technische universität
dortmund

Dissertation

Characterization of Classical Light Fields for Quantum Applications via Optical Homodyne Tomography

submitted in partial fulfillment of the
requirements for the degree of

Dr. rer. nat.

to the Institute of Physics of the
TU Dortmund University, Germany

by

Yannik Brune

Dortmund, April 2026

Submission: Dortmund, 29.04.2026

Disputation: Dortmund, 23.07.2026

Examination board:

Prof. Dr.	Marc Aßmann
Prof. Dr.	Christof Weitenberg
Prof. Dr.	Kevin Kröninger
Jun.-Prof. Dr.	Benedikt Fauseweh

Abstract

The goal of this work is to examine the coherence of classical light fields in order to assess their usefulness for quantum-informational tasks and to draw conclusions about the properties of the light source. To this end, we use and extend several optical homodyne tomography techniques employing four-port, eight-port, and sixteen-port detection schemes. To understand the role of coherence of a light field in solving a quantum informational task such as coherent qubit control, we begin by analyzing the qubit excitation process from a resource-theoretical perspective. By simulating the light-matter interactions, we demonstrate how the quantum coherence of the driving light field emerges as a key ingredient for coherent qubit control. At the same time, we show how the presence of thermal noise or dephasing significantly degrades the achievable quantum coherence of the light field. After studying the coherence properties of conventional lasers, we turn to non-conventional coherent light sources and investigate the emission of a non-resonantly excited exciton-polariton condensate. By employing long-lived polaritons and minimizing interactions with the reservoir, we optimize the condensation process and achieve a pronounced buildup of quantum superpositions in the condensate immediately above the condensation threshold. Finally, we shift our focus entirely to the matter system itself and use the coherence of the emitted light field to investigate its dynamics. For this purpose, we introduce a sixteen-port detection scheme that enables non-stationary and conditional analyses tailored to the requirements of semiconductor spectroscopy. Benchmarking the setup with a thermal light field, then demonstrate how we can resolve the stochastic fluctuations of the thermal state on the femtosecond level. Overall, our results establish connections between quantum optics, quantum information science, and semiconductor physics, providing insights relevant for quantum technologies and future hybrid quantum devices.

Zusammenfassung

Das Ziel dieser Arbeit ist es, die Kohärenzeigenschaften klassischer Lichtfelder zu untersuchen, um ihre Eignung für quanteninformationstechnische Aufgaben zu bewerten und Rückschlüsse auf die Eigenschaften der Lichtquelle zu ziehen. Zu diesem Zweck nutzen und erweitern wir verschiedene Techniken der optischen homodynen Tomographie unter Einsatz von Vierport-, Achtport- und Sechzehnportdetektor Setups. Um zunächst die Rolle der Kohärenz eines Lichtfeldes bei der Lösung eines quantuminformationstechnischen Problems wie der Manipulation von Qubits zu verstehen, beginnen wir die Analysen, indem wir den Qubitanregungsprozess aus einer quantenresourcentheoretischen Perspektive betrachten. Hierzu simulieren wir die Licht-Materie-Wechselwirkungen und zeigen, dass die Quantenkohärenz des treibenden Lichtfeldes die Schlüsselkomponente für die Preparation kohärenter Superpositionszustände ist. Gleichzeitig zeigen wir, wie thermische Fluktuationen oder Dephasierung die Quantenkohärenz des Lichtfeldes signifikant reduzieren. Nachdem wir die Kohärenzeigenschaften zunächst an konventionellen Lasern studiert haben, wechseln wir nun zu unkonventionellen kohärenten Lichtquellen und untersuchen die Emission eines nichtresonant angeregten Exziton-Polariton-Kondensates. Indem wir langlebige Polaritonen verwenden und zusätzlich die Wechselwirkungen mit dem inkohärenten Reservoir minimieren, erreichen wir die Ausbildung kohärenter Quantensuperpositionen innerhalb des Kondensats direkt oberhalb der Kondensationsschwelle. Zuletzt fokussieren wir uns vollständig auf die Lichtquelle und untersuchen die Kohärenzeigenschaften des emittierten Lichtfeldes, um dessen Dynamiken zu bestimmen. Zu diesem Zweck führen wir einen Sechzehnportdetektor ein, welcher es uns erlaubt, nichtstationäre und konditionale Analysen durchzuführen, angepasst an die Anforderungen der Halbleiterspektroskopie. Anhand des Benchmarks mit einem thermischen Lichtfeldes demonstrieren wir, dass wir die stochastischen Prozesse innerhalb des Lichtfeldes mit Femtosekundengenauigkeit auflösen können. Zusammenfassend verbinden unsere Ergebnisse Quantenoptik, Quanteninformationswissenschaften und Halbleiterphysik und geben Einblicke, die relevant für Quantentechnologien und zukünftige hybride Quantengeräte sind.

Contents

1 Introduction

In recent years, advances in quantum optics and quantum information science have led to remarkable progress in fields such as optical quantum computing, quantum communication, and quantum metrology. Within the framework of quantum information theory, the resourcefulness of a light field for performing a specific task can be quantified by an appropriately tailored quantum resource theory[1]. In most established approaches, non-classical light fields are regarded as resourceful, whereas classical light fields are considered not resourceful or free. In practice, however, this separation is not always consistent. A wide range of applications, including qubit manipulation[2, 3, 4] and quantum random number generation[5, 6], can also be implemented using classical states. Since classical light fields can be typically more easily, reliably, and cost-effectively generated, a tension arises between theoretical frameworks and experimental practice.

To address part of this discrepancy, we begin this work by introducing a quantum resource theory for lasers in which coherent states are considered resourceful while thermal states are regarded as free. This theory is tailored to the requirements of coherent qubit control and is based on the framework of quantum coherence. Building on this foundation, we investigate which physical mechanisms degrade quantum coherence and how quantum coherence influences the performance of coherent qubit control. After establishing the resource theory used to describe laser emission, we adapt it to evaluate the emission of other non-conventional sources of partially coherent light. An ideal test platform for this approach is a system of exciton-polaritons, hereafter referred to simply as polaritons[7]. These hybrid light-matter quasiparticles can undergo a phase transition into a Bose-Einstein-condensate-like state, accompanied by the formation of quantum superpositions. The quality of the condensate depends on the relative fractions of condensed and uncondensed polaritons as well as on interactions with incoherent particles in the surrounding reservoir. In this work, we therefore aim to improve the coherence properties of the condensate by optimizing polariton thermalization while simultaneously minimizing interactions with the incoherent reservoir. The coherence properties of the condensate are analyzed through its optical emission, since polaritons decay by emitting photons that inherit their quantum properties. In this way, the coherence characteristics of the condensate are transferred to the emitted light field. This property makes polariton condensates not only promising low-threshold sources of

coherent light fields, but also valuable test beds for the investigations of non-trivial dynamics. To characterize the coherence properties of the emission - as well as those of the other light fields studied throughout this work - we employ optical homodyne tomography. By sampling the quadrature operator of the light field using homodyne detection, this method provides us access to information about the underlying quantum state of the optical field. Finally, we extend the coherence analysis to applications in semiconductor spectroscopy. To this end, we expand the previously used homodyne detection scheme and develop a detection architecture that enables non-stationary and conditional analyses with temporal resolutions down to 100 fs and a wide range of a posteriori applicable conditions. The capabilities of this advanced detection scheme are then benchmarked on a thermal light field, demonstrating how the incoherent field emerges from the incoherent superposition of coherent pulses emitted by a large ensemble of emitters

The thesis is structured as follows: chapters 2 and 3 establish the theoretical fundamentals of quantum optics and exciton-polaritons. Building upon these concepts, chapter 4 introduces the principles of homodyne detection and optical tomography. Subsequently, chapter 5 describes the experimental setup employed to generate and investigate polariton condensates. The experimental results are presented in chapters 6-8. In chapter 6, we develop a new quantum resource theory for realistic laser light fields, based on the framework of quantum coherence. Subsequently, quantum coherence is used to study the condensation process of a polariton condensate in chapter 7. Extending the methodological scope of optical homodyne tomography to the needs of semiconductor spectroscopy, chapter 8 modifies the experimental setup to enable non-stationary and conditional analyses. The work is concluded with a brief summary and an outlook in chapter 9. Since the result chapters are largely self-contained, chapters 6-8 each include dedicated introductions and conclusions.

2 Theoretical Foundations - Quantum Optics

The goal of this chapter is to set the theoretical foundations required to describe light fields in quantum optics and to evaluate their coherence properties. The chapter is divided into two major sections. The first section provides a concise introduction to the quantum-optical description of light fields. We introduce different types of light fields and consider their representations in terms of discrete density matrices and continuous phase-space distributions. In the second section, we build upon these definitions and discuss a range of coherence quantifiers. We will use these quantifiers not only to distinguish between different types of light fields but also to assess their usefulness for concrete quantum-optical tasks.

2.1 Light Field Description in Quantum Optics

2.1.1 A Light Field Is an Electromagnetic Wave

We begin our considerations on light fields with the classical picture of light as an electromagnetic wave consisting of an electric field $\vec{E}$ and a magnetic field $\vec{B}$. The dynamics of both fields are governed by the Maxwell equations. In the absence of electric charges or currents, these equations yield the wave equation for the electric field

$$\nabla^2 \vec{E} = \frac{1}{c^2} \frac{\partial^2 \vec{E}}{\partial t^2} \,, \tag{2.1}$$

where $c = (\mu_0 \epsilon_0)^{-\frac{1}{2}} \approx 299\,792\,458\,\mathrm{m\,s^{-1}}$ denotes the speed of light, determined by the vacuum permittivity ϵ_0 and permeability μ_0 [8]. The simplest non-trivial solution of the wave equation is the monochromatic, linearly polarized plane wave, corresponding to a single optical mode. Assuming propagation along the z-axis and polarization along the x-axis, the electric field is given by

$$\vec{E}(z,t) = E_0 \mathrm{e}^{i(k_z z - \omega t + \varphi_0)} \vec{e}_x \,, \tag{2.2}$$

and depends on the electric-field amplitude E_0, the angular frequency ω, the wave vector component k_z, and a constant but otherwise arbitrary phase offset φ_0. The magnetic field, polarized along the y-axis, follows analogously as

$$\vec{B}(z,t) = B_0 \mathrm{e}^{i(k_z z - \omega t + \varphi_0 + \frac{\pi}{2})} \vec{e}_y \,. \tag{2.3}$$

In general, a real light field is a superposition of several modes $\vec{E}_\mathrm{i}$, such that the total electric field is

$$\vec{E}(z,t) = \sum_\mathrm{i} \vec{E}_\mathrm{i}(z,t) = \sum_\mathrm{i} \vec{E}_{0,\mathrm{i}} \mathrm{e}^{i(k_{z,\mathrm{i}} z - \omega_\mathrm{i} t + \varphi_{0,\mathrm{i}})} \tag{2.4}$$

2.1.2 A Light Field Is a Quantum Object

A fundamentally different description emerges when the light field is treated quantum mechanically. In this picture, a light field is not regarded as a superposition of electromagnetic waves but rather as a stream of photons - bosonic particles with the energy $\hbar\omega$. A photon stream is mathematically described by a quantum state, an abstract tensor, defined on an infinite-dimensional Hilbert space $\mathcal{H}$. The representation of a quantum state depends on the set of basis vectors $\{|\Psi_\mathrm{i}\rangle\}$ spanning $\mathcal{H}$. Depending on its structure, a quantum state may be either pure or mixed. Additionally, one must distinguish between single-mode and multi-mode quantum states. In this context, we define a single-mode state as a state associated with a single light-field mode that is characterized by a specific spatial-temporal distribution, energy, polarization, and orbital angular momentum. Importantly, we do not necessarily consider mixed states as multi-mode states. We begin with the description of single-mode quantum states:

1. **Pure States**
   A state is referred to as pure if it is represented by a single state vector. The representation in a given basis $\{|\Psi_\mathrm{i}\rangle\}$ is then a coherent superposition of basis states

   $$|\Psi\rangle = \sum_\mathrm{i} \langle\Psi_\mathrm{i}|\Psi\rangle |\Psi_\mathrm{i}\rangle \,, \tag{2.5}$$

   using the identity operator $\hat{I} = \sum_\mathrm{i} |\Psi_\mathrm{i}\rangle\langle\Psi_\mathrm{i}|$ and the scalar product of the Hilbert space $\langle\Psi_\mathrm{i}|\Psi\rangle$. In addition, we introduce the density operator of the pure state, denoted by $\hat{\rho}_\mathrm{P}$, which is defined by the dyadic product

   $$\hat{\rho}_\mathrm{P} = |\Psi\rangle\langle\Psi| \,. \tag{2.6}$$

2. **Mixed States**
   If a state cannot be described by a single state vector, it is referred to as mixed. This situation arises when the light field is described as a stochastic ensemble of several pure states due to incomplete knowledge of the system. In this case, the state must be represented by a mixed density operator of the form

$$\hat{\rho}_{\mathrm{M}} = \sum_{\mathrm{i}} W_{\mathrm{i}} \hat{\rho}_{\mathrm{P,i}} = \sum_{\mathrm{i}} W_{\mathrm{i}} |\Psi_{\mathrm{i}}\rangle\langle\Psi_{\mathrm{i}}| \,, \tag{2.7}$$

   where each pure state $|\Psi_{\mathrm{i}}\rangle$ occurs with probability W_{i}.

Throughout this work, we primarily employ the description with density operators. In the next step, we extend the description to two-mode quantum states, defined on a Hilbert space $\mathcal{H}^{\mathrm{AB}} = \mathcal{H}^{\mathrm{A}} \otimes \mathcal{H}^{\mathrm{B}}$. The characterization of such two-mode states depends on whether the modes are separable or entangled. If the modes are separable, the joint density operator of the light field can be factorized as

$$\hat{\rho}^{\mathrm{AB}} = \sum_{\mathrm{i}} p_{\mathrm{i}} \left(\hat{\rho}_{\mathrm{i}}^{\mathrm{A}} \otimes \hat{\rho}_{\mathrm{i}}^{\mathrm{B}} \right) . \tag{2.8}$$

If such a factorization is not possible, the modes are entangled. Finally, we consider the calculation of expectation values. The expectation value of an observable $\hat{O}$ for a given state $\hat{\rho}$ is determined by the trace operation

$$\langle \hat{O} \rangle = \mathrm{tr}(\hat{O}\hat{\rho}) \,. \tag{2.9}$$

For multipartite systems, subsystems can be traced out using the partial trace [9, p. 123-124]. As an example, the operation

$$\mathrm{tr}_{\mathrm{B}}(\hat{\rho}^{\mathrm{AB}}) = \sum_{\mathrm{i}} (\hat{I}^{\mathrm{A}} \otimes \langle \Psi_{\mathrm{i}}^{\mathrm{B}}|) \hat{\rho}^{\mathrm{AB}} (\hat{I}^{\mathrm{A}} \otimes |\Psi_{\mathrm{i}}^{\mathrm{B}}\rangle) = \hat{\rho}^{\mathrm{A}} \,, \tag{2.10}$$

traces out subsystem B out of a two-mode system, described by $\hat{\rho}^{\mathrm{AB}}$, and yields the reduced density operator of subsystem A.

2.1.3 The Photon Number Representation

Up to this point, we have treated quantum states as abstract mathematical objects represented in a fixed but otherwise arbitrary basis. Our next objective is to find a basis that is particularly well-suited for describing light fields. The first basis of interest is the orthogonal Fock basis $\{|n\rangle\}$, which consists of the eigenstates of the photon number operator $\hat{n} = \hat{a}^{\dagger}\hat{a}$, where $\hat{a}$ and $\hat{a}^{\dagger}$ denote the bosonic annihilation

and creation operators of a single mode. The Fock states can be constructed from the vacuum state $|0\rangle$ through repeated application of the bosonic creation operator

$$|n\rangle = \frac{(\hat{a}^\dagger)^n}{\sqrt{n!}}|0\rangle\,. \tag{2.11}$$

The representation of an arbitrary single-mode density operator in the Fock basis is given by

$$\hat{\rho} = \sum_{m,n} |m\rangle\langle m|\hat{\rho}|n\rangle\langle n| = \sum_{m,n} \rho_{m,n}|m\rangle\langle n|\,, \tag{2.12}$$

where the elements $\rho_{m,n} = \langle m|\hat{\rho}|n\rangle$ form the density matrix $\boldsymbol{\rho}$ of the quantum state in Fock representation, hereafter simply referred to as the density matrix. Its main diagonal elements $\rho_{n,n}$ correspond to the photon statistics $P(n) = \rho_{n,n}$ of the light field. In the special case of a Fock state, the density matrix contains a single non-zero element. For example, the state $|10\rangle$ yields a density matrix and photon statistics as shown in panels (a) and (d) of figure 2.1. The density matrix is singular with $\rho_{10,10} = 1$, and the photon statistics exhibit a single entry at $n = 10$. In the following section, we employ the density-matrix formalism to discuss additional light fields that are more readily accessible experimentally and play an important role throughout this work.

2.1.4 Classical States of Light

The Coherent State

The first important light field is the coherent light, emitted, for example, by an ideal laser. The motivation is to identify a light field whose quantum-mechanical description resembles the properties of a classical electromagnetic wave. Consequently, such a state $|\alpha\rangle$ must be an eigenstate of the annihilation operator, since the properties of a classical wave would remain unchanged under measurement [10, p. 523-524]. Assuming that such a state exists, we start with the general expansion

$$|\alpha\rangle = \sum_{n=0}^{\infty} c_n|n\rangle, c_n \in \mathbb{C}\,, \tag{2.13}$$

and insert it into the eigenvalue equation

$$\hat{a}|\alpha\rangle = \alpha|\alpha\rangle\,. \tag{2.14}$$

This yields the recurrence relation between consecutive coefficients

$$\sqrt{n}c_n = \alpha c_{n-1}\,, \tag{2.15}$$

which can be traced back to

$$c_n = \frac{\alpha^n}{\sqrt{n!}}c_0\,. \tag{2.16}$$

After normalizing the state, one obtains the Fock representation

$$|\alpha\rangle = \mathrm{e}^{-\frac{|\alpha|^2}{2}} \sum_{n=0}^{\infty} \frac{\alpha^n}{\sqrt{n!}}|n\rangle\,. \tag{2.17}$$

From this representation, the photon statistics of the coherent state can be derived as

$$P_n = |\langle\alpha|n\rangle|^2 = \mathrm{e}^{-|\alpha|^2}\frac{|\alpha|^{2n}}{n!}\,. \tag{2.18}$$

Thus, the photon statistics of a coherent state follow a Poisson distribution with $\langle\hat{n}\rangle = |\alpha|^2$. The density matrix and photon statistics of a coherent state with mean photon number $|\alpha|^2 = 10$ are illustrated in figure 2.1 (b) and (e). Compared to a Fock state, the photon statistics are broadened with $\mathrm{Var}(n) = |\alpha|^2$, and the density matrix exhibits significant off-diagonal elements. Coherent states form an overcomplete basis [11, p. 301-302], whereby the scalar product between two coherent states $|\alpha\rangle$ and $|\beta\rangle$ is given by

$$\langle\alpha|\beta\rangle = \mathrm{e}^{-\frac{1}{2}(|\alpha|^2+|\beta|^2)+\alpha^*\beta}\,. \tag{2.19}$$

The Thermal State

A second important type of light field is the thermal light, emitted, for example, by light bulbs, LEDs, or the sun. It is described by a thermal state with density operator $\hat{\rho}_{\mathrm{th}}$. In contrast to coherent light, thermal light cannot be interpreted as radiation from a single emitter. Instead, it must be considered as the incoherent superposition of many wave packets emitted by a large number of uncorrelated emitters. Consequently, the density matrix of a thermal state is diagonal, since all coherent superpositions vanish under ensemble averaging. The Fock representation of a thermal state with mean photon number $\langle\hat{n}\rangle = n_{\mathrm{th}}$ is given by [11, p. 52]

$$\hat{\rho}_{\mathrm{th}}(n_{\mathrm{th}}) = \frac{1}{n_{\mathrm{th}}+1}\sum_{n=0}^{\infty}\left(\frac{n_{\mathrm{th}}}{n_{\mathrm{th}}+1}\right)^n |n\rangle\langle n|\,. \tag{2.20}$$

The corresponding photon statistics follow the Bose-Einstein distribution. The density matrix and photon statistics of a thermal state are illustrated for the example $n_{\mathrm{th}} = 10$ in figure 2.1, panels (c) and (f). In this case, the matrix is diagonal, and the vacuum state has the most probable outcome while the outcome probability of higher Fock states decreases gradually with increasing Fock-state number. The Bose-Einstein distribution leads to a variance of $\mathrm{Var}(\hat{n}) = \langle\hat{n}\rangle^2 + \langle\hat{n}\rangle$.

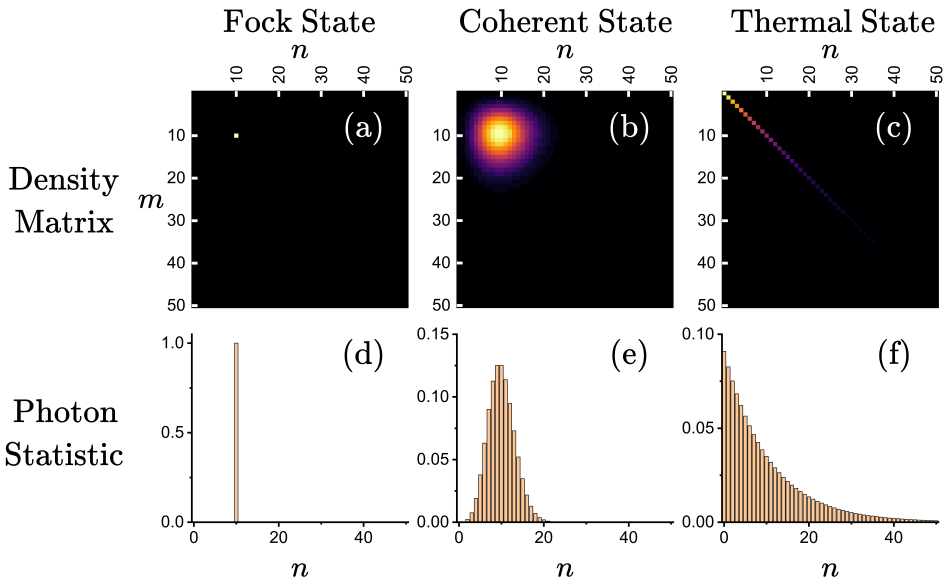

Figure 2.1: Density matrices and photon statistics for a Fock state ((a), (d)), a coherent state ((b), (e)) and a thermal state ((c), (f)) of average photon number $\langle\hat{n}\rangle = 10$.

2.1.5 Light-Field Description in Phase Space

So far, we have described light fields exclusively in terms of density matrices using the discrete Fock-basis representation. An alternative approach, better suited to describe the field-like properties of light, is a description in phase space using continuous variables. The following motivation is based on [12, p. 13]. We begin with the classical picture of the electric field as a plane wave, as introduced in equation (2.2). Although the electric field is generally dependent on several parameters, many of these parameters remain fixed in a typical experiment. As an example, we consider the detection of a light field propagating along the z-axis on a detector. In a typical experimental configuration, the detector position z_0 is fixed. Furthermore, one is usually not interested in the entire signal but rather in a specific mode characterized

by a fixed frequency ω_0, a fixed wave-vector component $k_{z,0}$, and a fixed polarization vector $\vec{E}_0$. Under these conditions, the spatial term $k_z z$ becomes constant and can be absorbed into the phase $\varphi = k_{z,0} z_0 + \varphi_0$. Considering the electric field within the plane of polarization, the field reduces to a harmonic oscillation in time,

$$E(z_0, t) = E_0 \mathrm{e}^{i\varphi} \mathrm{e}^{-i\omega_0 t} = \mathcal{E} \mathrm{e}^{-i\omega_0 t}\,, \tag{2.21}$$

where the spatial properties are embedded into the complex amplitude $\mathcal{E}$. The real and imaginary parts of $\mathcal{E}$ can be mapped onto the position and momentum coordinates q and p, such that the complex amplitude corresponds to a point in phase space, determined by the field amplitude E_0 and the phase φ:

$$\begin{aligned} q &= \mathrm{Re}[\mathcal{E}] = E_0 \cos(\varphi) \\ p &= \mathrm{Im}[\mathcal{E}] = E_0 \sin(\varphi)\,. \end{aligned} \tag{2.22}$$

In the next step, the light field is quantized by promoting the variables q and p to the position and momentum operators $\hat{q}$ and $\hat{p}$. These operators are related to the bosonic annihilation and creation operators, as the quantized light field can be mapped onto the harmonic oscillator problem; see, for example, [11, p. 256-272]. Using the commutator relation convention $[\hat{q}, \hat{p}] = i$ and adopting the convention $\hbar = 1$, one obtains

$$\begin{aligned} \hat{q} &= \frac{1}{\sqrt{2}}(\hat{a} + \hat{a}^\dagger) \\ \hat{p} &= \frac{1}{\sqrt{2}i}(\hat{a} - \hat{a}^\dagger)\,. \end{aligned} \tag{2.23}$$

An equivalent way to span the phase space is to use the complex eigenvalues of the annihilation operator. Since $\hat{a}$ is related to $\hat{q}$ and $\hat{p}$ via $\hat{a} = \frac{1}{\sqrt{2}}(\hat{q} + i\hat{p})$, the corresponding relation between the phase space variables is given by

$$\alpha = \frac{1}{\sqrt{2}}(q + ip)\,. \tag{2.24}$$

This equivalence allows one to switch between phase-space variables depending on the application. In practice, the (q, p)-space representation is commonly used in experiments, whereas the α-space representation is often more convenient for definitions and theoretical calculations. The position and momentum operators can further be generalized to the quadrature operator $\hat{\epsilon}_\varphi$ [11, p. 293], defined as

$$\hat{\epsilon}_\varphi = \cos(\varphi)\hat{q} + \sin(\varphi)\hat{p} = \frac{1}{\sqrt{2}}(\hat{a}\mathrm{e}^{-i\varphi} + \hat{a}^\dagger \mathrm{e}^{i\varphi})\,, \tag{2.25}$$

where the relative contributions of $\hat{q}$ and $\hat{p}$ are determined by the phase φ. The generalized operator satisfies the same commutator relation as $[\hat{q}, \hat{p}]$ as one finds

$$\begin{aligned}[\hat{\epsilon}_\varphi, \hat{\epsilon}_{\varphi+\frac{\pi}{2}}] &= [(\cos(\varphi)\hat{q} + \sin(\varphi)\hat{p})\,(-\sin(\varphi)\hat{q} + \cos(\varphi)\hat{p})] - \\ &\quad [(-\sin(\varphi)\hat{q} + \cos(\varphi)\hat{p})\,(\cos(\varphi)\hat{q} + \sin(\varphi)\hat{p})] \\ &= \left(\sin(\varphi)^2 + \cos(\varphi)^2\right)\left(\hat{q}\hat{p} - \hat{p}\hat{q}\right) \\ &= [\hat{q}, \hat{p}]\ .\end{aligned} \tag{2.26}$$

2.1.6 Light-Field Description via Phase-Space Quasi-Probability Distributions

The phase space spanned by α can be used to define a family of phase-space distributions, quasi-probability distributions, which contain the complete information about the quantum state. We begin with the representation of an arbitrary state described by the density operator $\hat{\rho}$ in the basis of coherent states

$$\hat{\rho} = \frac{1}{\pi^2}\int \mathrm{d}^2\alpha \int \mathrm{d}^2\beta\, |\alpha\rangle\langle\alpha|\hat{\rho}|\beta\rangle\langle\beta| = \int \mathrm{d}^2\alpha \int \mathrm{d}^2\beta\, F(\alpha,\beta)|\alpha\rangle\langle\beta|\,, \tag{2.27}$$

by inserting the identity operator in the coherent basis $\hat{I} = \frac{1}{\pi}\int \mathrm{d}^2\alpha\, |\alpha\rangle\langle\alpha|$. The continuous function $F(\alpha,\beta) = \frac{1}{\pi^2}\langle\alpha|\hat{\rho}|\beta\rangle$ then defines a quasi-probability distribution.

The Glauber-Sudarshan P Distribution

In contrast to the density matrix, $F(\alpha,\beta)$ is not uniquely defined because the set of coherent states forms an overcomplete basis. Consequently, every quantum state has a specific distribution $P(\alpha)$, which diagonalizes the representation

$$\hat{\rho} = \int \mathrm{d}^2\alpha\, P(\alpha)|\alpha\rangle\langle\alpha|\,. \tag{2.28}$$

This distribution is the Glauber-Sudarshan P distribution, hereafter simply referred to as the P distribution. It was independently introduced by R.J. Glauber and E.C.G. Sudarshan [13][14]. While the properties of the P distribution are powerful, different drawbacks often complicate its efficient use. From a theoretical perspective, its implicit definition often hardens the calculation of analytical expressions. From an experimental perspective, the occurrence of higher-order singularities hinders numerical treatment. For this reason, one usually prefers other, smoother distributions that are related to the P distribution via convolution.

Although there is, in principle, an infinite number of information-wise equivalent phase-space distributions, in practice, mainly two additional distributions are particularly relevant due to their properties.

The Husimi-Kano Q Distribution

The first of these distributions is the Husimi-Kano Q distribution, hereafter referred to as Husimi-Q or simply Q distribution. It was originally introduced by K. Husimi and later rediscovered by Y. Kano [15][16]. The Q distribution $Q(\alpha)$ is defined as

$$Q(\alpha) = \frac{1}{\pi}\langle\alpha|\hat{\rho}|\alpha\rangle\,, \tag{2.29}$$

and corresponds to the probability of finding the quantum state $\hat{\rho}$ in the coherent state $|\alpha\rangle$. Using equations (2.28) and (2.19), one obtains

$$Q(\alpha) = \frac{1}{\pi}\langle\alpha|\hat{\rho}|\alpha\rangle = \frac{1}{\pi}\int \mathrm{d}^2\beta\, P(\beta)|\langle\alpha|\beta\rangle|^2 = \frac{1}{\pi}\int \mathrm{d}^2\beta\, P(\beta)\mathrm{e}^{-|\alpha-\beta|^2}\,, \tag{2.30}$$

which shows that the Q distribution is related to the P distribution through convolution with a Gaussian kernel of width $\frac{1}{\sqrt{2}}$. This convolution produces a smooth phase-space distribution that remains positive over the entire complex plane.

The Wigner W Distribution

The final important phase-space distribution is the Wigner W distribution. Historically, it was first introduced by E. Wigner as the Weyl transform of the density operator

$$W(q,p) = \frac{1}{2\pi}\int_{-\infty}^{\infty} \mathrm{d}\zeta\, \mathrm{e}^{-ip\zeta}\left\langle q+\frac{1}{2}\zeta\right|\hat{\rho}\left|q-\frac{1}{2}\zeta\right\rangle\,, \tag{2.31}$$

in order to describe a quantum-mechanical system in a manner analogous to a classical statistical mechanical system characterized by a probability distribution in phase space [17]. The Weyl transformation consists of two steps. First, one evaluates the probability amplitude for the system to perform a quantum step from the position eigenstate $\left|q-\frac{\zeta}{2}\right\rangle$ to the position eigenstate $\left|q+\frac{\zeta}{2}\right\rangle$. Second, a Fourier transform is applied to convert the stepsize ζ into the associated momentum p.

Similar to the Q distribution, the W distribution is related to the P distribution through convolution with a Gaussian kernel [18, p. 54]. One obtains

$$W(\alpha) = \frac{2}{\pi} \int \mathrm{d}^2\beta \, P(\beta) \mathrm{e}^{-2|\alpha-\beta|^2} \,, \tag{2.32}$$

which corresponds to a kernel width of $\frac{1}{2}$. Consequently, the W distribution is less strongly smoothed than the Q distribution. Due to this reduced smoothing, the W distribution can become locally negative. Such negativities are commonly interpreted as an indicator of the non-classicality of a light field. The converse, however, is not necessarily true, since certain non-classical states - such as squeezed states - possess a positive W distribution.

The P, W, and Q distributions of an exemplarily coherent state $|\alpha_0\rangle = |2 + i\rangle$ are shown in figure 2.2.

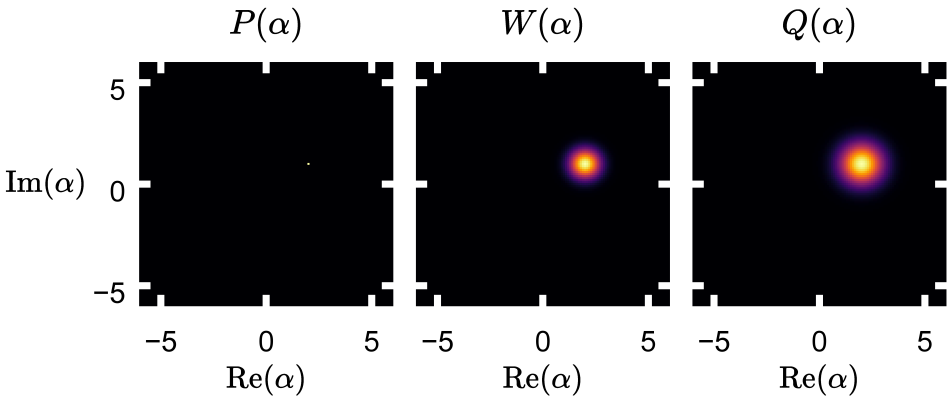

Figure 2.2: Phase-space distributions $P(\alpha)$, $W(\alpha)$, and $Q(\alpha)$ of the coherent state $|\alpha\rangle = |2 + i\rangle$

2.1.7 The Displacement Operator

Based on the phase-space representation of quantum states, one can introduce the displacement operator $\hat{D}(\alpha)$, which displaces a quantum state in phase space by the complex value α [10, p. 525-526]. The operator is defined as

$$\hat{D}(\alpha) = \exp\left(\alpha\hat{a}^\dagger - \alpha^*\hat{a}\right) . \tag{2.33}$$

A special case arises when the displacement operator is applied to the vacuum state. In this situation, the resulting state is a coherent state,

$$|\alpha\rangle = \hat{D}(\alpha)|0\rangle . \tag{2.34}$$

Thus, a coherent state corresponds to a vacuum state, displaced in phase space.

2.1.8 The Displaced Thermal State

The displacement operator can also be used to generalize coherent and thermal states to a displaced thermal state $\hat{\rho}_{\mathrm{DT}}(|\alpha|^2, n_{\mathrm{th}})$ [19, p.131], which contains both coherent and thermal contributions. This state is obtained by applying the displacement operator to a thermal state

$$\hat{\rho}_{\mathrm{DT}}(|\alpha|^2, n_{\mathrm{th}}) = \hat{D}(\alpha)\hat{\rho}_{\mathrm{th}}(n_{\mathrm{th}})\hat{D}^\dagger(\alpha) . \tag{2.35}$$

The average photon number of the displaced thermal state is given by the sum of the coherent and thermal photon numbers $\langle\hat{n}\rangle = n_{\mathrm{DT}} = |\alpha^2| + n_{\mathrm{th}}$, while the variance is given by $\mathrm{Var}(\hat{n}) = |\alpha|^2 + n_{\mathrm{th}}^2 + (2|\alpha|^2 + 1)n_{\mathrm{th}}$ [20]. Displaced thermal states form a class of Gaussian states that are characterized by a positive centrosymmetric Gaussian distribution in phase-space. In this situation, a change from the P distribution to the W or the Q distribution affects only the distribution's width, not its general shape. The coherent state and the thermal state arise as special cases of the displaced thermal state model as a coherent state corresponds to $\hat{\rho}_{\mathrm{Coh}}(|\alpha|^2) = \hat{\rho}_{\mathrm{DT}}(|\alpha|^2, 0)$, while a thermal state is obtained by $\hat{\rho}_{\mathrm{th}}(n_{\mathrm{th}}) = \hat{\rho}_{\mathrm{DT}}(0, n_{\mathrm{th}})$.

2.1.9 Calculation of Expectation Values from a Phase-Space Distribution

Finally, we consider the calculation of expectation values from a phase-space distribution. The underlying idea stems from the desire to determine the expectation value of an observable, analogous to the procedure used in classical statistical mechanics. In classical statistical mechanics, a single-particle system is described by

a probability distribution $P^{(\mathrm{cl})}(q,p)$ in phase space, spanned by the generalized position and momentum variables q and p. The expectation value of a classical observable $O^{(\mathrm{cl})}(q,p)$ is then given by

$$\langle O(q,p)\rangle = \int_{-\infty}^{\infty} \mathrm{d}q \int_{-\infty}^{\infty} \mathrm{d}p\, O^{(\mathrm{cl})}(q,p) P^{(\mathrm{cl})}(q,p)\,, \tag{2.36}$$

which corresponds to the weighted average of the observable, with $P^{\mathrm{cl}}(q,p)$ acting as the weight function. In classical physics, this relation is unambiguous. In quantum mechanics, however, it is not, as a potential classical analog to $\hat{O}$ would depend on the operator ordering of $\hat{O}$. This ambiguity can be resolved using the optical equivalence theorem [14][21][22][23]. Let $\hat{O}(\hat{a},\hat{a}^\dagger)$ be an operator expressed in terms of the bosonic annihilation and creation operators with a finite normal-ordered finite expansion

$$\hat{O}(\hat{a},\hat{a}^\dagger) = \sum_{\mathrm{i,j}} c_{\mathrm{i,j}} \hat{a}^{\dagger \mathrm{i}} \hat{a}^{\mathrm{j}}\,. \tag{2.37}$$

One can then define the function $O^{(n)}(\alpha)$ associated with this operator,

$$O^{(n)}(\alpha) = \sum_{\mathrm{i,j}} c_{\mathrm{i,j}} \alpha^{*\mathrm{i}} \alpha^{\mathrm{j}}\,, \tag{2.38}$$

which allows calculating the expectation value of $\hat{O}$ via

$$\langle \hat{O}\rangle = \int \mathrm{d}^2\alpha\, O^{(n)}(\alpha) P(\alpha)\,. \tag{2.39}$$

This formalism can be generalized to normal, symmetric, and antinormal operator ordering. In this case, one obtains

$$\langle \hat{O}\rangle = \int \mathrm{d}^2\alpha\, O^{(\Omega)}(\alpha) F^{(\bar{\Omega})}(\alpha)\,, \tag{2.40}$$

where $O^{(\Omega)}(\alpha)$ denotes the function corresponding to the Ω-ordered observable and $F^{(\bar{\Omega})}(\alpha)$ represents the phase-space distribution associated with the oppositely-ordered density operator. Within this framework, the P distribution is associated with the antinormally-ordered density operator $\hat{\rho}^{(a)}$, the Wigner distribution with the symmetrically-ordered density operator $\hat{\rho}^{(s)}$, and the Husimi-Q distribution with the normally-ordered density operator $\hat{\rho}^{(n)}$.

2.2 Quantifying the Coherence of a Light Field

In the previous section, we introduced the general quantum-optical description of light fields. However, in order to classify an unknown light field in an experiment or to assess its suitability for a quantum-optical task, it is necessary to characterize the light field through measurable physical properties. One of the most important properties is the coherence of the light field. As will become apparent, coherence cannot be quantified unambiguously by a single quantifier; rather, the appropriate quantifier depends on the specific application. For this reason, we briefly introduce several coherence measures in the following.

2.2.1 Correlation Functions

The most widely used family of coherence quantifiers consists of the correlation functions $g^{(\mathrm{n})}(\vec{r}, \vec{r}', t, t')$. A correlation function measures the correlations between the light field at two points in space and time $(\vec{r}, t)$ and $(\vec{r}', t')$, normalized to the case of completely uncorrelated fields. The type of coherence probed depends on the order of the correlation function. Throughout this work, we will focus on temporal correlations of the form $g^{(\mathrm{n})}(t, t' = t + \tau)$, where τ denotes the time delay between the two points. Further, we distinguish between general and stationary light fields. In the general case, the correlations depend on both t and τ, whereas in the stationary case the coherence properties become independent of the absolute time, and the correlation functions reduce to the form $g^{(\mathrm{n})}(\tau)$.

The First-Order Correlation Function

The lowest-order correlation function is the first-order correlation function $g^{(1)}(t, \tau)$ [24, p. 16-19], defined in terms of the complex electric field $E(t)$ as

$$g^{(1)}(t, \tau) = \frac{\langle E^*(t) E(t + \tau) \rangle)}{\sqrt{\langle E^*(t) E(t) \rangle \langle E^*(t + \tau) E(t + \tau) \rangle}} \,. \tag{2.41}$$

The first-order correlation function quantifies how well the phase of the field at time $t + \tau$ can be predicted from the phase at time t. Its magnitude takes values in the interval $[-1, 1]$, where $|g^{(1)}(t, \tau)| = 1$ indicates perfect coherence and 0 corresponds to a completely incoherent phase relation. By definition, one always has $|g^{(1)}(t, 0)| = 1$, independent of the specific light field. For a single-mode light field, the phase coherence persists for increasing τ. In contrast, for multi-mode light fields, the coherence decreases with increasing time delay. This behavior arises from the finite spectral width of the light field, which leads to a gradual broadening of the

phase distribution over time. As a consequence, $|g^{(1)}(t,\tau)|$ approaches zero when the time delay becomes large compared to the first-order coherence time. For stationary light fields, power spectrum $S(\omega)$ and autocorrelation function $\langle E^*(t)E(t+\tau)\rangle$ are related through the Wiener-Khinchin theorem [10, p. 56-59]

$$\langle E^*(t)E(t+\tau)\rangle = \int_{-\infty}^{\infty} \mathrm{d}\omega\, S(\omega)\mathrm{e}^{-i\omega\tau}\,. \tag{2.42}$$

Importantly, this relation implies that $g^{(1)}$ characterizes the properties of the light field itself but does not necessarily allow direct conclusions about the emitting light source. For instance, the coherence time of a light field can be artificially increased by narrowing its spectral bandwidth with a spectral filter. In order to distinguish between different types of light sources, it is therefore necessary to consider higher-order correlation functions.

The Second-Order Correlation Function

The lowest-order correlation function that allows one to distinguish between different light sources is the second-order correlation function $g^{(2)}(t,\tau)$. It corresponds to the conditional probability of detecting a photon at time $t+\tau$, given that a photon has been detected at time t, normalized to the case of uncorrelated detection events. This measurement scheme is associated with the Hanbury Brown-Twiss experiment [25]. For a single-mode light field, $g^{(2)}(t,\tau)$ is defined as [24, p. 161]

$$g^{(2)}\,(t,\tau) = \frac{\langle \hat{a}^\dagger(t)\hat{a}^\dagger(t+\tau)\hat{a}(t+\tau)\hat{a}(t)\rangle}{\langle \hat{a}^\dagger(t)\hat{a}(t)\rangle\langle \hat{a}^\dagger(t+\tau)\hat{a}(t+\tau)\rangle}\,. \tag{2.43}$$

Similar to $g^{(1)}$, $g^{(2)}$ typically exhibits an extremum at $\tau = 0$, corresponding to the detection of photon pairs, and approaches unity for increasing τ as the correlations between the detection events vanish. In the remainder of this section, we focus on the detection of photon pairs. Using the bosonic commutation relation $g^{(2)}(t,0)$ simplifies to

$$g^{(2)}\,(t,0) = \frac{\langle \hat{n}(t)\,(\hat{n}(t)-1)\rangle}{\langle \hat{n}(t)\rangle^2}\,, \tag{2.44}$$

which depends solely on the photon number operator. In the next step, we express the expectation values in terms of ensemble averages. Each sampled photon number n_i can be written as a deviation Δn_i from the ensemble average such that $n_\mathrm{i} = \langle\hat{n}\rangle + \Delta n_\mathrm{i}$. Using this substitution, all terms linear in Δn vanish in the ensemble average, yielding the final expression

$$g^{(2)}(t,0) = 1 - \frac{1}{\langle \hat{n}(t)\rangle} + \frac{\mathrm{Var}(\hat{n}(t))}{\langle \hat{n}(t)\rangle^2}\,, \tag{2.45}$$

which depends only on the average photon number $\langle \hat{n}(t) \rangle$ and the variance of the photon statistics $\mathrm{Var}(\hat{n}(t)) = \langle (\Delta n(t))^2 \rangle$. Since this expression is central to the subsequent chapters, we briefly discuss the physical interpretation of the three contributing terms. The first term corresponds to the standard value expected for uncorrelated detection events. The second term decreases $g^{(2)}(0)$. It arises from the removal of a photon during the first photon-detection event, which reduces the probability of detecting a second photon immediately afterward. Light fields dominated by this term are referred to as antibunched, since their photon streams consist primarily of temporally separated single photons. The third term increases $g^{(2)}(0)$ and arises from two considerations: First, the probability of detecting the first photon increases with the instantaneous photon number. Considering a light field of fluctuating photon number, this implies that time intervals with higher photon number contribute more strongly to $g^{(2)}(0)$ than time intervals with lower photon number. Second, a high instantaneous photon number also increases the probability of detecting a second photon, since the photon number after the first detection is typically still above the average value. As a result, photon-number fluctuations increase $g^{(2)}(0)$. Light fields dominated by the third term are referred to as bunched, as the photons tend to appear in temporal clusters.

The three terms allow the evaluation of $g^{(2)}(0)$ for the light fields introduced in the previous section. For a Fock state, the variance of the photon statistics is zero, resulting in $g^{(2)}(0) = 1 - \frac{1}{\langle \hat{n} \rangle}$. This value becomes zero for an ideal single-photon source and converges to unity with increasing $\langle \hat{n} \rangle$. The general limitation $g^{(2)}(0) < 1$ underscores the non-classical character of Fock states. For a coherent state, the variance is given by $\mathrm{Var}(\hat{n}) = \langle \hat{n} \rangle$. This leads to $g^{(2)}(0) = 1$, since the second and third terms cancel each other. The result reflects the interpretation of coherent states as the quantum-mechanical analog of classical electromagnetic waves. For a thermal state, the photon-number variance is given by $\mathrm{Var}(\hat{n}) = \langle \hat{n} \rangle^2 + \langle \hat{n} \rangle$, which results in $g^{(2)}(0) = 2$. It reflects that the thermal light field is driven by photon-number fluctuations. Finally, we consider the displaced thermal state, which has a photon-number variance of $\mathrm{Var}(\hat{n}) = |\alpha|^2 + n_{\mathrm{th}}^2 + (2|\alpha|^2 + 1) n_{\mathrm{th}}$ [20]. Using this variance, we obtain

$$g^{(2)}_{\mathrm{DT}}(0)(|\alpha|^2, n_{\mathrm{th}}) = 2 - \left(\frac{|\alpha|^2}{|\alpha|^2 + n_{\mathrm{th}}} \right)^2 = 2 - \left(\frac{R}{R+1} \right)^2 , \tag{2.46}$$

where $R = \frac{|\alpha|^2}{n_{\mathrm{th}}}$ denotes the relation between the coherent and thermal photon number. Dependent on R, $g^{(2)}(0)$ lies in the interval $[1, 2]$.

2.2.2 Coherence Quantifier Based on the Density Matrix

In the previous section, we introduced the second-order correlation function, which is suitable for distinguishing different types of light sources. This characterization, however, relies solely on the photon statistics of the light field and therefore neglects the information contained in the off-diagonal elements of the density matrix. To address this limitation, we introduce a second set of quantifiers based on the complete density matrix. These quantifiers provide access to the coherence properties of the quantum state beyond its photon statistics.

The Purity

The first quantifier is the purity $\mathcal{P}$ [9, p. 107], defined by

$$\mathcal{P}(\hat{\rho}) = \mathrm{tr}(\hat{\rho}^2)\,, \tag{2.47}$$

which measures the degree of purity of a quantum state. The purity of a pure state equals one, while it decreases for mixed states. In the case of systems defined on finite-dimensional Hilbert spaces, there exists a well-defined maximally mixed state of minimal purity d^{-1}, where d denotes the dimension of $\mathcal{H}$. However, such a state does not exist in the case of light fields that are defined on infinite-dimensional Hilbert spaces. A second purity of particular interest is the purity of the state's closest incoherent counterpart $\mathcal{P}(\hat{\rho}_{\mathrm{Inc}})$, hereafter denoted by $\mathcal{P}_{\mathrm{Inc}}(\hat{\rho})$. The closest incoherent counterpart $\hat{\rho}_{\mathrm{Inc}}$ shares the same main diagonal matrix elements as $\hat{\rho}$ but lacks the off-diagonal matrix elements. Consequently, the relation between the two states depends on the chosen basis. In Fock representation $\mathcal{P}_{\mathrm{Inc}}(\hat{\rho})$ can be calculated from the density matrix of $\hat{\rho}$ via

$$\mathcal{P}(\hat{\rho}_{\mathrm{Inc}}) = \mathcal{P}_{\mathrm{Inc}}(\hat{\rho}) = \mathrm{tr}(\boldsymbol{\rho} \odot \boldsymbol{\rho})\,, \tag{2.48}$$

where $\boldsymbol{\rho}$ denotes the density matrix of $\hat{\rho}$ and $\odot$ represents the Hadamard product.

The Mixedness

Complementary to the purity, we define the linear entropy or mixedness

$$\mathcal{M}(\hat{\rho}) = 1 - \mathcal{P}(\hat{\rho})\,, \tag{2.49}$$

which quantifies the degree of mixing in the state.

The Quantum Coherence

Finally, we define the quantum coherence $\mathcal{C}$ as the distance between the quantum state $\hat{\rho}$ and its closest incoherent counterpart $\hat{\rho}_{\mathrm{Inc}}$. Using the squared Hilbert-Schmidt norm $\|\cdot\|_{\mathrm{HS}}^2$ as a measure [26], one obtains

$$\mathcal{C}(\hat{\rho}) = \|\hat{\rho} - \hat{\rho}_{\mathrm{Inc}}\|_{\mathrm{HS}}^2 = \sum_{m,n\in\mathbb{N},m\neq n} |\rho_{m,n}|^2 = \mathcal{P}(\hat{\rho}) - \mathcal{P}_{\mathrm{Inc}}(\hat{\rho})\,, \tag{2.50}$$

In terms of density matrices, this definition corresponds to the sum of the squared magnitudes of all off-diagonal matrix elements. Equivalently, it can be expressed as the difference between the purities of the full state $\hat{\rho}$ and its closest incoherent counterpart $\hat{\rho}_{\mathrm{Inc}}$. Quantum coherence therefore quantifies the amount of quantum superpositions present in a state, which renders it complementary to $g^{(2)}$. In particular, it can be used to assess the usefulness of a quantum state for a specific quantum-optical task, as we will discuss in chapter 6. The definition of $\mathcal{C}$, however, comes with certain limitations: First, quantum coherence depends on the chosen basis, since the difference between $\hat{\rho}$ and $\hat{\rho}_{\mathrm{Inc}}$ is basis dependent. Consequently, a common reference basis must be specified. Second, the definition of quantum coherence, used by us, is not universally applicable to all quantum states, as the monotonicity of $\mathcal{C}$ may be violated for certain classes of states or by certain operations [26][27]. Nevertheless, it remains valid for the classical Gaussian states considered throughout this work.

Together, the three quantifiers $\mathcal{C}$, $\mathcal{M}$ and $\mathcal{P}_{\mathrm{Inc}}$ satisfy the relation

$$\mathcal{C}(\hat{\rho}) + \mathcal{M}(\hat{\rho}) + \mathcal{P}_{\mathrm{Inc}}(\hat{\rho}) = 1\,. \tag{2.51}$$

3 Theoretical Foundations - Exciton-Polaritons in a Microcavity

A second fundamental aspect of quantum optics concerns the study of interactions between light fields and matter. In the regime of strong coupling, the interaction of a photon with an exciton leads to the formation of an exciton-polariton, a bosonic light-matter quasiparticle that exhibits properties of both constituents. In this work, we focus exclusively on exciton-polaritons in a planar microcavity, whose theoretical foundations are discussed in this chapter. We begin with the concept of quantum well excitons, introduced in section 3.1. Subsequently, we consider planar microcavities, described in section 3.2, which are employed to enhance the light-matter interaction. Attaining the strong-coupling regime leads to the formation of exciton-polaritons, discussed in section 3.3. In section 3.4, we extend the discussion to the condensation process of a non-resonantly excited polariton population into a Bose-Einstein condensate-like state. Finally, in section 3.5, we address strategies for optimizing both the condensation efficiency and the coherence properties of the condensate through tailored excitation geometries.

3.1 Excitons in a Semiconductor

Semiconductors are materials whose electrical conductivity lies between that of isolators and metals. The ability to control their conductivity by external fields makes them a cornerstone of modern technology. While the dispersion relation of a semiconductor $E(\vec{k})$ is complex in general, it can often be approximated by parabolic bands in the proximity of the Γ-point [28, p. 90-92]. For the case of $GaAs$, which is used throughout this work, the conduction band is s-like, whereas the valence band is p-like and split into the light-hole (LH), heavy-hole (HH), and the energetically lower split-off (SO) bands. The corresponding band structure is depicted schematically in figure 3.1. Based on the dispersion relation, the effective electron mass m_e^* is defined as

$$m_\mathrm{e}^* = \hbar^2 \left(\frac{\mathrm{d}^2 E(k)}{\mathrm{d}k^2} \right)^{-1} , \tag{3.1}$$

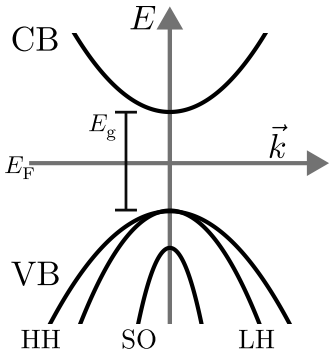

Figure 3.1: Schematic of the *GaAs* bandstructure in parabolical approximation near the Γ-point. The band structure consists of the p-like valence band (VB), split into the heavy-hole band (HH), light-hole band(LH), and split-off band (SO), and the s-like conduction band (CB). Valence bands and conduction band are separated by the band gap of energy E_g. The Fermi level with the energy E_F lies within the band gap. Adapted from [28, p. 92]

which enables a description of crystal electrons analog to that of free electrons. When a photon excites an electron from the valence to the conduction band, the electron leaves behind a positively charged quasiparticle, referred to as hole, with charge $+e$ and effective mass $m_h^* = -m_e^*$. Due to their opposite charges, an electron and a hole with sufficiently low kinetic energy can bind via Coulomb interaction, forming a new quasi-particle, referred to as an exciton. Depending on the exciton binding energy $E_{x,B}$, one distinguishes between weakly bound Wannier-Mott-excitons, typically found in inorganic semiconductors, with binding energies of the order of several meV, and strongly bound Frenkel excitons, usually found in organic semiconductors, with typical binding energies of several hundred meV [28, p. 123-126]. Due to their low binding energy, Wannier-Mott excitons can be delocalized over many lattice constants, while Frenkel excitons usually localize at individual lattice sites. In this work, we focus exclusively on Wannier-Mott excitons. In a bulk semiconductor, the wave functions of a Wannier-Mott exciton can be derived analogously to the hydrogen problem. This yields the exciton binding energies

$$E_{x,B}^n = -\frac{\mu_x}{m_0 \epsilon_r^2} \frac{R_H}{n^2}\,, \tag{3.2}$$

connected to excitons with the radii

$$r_x^n = \frac{m_e}{\mu_x} \epsilon_r a_B n^2\,, \tag{3.3}$$

where n denotes the principal exciton quantum number, $\mu_x = \frac{m_e^* m_h^*}{m_e^* + m_h^*}$ is the reduced effective mass, m_e is the free electron mass, R_H is the Rydberg energy, and a_B is

the atomic Bohr radius. Further, the dielectric screening constant ϵ_r accounts for screening of the Coulomb interaction by the surrounding lattice atoms. Including the band gap energy E_g and the kinetic energy in the center-of-mass system, the exciton dispersion relation can be written as

$$E_\mathrm{x}^n(\vec{K}) = E_\mathrm{g} - E_\mathrm{x,B}^n + \frac{\hbar^2|\vec{K}|^2}{2M_\mathrm{x}}\,, \tag{3.4}$$

where $\vec{K}$ denotes the center-of-mass wave vector and $M_\mathrm{x} = m_\mathrm{e}^* + m_\mathrm{h}^*$ is the total mass. In the next step, we consider excitons confined in a planar two-dimensional quantum well. The confinement leads to the quantization of the out-of-plane wave vector component $k_\perp$, while the in-plane component $k_\parallel$ remains continuous. Additionally, the exciton wave function is compressed by the potential barriers [29, p. 139-140]. For narrow quantum wells with thickness $d \ll r_\mathrm{x}^n$, this confinement modifies the binding energies and the Bohr radii according to $E_{\mathrm{x,B_{2D}}}^n = 4E_{\mathrm{x,B_{3D}}}^n$ and $a_{\mathrm{B_{2D}}} = \frac{1}{2}a_{\mathrm{B_{3D}}}$. For the case $d < r_\mathrm{x}^n$ or for finite barrier potentials, the binding energy initially increases with decreasing well width due to the compression of the wave function. However, as the wave function begins to tunnel into the barrier, the effective width of the wave function increases, and the binding energy again decreases.

3.2 Planar Microcavities

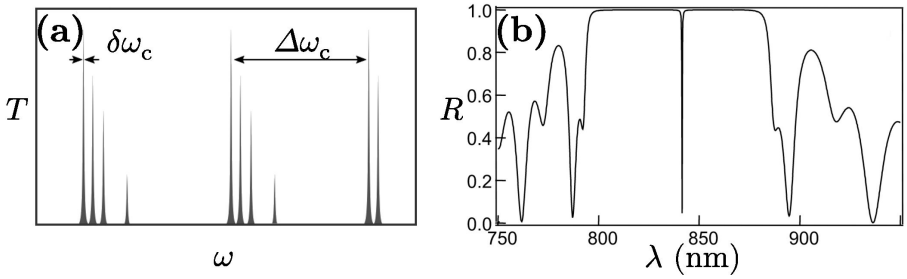

Figure 3.2: Discrete transmission spectrum of the longitudinal modes inside a microcavity (a) and the reflection spectrum of a planar microcavity consisting of two DBR mirrors. The overall reflectivity in (b) displays the structure of a single DBR mirror, while the reflectivity dip at 841 nm corresponds to the resonant cavity mode. Adapted from [29, p. 10].

After introducing quantum well excitons in the previous section, we now consider their coupling to a light field. The interaction between a light field and semiconductor excitons without further amplification is, however, relatively weak. To enhance both

the interaction time and the interaction strength between excitons and photons, we embed the quantum well in a microcavity. The simplest cavity type is the planar Fabry-Perot resonator, consisting of two plane-parallel mirrors of equal reflectivity R, separated by a distance L_c. This spatial confinement discretizes the frequency spectrum of the allowed resonator modes, as exemplarily illustrated in figure 3.2 (a). The properties of a resonator mode of frequency ω_c are commonly characterized via two key quantities [29, p. 2-3]. The first is the quality factor, or Q-factor, defined as

$$Q = \frac{\omega_\mathrm{c}}{\delta\omega_\mathrm{c}}\,, \tag{3.5}$$

where $\delta\omega_\mathrm{c}$ denotes the linewidth of the resonator mode. For a $\lambda/2$ microcavity, the Q-factor can be interpreted as the average number of cavity round-trips a photon performs inside the cavity before it escapes the cavity through one of the mirrors. The corresponding photon lifetime is given by $\tau_\mathrm{c} = \frac{Q}{\omega_\mathrm{c}}$. The second important quantity is the finesse F, defined as

$$F = \frac{\Delta\omega_\mathrm{c}}{\delta\omega_\mathrm{c}} = \frac{\pi\sqrt{R}}{1-R}\,, \tag{3.6}$$

where $\Delta\omega_\mathrm{c}$ is the free spectral range. When the finesse is primarily limited by mirror losses, it can be used to estimate the enhancement of the electric field inside the cavity relative to the field outside:

$$\frac{I_\mathrm{Cav}}{I_\mathrm{Out}} \simeq \frac{F}{\pi\sqrt{R}}. \tag{3.7}$$

Both the Q-factor and the finesse rely on high-quality mirrors with very high reflectivity ($R \approx 1$). A suitable mirror design for achieving such high reflectivities is the distributed Bragg reflector (DBR) [29, p. 54-58]. A DBR structure consists of a periodic stack of two alternating dielectric layers with low and high refractive indices n_L and n_H. At each interface, the incident light is partially transmitted and partially reflected. When optimized for a central wavelength $\bar{\lambda}$, the layer thicknesses satisfy the condition

$$n_\mathrm{L} \cdot d_\mathrm{L} = n_\mathrm{H} \cdot d_\mathrm{H} = \frac{(2j-1)\bar{\lambda}}{4},\ j \in \mathbb{N}\,. \tag{3.8}$$

The condition ensures the high reflectivity of the mirrors, as the relative phases between the partial beams are modified in a manner such that the transmitted partial beams interfere destructively while the reflected partial beams interfere constructively. As a result, the system behaves as a one-dimensional photonic crystal exhibiting a stop band with reflectivity $R \approx 1$ around $\bar{\lambda}$. Outside this stop band, the reflectivity

decreases under oscillations, with the reflectivity minima commonly referred to as Bragg minima. Using DBR mirrors, the cavity eigenfrequencies ω_c satisfy the resonance condition

$$\frac{L_\mathrm{DBR}}{n_\mathrm{c} c}(\omega_\mathrm{c} - \bar{\omega}) + k_\perp L\mathrm{c} = j\pi,\ j \in \mathbb{N}\,, \tag{3.9}$$

where $L_\mathrm{DBR} = \frac{n_\mathrm{L} n_\mathrm{H} \bar{\lambda}}{2(n_\mathrm{H} - n_\mathrm{L})}$ denotes the effective length of the Bragg mirror, n_c is the refractive index of the cavity layer, and $k_\perp = \frac{n_\mathrm{c} 2\pi}{\lambda_\mathrm{c}}$ is the out of plane component of the wave vector [29, p. 61]. The eigenfrequencies are accompanied by a narrow dip in the reflection spectrum of the cavity reaching almost $R = 0$, as the transmitted light fields interfere constructively. An example of a complete cavity spectrum is depicted in figure 3.2 (b). The main difference between a macroscopic cavity and a microcavity lies in the spacing L_c. A macroscopic cavity has a large spacing of $L_\mathrm{c} \gg \bar{\lambda}$, leading to a dense frequency distribution of resonator modes. In contrast, microcavities feature very small cavity lengths and therefore exhibit a large free spectral range, such that typically only a single cavity mode overlaps with the stop band of the Bragg mirrors.

According to [7], the dispersion relation of a cavity photon is given by

$$E(\vec{k}) = \frac{\hbar c}{n_\mathrm{c}} \sqrt{k_\perp^2 + k_\parallel^2}\,. \tag{3.10}$$

Near $k_\parallel = 0$, this relation can be approximated by a parabolic dispersion

$$E(\vec{k}) = E(k_\parallel = 0) + \frac{\hbar^2 k_\parallel^2}{2 m_\mathrm{c}^*}\,, \tag{3.11}$$

which introduces the effective cavity photon mass

$$m_\mathrm{c}^* = \left(\frac{n_\mathrm{c}}{c}\right)^2 E(k_\parallel = 0)\,. \tag{3.12}$$

The effective cavity photon mass is typically on the order of $10 \times 10^{-5}\, m_\mathrm{e}$.

3.3 Exciton-Polaritons in a Microcavity

In the next step, we place $GaAs$ quantum wells at the anti-nodes of the cavity mode and consider the coupled system. The following description is based on [7] and [30, p. 50-61]. The Hamiltonian of the coupled system is given by

$$\hat{H} = \sum_{k_\parallel \in 1.\ \mathrm{B.Z}} E_\mathrm{c}(k_\perp, k_\parallel)\hat{a}^\dagger_{k_\parallel}\hat{a}_{k_\parallel} + E_\mathrm{x}\hat{b}^\dagger_{k_\parallel}\hat{b}_{k_\parallel} + \hbar g(\hat{a}^\dagger_{k_\parallel}\hat{b}_{k_\parallel} + \hat{b}^\dagger_{k_\parallel}\hat{a}_{k_\parallel})\,, \tag{3.13}$$

where $(\hat{a}, \hat{a}^\dagger)$ and $(\hat{b}, \hat{b}^\dagger)$ denote the bosonic annihilation and creation operators of the cavity photon and the exciton, respectively, and $\hbar g$ is the Rabi energy. Furthermore, we assume that the exciton density remains below the Mott density, allowing us to treat excitons as bosons. The first two terms describe the energy contributions of cavity photon and exciton, while the third term represents the coupling between both, determined by the Rabi energy. The Rabi energy is proportional to the transition matrix element between the excitonic and the photonic state. In dipole-approximation, the matrix element is determined by $\langle X_{k_\parallel}|\vec{d}_\mathrm{x}\vec{E}_\mathrm{c}|C_{k_\parallel}\rangle$, where $\vec{d}_\mathrm{x}$ is the exciton dipole moment and $\vec{E}_\mathrm{c}$ is the electric field vector of the cavity field. Further, mainly ground state excitons couple to the light field as the exciton oscillator strength decreases with n^{-3} [31, p. 276]. In general, coupling is restricted to modes of identical wave vector. However, as the spatial confinement inside the quantum well breaks the translational symmetry along the out-of-plane axis, this condition reduces to equal $k_\parallel$. Consequently, the Hamiltonian decomposes into a set of independent Hamiltonians $H_{k_\parallel}$, each corresponding to a fixed $k_\parallel$. These Hamiltonians can be diagonalized individually by introducing a set of new operators

$$\begin{aligned} \hat{l}_{k_\parallel} &= X(k_\parallel)\hat{b}_{k_\parallel} + C(k_\parallel)\hat{a}_{k_\parallel} \\ \hat{u}_{k_\parallel} &= -C(k_\parallel)\hat{b}_{k_\parallel} + X(k_\parallel)\hat{a}_{k_\parallel} \end{aligned} \tag{3.14}$$

which translates the Hamiltonians into

$$\hat{H}_{k_\parallel} = E_\mathrm{LP}(k_\parallel)\hat{l}^\dagger_{k_\parallel}\hat{l}_{k_\parallel} + E_\mathrm{UP}(k_\parallel)\hat{u}^\dagger_{k_\parallel}\hat{u}_{k_\parallel}\,. \tag{3.15}$$

The new operators $\hat{l}_{k_\parallel}$ and $\hat{u}_{k_\parallel}$ correspond to the annihilation operators of the new eigenmodes of the coupled system, namely the exciton polaritons of the lower and upper branches. The excitonic and photonic contributions to the polaritons of the lower polariton branch are determined by the Hopfield coefficients X and C, whereas the connection is inverted for the polaritons of the upper polariton branch. The Hopfield coefficients satisfy the normalization condition $|X|^2 + |C|^2 = 1$ and follow

from the relations [32]

$$|C(k_\parallel)|^2, |X(k_\parallel)|^2 = \frac{1}{2}\left(1 \mp \frac{\Delta_{\text{c-x}}(k_\parallel)}{\sqrt{(2\hbar g)^2 + \left(\Delta_{\text{c-x}}(k_\parallel)\right)^2}}\right), \tag{3.16}$$

where $\Delta_{\text{c-x}}(k_\parallel) = E_{\text{c}}(k_\parallel) - E_{\text{x}}(k_\parallel)$ denotes the energy detuning between the cavity resonance energy and the exciton energy. The corresponding polariton dispersions of the lower and upper branches $E_{\text{LP}}(k_\parallel)$ and $E_{\text{UP}}(k_\parallel)$ are given by

$$E_{\text{LP,UP}} = \frac{1}{2}\left(E_{\text{c}}(k_\parallel) + E_{\text{x}}(k_\parallel) \mp \sqrt{(2\hbar g)^2 + \left(\Delta_{\text{c-x}}(k_\parallel)\right)^2}\right). \tag{3.17}$$

Based on equation (3.16), we note two important aspects: First $|X|^2$ becomes minimal at $k_\parallel = 0$ and increases as $\Delta_{\text{c-x}}(k_\parallel)$ increases with increasing $|k_\parallel|$. Second, the minimum becomes more pronounced with decreasing $\Delta_{\text{c-x}}(0)$. An illustration of this relation based on three exemplary initial detunings of $\Delta_{\text{c-x}}(0) = -10\,\text{meV}$, $0\,\text{meV}$, and $10\,\text{meV}$ is depicted in the top row of figure 3.3. Considering the effect of

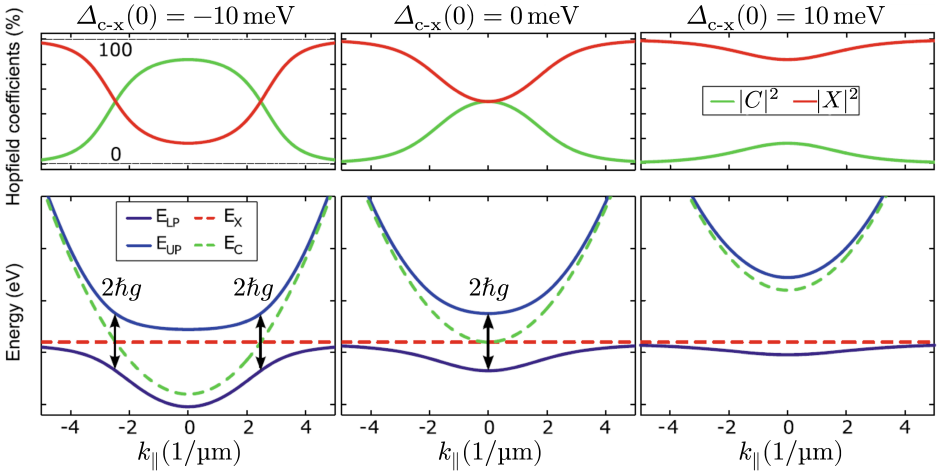

Figure 3.3: Hopfield coefficients and polariton dispersion relations for the three initial detunings $\Delta_{\text{c-x}}(0) = -10\,\text{meV}$, $0\,\text{meV}$, and $10\,\text{meV}$. Adapted from [33]

these changes on the polariton dispersion of the lower polariton branch, this means that the dispersion flattens with increasing $\Delta_{\text{c-x}}(0)$ or increasing $k_\parallel$ as the polaritons become more excitonic. For the polaritons of the upper polariton branch, the situation is inverted as they become more photonic. The dispersion relations of both branches are illustrated in the bottom panels of figure 3.3. At the crossing points of exciton and photon dispersion, corresponding to $\Delta_{\text{c-x}}(k_\parallel) = 0$, the energy difference between the two branches achieves a minimal value of the double Rabi energy.

Consequently, one observes for $\Delta_{\text{c-x}}(0) < 0$ two symmetrically placed crossing points at finite $|k_{\|}| > 0$, for $\Delta_{\text{c-x}}(0) = 0$ one crossing point at $k_{\|} = 0$ and for $\Delta_{\text{c-x}}(0) > 0$ none. As the effective masses of the quantum well exciton and cavity photon are different, the Hopfield coefficients also define the effective polariton masses, given by

$$\frac{1}{m^*_{\text{LP}}} = \frac{|C|^2}{m^*_{\text{c}}} + \frac{|X|^2}{m^*_{\text{x}}} \text{ and } \frac{1}{m^*_{\text{UP}}} = \frac{|X|^2}{m^*_{\text{c}}} + \frac{|C|^2}{m^*_{\text{x}}} \,. \tag{3.18}$$

This allows a modification of the effective polariton mass over a broad range by adjusting the detuning as the effective exciton mass is two to three orders larger than the effective cavity photon mass.

So far, we have considered the idealized case of a closed system without losses. In practice, however, photons may escape the cavity due to imperfect mirrors, and excitons may decay via non-radiative channels. These losses can be phenomenologically described by introducing the damping constants γ_{c} and γ_{x}. This leads to the two modified dispersion relations

$$E_{\text{LP,UP}} = \frac{1}{2}\left(E_{\text{c}} + E_{\text{x}} + i\left(\gamma_{\text{c}} + \gamma_{\text{x}}\right) \mp \sqrt{\left(2\hbar g\right)^2 + \left(\Delta_{\text{c-x}} + i\left(\gamma_{\text{c}} - \gamma_{\text{x}}\right)\right)^2}\right) . \tag{3.19}$$

Consequently, the system must fulfill the condition $\hbar g > \frac{|\gamma_{\text{c}} - \gamma_x|}{2}$ to reach the strong-coupling regime, characterized by a splitting of the real parts of the eigen energies. As for the previous quantities, the effective polariton decay rates depend on the Hopfield coefficients and are given by

$$\begin{aligned} \gamma_{\text{LP}} &= \gamma_{\text{c}}|C|^2 + \gamma_{\text{x}}|X|^2 \\ \gamma_{\text{UP}} &= \gamma_{\text{x}}|C|^2 + \gamma_{\text{c}}|X|^2 \,. \end{aligned} \tag{3.20}$$

As the typical cavity photon lifetime lies in the picosecond range, while the exciton lifetime amounts to a few nanoseconds, adjusting the detuning allows modifying the polariton lifetime over a broad range.

3.4 Polariton Condensation in a Population of Non-Resonant Excited Polaritons

Until the beginning of the last century, matter was commonly classified into three phases: solid, liquid, and gaseous. This classical picture was fundamentally challenged with the emergence of quantum mechanics, which paved the way to a variety of new exotic phases. One of the most prominent examples is the Bose-Einstein

condensate (BEC), in which a macroscopic number of bosonic particles occupies a single quantum state, such that the system is described by a single macroscopic wavefunction [34]. Further, the condensation process is accompanied by effects like superfluidity [35] and off-diagonal long-range order [36], which renders BECs potentially interesting for fundamental research. Crucial condition for the condensation process is the spatial overlap of the individual particle wavefunctions [37, p. 264-266]. This leads to the critical temperature

$$T_\mathrm{c} = \frac{2\pi\hbar^2}{k_\mathrm{B} m_\mathrm{b}} \frac{1}{(\nu \cdot \zeta(3/2))^{2/3}}\,, \tag{3.21}$$

where we use the thermal de-broglie wavelength

$$\lambda_\mathrm{DB} = \sqrt{\frac{2\pi\hbar^2}{m_\mathrm{b} k_\mathrm{B} T}}\,, \tag{3.22}$$

to estimate the size of the particle wavefunction. In this context, m_b denotes the particle mass, k_B the Boltzmann constant, T the temperature and ν^{-1} the particle density. Consequently, T_c decreases at constant particle density with increasing temperature and particle mass. The condensation, therefore requires either low temperatures or light particles. Historically, Bose-Einstein condensates were first realized experimentally in a vapor of rubidium-87 atoms cooled to approximately 170 nK [38]. However, achieving such temperatures requires complex experimental techniques, and additional methods must be employed to detect the condensation process, as atomic vapors do not emit light directly. In contrast, exciton-polaritons can condense at much higher temperatures due to their low effective mass. Typically, the maximal temperature is not limited by the size of the particle wavefunctions but by dissociation of the excitonic component. This enables polariton condensation in inorganic semiconductors, such as $GaAs$, at regular cryogenic temperatures of a few K [39], while room-temperature condensation has been observed in organic semiconductors [40]. Polaritons not only simplify the creation of a condensate but also allow direct optical access to its properties. This is possible as polaritons decay under emission of photons that inherit the properties of the polaritons. Lastly, it is important to note that polaritons in a microcavity do not condensate into a true Bose-Einstein condensate, but only a Bose-Einstein condensate-like state, hereafter referred to as polariton condensate. One of the reasons is that a true BEC would require complete thermalization of the system, a condition that does not hold due to the short polariton lifetimes. Consequently, the system is in a constant non-equilibrium and the average polariton population is governed by the balance between gains and losses. Further explanations about the phase transition can, for example, be found in [29, p. 320-334].

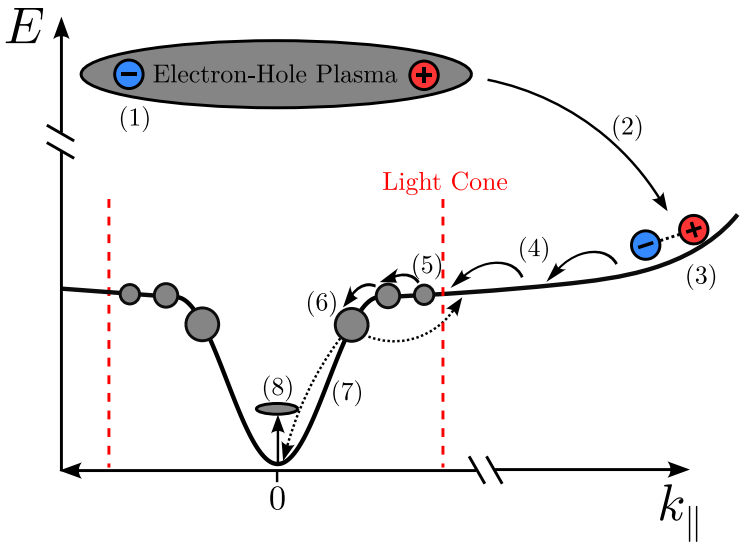

Figure 3.4: Schematic of the polariton condensation process via non-resonant excitation. The individual steps (1)-(8) are described in detail in the text. Adapted from [33, 41]

Experimentally, polariton condensates can be generated using either resonant or non-resonant optical pumping. While resonant excitation allows the direct transfer of laser properties to the condensate, our focus lies on the intrinsic buildup of coherence. For this reason, we focus on non-resonant excitation. The condensation process of polaritons in the lower polariton branch under non-resonant pumping is illustrated schematically in figure 3.4. The description is based on [29, p. 335-338]. A laser excites the sample non-resonantly through one of the upper Bragg minima, generating a hot plasma of free excitons and holes with energies far above the dispersion of the lower polariton branch (1). These carriers subsequently lose a major part of their kinetic energy through inelastic scattering with optical phonons (2) until their kinetic energies become sufficiently low for electrons and holes to bind via Coulomb interaction and to form excitons (3). Additional scattering events, now primarily with acoustic phonons, further reduce the kinetic energy of the exciton (4) until the exciton wave vector enters the light cone. At this point, the excitons couples to the cavity field and form polaritons (5). As polaritons approach $k_{||} = 0$, their photonic fraction increases. This complicates further relaxation for two reasons: First, the increasing photonic fraction decreases the polariton lifetime, so a polariton has less time to relax before it decays. Second, the higher photonic fraction changes the dispersion, leading to a narrow dip around $k_{||} = 0$ that decreases the local density of states which is inversely proportional to the curvature of the dispersion relation. Together these two aspects lead to the formation of a bottleneck region (6), where

polaritons tend to decay rather than relax further towards the ground state. Only at sufficiently high polariton densities, polaritons can relax via polariton-polariton scattering to the ground state (7). These initial polariton population then serves as a seed for further stimulated polariton-polariton scattering into the ground state, since the scattering rate scales with $1 + n_{\mathrm{f}}$, where n_{f} denotes the population of the final state [7]. As a consequence, the ground-state population increases highly nonlinearly once the system is driven above the condensation threshold. Finally, the polariton-polariton interactions - dominated by the repulsive interactions between polaritons of equal spin - lead to a blueshift of the condensate mode relative to the ground state of the lower polariton branch (8).

Experimentally, the condensation process can be identified spectroscopically by three characteristic signatures. First, emission intensity increases by several orders of magnitude while the emission narrows in momentum space around $k_{\parallel} = 0$. Second, the linewidth of the dispersion narrows, reflecting the macroscopic occupation of a single quantum state. Third, the formation of the condensate mode is accompanied by a blueshift. In addition to these spectroscopic signatures, the emergence of long-range order in the condensate also modifies its coherence properties. The coherence properties can likewise be probed through the emitted radiation and may be observed using techniques such as homodyne detection, which will be discussed in the following chapter.

3.5 Optical Polariton Trapping

Finally, we discuss the possibility of tailoring the polariton potential landscape all-optically. We begin by considering the excitation beam, which leads not only to the creation of polaritons but also a variety of other quasi-particles, including free electrons, free holes, or dark excitons of $k_{\parallel}$ outside the light cone. These excitations are collectively referred to as reservoir particles. From the perspective of the polaritons, the reservoir particles form an effective potential landscape, as interactions between polaritons and reservoir particles are predominantly repulsive. Furthermore, the potential landscape can be regarded as quasi-static, since the reservoir particles possess significantly larger mass than the polaritons. The local density of the reservoir particles depends on the spatial intensity distribution of the excitation beam. Consequently, tailored potential structures can be created all-optically by employing excitation beams with appropriately designed intensity profiles. Such engineered potential landscapes have been used in a wide range of applications, ranging from controlling the flow of a single polariton population [42] to the realization of artificial polariton-condensate lattices [43, 44] Another application, particularly relevant for this work, is the manipulation of the condensation process

by trapping the polariton population with an annular-shaped excitation beam. This approach not only lowers the condensation threshold but also spatially separates the condensate from the incoherent reservoir, thereby minimizing potential interactions and improving its coherence properties [45][46, 47]. The corresponding experimental investigations are presented in chapter 7.

4 Experimental Methods - Homodyne Detection

In the first chapter, we established the theoretical foundations to describe light fields in quantum optics and to quantifier their coherence properties. In the present chapter, we introduce balanced homodyne detection, a technique that enables the experimental reconstruction of the quantum state of a light field. We begin with the theoretical principles underlying the four-port and eight-port detection schemes. Subsequently, we discuss the design and alignment of the corresponding experimental setups. The chapter concludes with the calculation of quadratures, the reconstruction of quantum-state representations, and the evaluation of relevant quantifiers.

4.1 Theoretical Foundations

4.1.1 The Coupling of Light Fields on a Beam Splitter

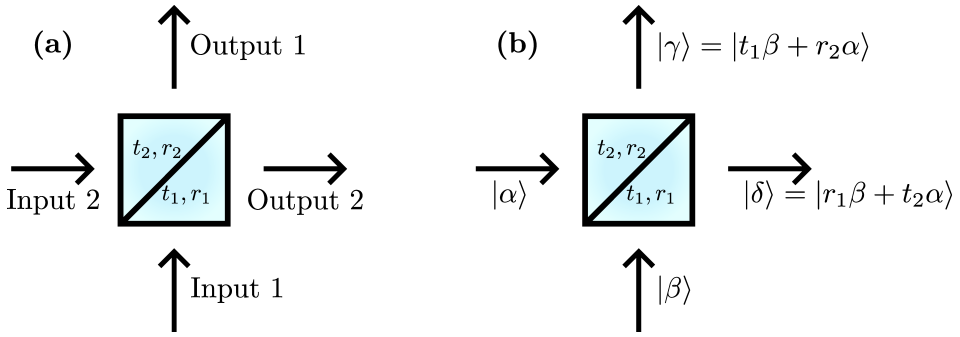

Figure 4.1: Definition of the beam splitter input and output ports (a) and the associated phase space variables (b).

One of the most fundamental optical elements in quantum optics - and the basis of homodyne detection - is the beam splitter [11, p. 350-355]. It couples two light fields entering through the input ports to two, in general, entangled, light fields exiting through the output ports. For simplicity, we restrict our description to the coupling of two initially uncorrelated single-mode light fields on a lossless, non-polarizing

beam splitter. The beam splitter is characterized by the complex reflection and transmission coefficients r_1, t_1, and r_2, t_2. The corresponding notation is illustrated in figure 4.1 (a). Since the beam splitter is assumed to be lossless, these coefficients are not independent, but connected by the relations

$$\begin{aligned} |t_1|^2 + |r_1|^2 &= 1 \\ |t_2|^2 + |r_2|^2 &= 1 \\ t_1 r_2^* + t_2^* r_1 &= 0\,. \end{aligned} \tag{4.1}$$

Transformation Rule of the Annihilation Operator

In the first scenario, we describe the beam splitter transformation in terms of the annihilation operators $\hat{a}_{\mathrm{I},1}$ and $\hat{a}_{\mathrm{I},2}$, associated with the two input modes. The corresponding operators for the output modes are then given by

$$\begin{aligned} \hat{a}_{\mathrm{O},1} &= t_1 \hat{a}_{\mathrm{I},1} + r_2 \hat{a}_{\mathrm{I},2} \\ \hat{a}_{\mathrm{O},2} &= r_1 \hat{a}_{\mathrm{I},1} + t_2 \hat{a}_{\mathrm{I},2}\,. \end{aligned} \tag{4.2}$$

Conversely, by applying the relations in equation (4.1), the operators of the input modes can be expressed in terms of the operators of the output modes,

$$\begin{aligned} \hat{a}_{\mathrm{I},1} &= t_1^* \hat{a}_{\mathrm{O},1} + r_1^* \hat{a}_{\mathrm{O},2} \\ \hat{a}_{\mathrm{I},2} &= r_2^* \hat{a}_{\mathrm{O},1} + t_2^* \hat{a}_{\mathrm{O},2}\,. \end{aligned} \tag{4.3}$$

Transformation Rule of the Quantum States

In the second scenario, we consider the beam splitter transformation of quantum states. We begin with the simplest case: the coupling of two uncorrelated coherent light fields. Using the notation shown in figure 4.1 (b), the joint quantum state is given by $|\Psi_\mathrm{I}\rangle = |\beta\rangle \otimes |\alpha\rangle$. Since coherent states transform under a beam splitter in the same way as classical waves, the individual output states remain uncorrelated, and the joint output state takes the form

$$|\Psi_\mathrm{O}\rangle = |\gamma\rangle \otimes |\delta\rangle = |t_1\beta + r_2\alpha\rangle \otimes |r_1\beta + t_2\alpha\rangle\,. \tag{4.4}$$

Analogous to the annihilation operator, we obtain the joint input state in terms of the individual output states

$$|\Psi_\mathrm{I}\rangle = |\beta\rangle \otimes |\alpha\rangle = |t_1^*\gamma + r_1^*\delta\rangle \otimes |r_2^*\gamma + t_2^*\delta\rangle\,, \tag{4.5}$$

using again the equations in (4.1). The inversion is possible because the quantum states at the two output ports are uncorrelated. In the next step, we generalize the transformation rule to two uncorrelated but otherwise arbitrary input light fields whose joint state is described by the density operator $\hat{\rho}_{\mathrm{I}} = \hat{\rho}_{\mathrm{I},1} \otimes \hat{\rho}_{\mathrm{I},2}$. First, we represent the density operator of the input state in the basis of the coherent states using the P distribution

$$\hat{\rho}_{\mathrm{I}} = \int \mathrm{d}^2\alpha \int \mathrm{d}^2\beta \, P_1(\beta) P_2(\alpha) |\beta\rangle\langle\beta| \otimes |\alpha\rangle\langle\alpha| \,. \tag{4.6}$$

The representation allows us to separate the beam-splitter transformation, which acts on the basis vectors, from the information about the state, which is encoded in the P distributions. The resulting output state $\hat{\rho}_{\mathrm{O}}$ is given by

$$\hat{\rho}_{\mathrm{O}} = \int \mathrm{d}^2\alpha \int \mathrm{d}^2\beta \, P_1(\beta) P_2(\alpha) |r_2\alpha + t_1\beta\rangle\langle r_2\alpha + t_1\beta| \otimes |t_2\alpha + r_1\beta\rangle\langle t_2\alpha + r_1\beta| \,. \tag{4.7}$$

Finally, we express $\hat{\rho}_{\mathrm{O}}$ in terms of the phase space variables of the output modes γ and δ,

$$\hat{\rho}_{\mathrm{O}} = \int \mathrm{d}^2\gamma \int \mathrm{d}^2\delta \, P_1(t_1^*\gamma + r_1^*\delta) P_2(r_2^*\gamma + t_2^*\delta) |\gamma\rangle\langle\gamma| \otimes |\delta\rangle\langle\delta| \,, \tag{4.8}$$

using the relations given in (4.1). The output modes are typically entangled as the phase-space integration over the joined P-distribution $P_{\mathrm{j}}(\gamma, \delta) = P_1(t_1^*\gamma + r_1^*\delta) \cdot P_2(r_2^*\gamma + t_2^*\delta)$ couples the phase-space variables of the two output modes.

4.1.2 Quadrature Sampling with a Four-Port Detector

The beam splitter constitutes the fundamental element of homodyne detection, which enables the sampling of the quadrature operator introduced in equation (2.25). The most basic homodyne detection scheme is the four-port detector first used by H. P. Yuen and V. W. S. Chan [48, 49], which samples a single quadrature. The following derivation is adapted from Lüders et al. [50]. We begin with a lossless beam splitter with the real transmission and reflection coefficients $t_1 = t_2 = \frac{1}{\sqrt{2}}$ and $r_1 = -r_2 = \frac{1}{\sqrt{2}}$. The relative π-phase shift between the reflection coefficients follows from energy conservation [51]. The annihilation operators of the output modes are then given by

$$\begin{aligned} \hat{a}_{\mathrm{O},1} &= \frac{1}{\sqrt{2}} \left(\hat{a}_{\mathrm{I},1} - \hat{a}_{\mathrm{I},2} \right) \\ \hat{a}_{\mathrm{O},2} &= \frac{1}{\sqrt{2}} \left(\hat{a}_{\mathrm{I},1} + \hat{a}_{\mathrm{I},2} \right) \,. \end{aligned} \tag{4.9}$$

In the next step, we place detectors at both output ports and measure the intensity difference, which is proportional to the photon-number difference.

$$\begin{aligned} \Delta I &= I_{\mathrm{O},2} - I_{\mathrm{O},1} \\ \propto \Delta N &= \hat{a}^\dagger_{\mathrm{O},2}\hat{a}_{\mathrm{O},2} - \hat{a}^\dagger_{\mathrm{O},1}\hat{a}_{\mathrm{O},1} \\ &= \frac{1}{2}\left[\left(\hat{a}^\dagger_{\mathrm{I},1} + \hat{a}^\dagger_{\mathrm{I},2}\right)\left(\hat{a}_{\mathrm{I},1} + \hat{a}_{\mathrm{I},2}\right) - \left(\hat{a}^\dagger_{\mathrm{I},1} - \hat{a}^\dagger_{\mathrm{I},2}\right)\left(\hat{a}_{\mathrm{I},1} - \hat{a}_{\mathrm{I},2}\right)\right] \\ &= \hat{a}^\dagger_{\mathrm{I},1}\hat{a}_{\mathrm{I},2} + \hat{a}^\dagger_{\mathrm{I},2}\hat{a}_{\mathrm{I},1}\,. \end{aligned} \tag{4.10}$$

Interestingly, the intensity difference does not vanish but depends on the products of the two input modes. In the final step, we assume that the light field entering input port 1 is in a coherent state with a large average photon number. In this limit, we can treat the light field classically and replace the annihilation operator by a complex field amplitude, $\hat{a}_{\mathrm{I},1} \to |\alpha|\mathrm{e}^{i\varphi}$. This strong, coherent light field is referred to as the local oscillator (LO). The light field entering input port 2 represents the signal and remains treated quantum mechanically. Substituting this approximation yields the final expression for the intensity difference

$$\Delta I \propto |\alpha|\left(\hat{a}_{\mathrm{I},2}\mathrm{e}^{-i\varphi} + \hat{a}^\dagger_{\mathrm{I},2}\mathrm{e}^{i\varphi}\right)\,, \tag{4.11}$$

which is proportional to the quadrature operator defined in equation (2.25), but amplified by the amplitude of the local oscillator. The quadrature sampling axis is determined by the relative phase between the local oscillator and the signal φ. For a fixed phase φ, the distribution of sampled quadratures corresponds to the associated marginal distribution of the signal state's Wigner distribution [11, p. 143]. The amplification by the local oscillator enables the study of weak optical fields using detectors with conventional quantum efficiencies. An alternative derivation based on the transformation of the quantum states can be found, for example, in [11, p. 358-360]. Homodyne detection is intrinsically mode-selective and detects only those modes that overlap with the local oscillator in real space, momentum space, spectral domain, and polarization. This property enables highly selective measurements of specific optical modes.

So far, we have considered time-independent fields. Employing a pulsed local oscillator, a quadrature corresponds to the difference signal integrated over the pulse duration. This provides several important advantages. First, the achievable temporal resolution is determined by the pulse duration and is therefore independent of the detector bandwidth, which is typically several orders of magnitude slower. Second, the signal amplification depends on the peak amplitude of the pulse, leading to amplification factors several orders of magnitude larger than those achievable with a continuous-wave laser of comparable average power. Third, the quadrature sampling

rate is theoretically only upper bounded by the repetition rate of the laser pulses and could reach, in principle, rates up to several GHz. Therefore, the quadrature sampling rate is in practice typically not limited by the local oscillator but by the detection electronics. To clearly distinguish between theory and experiment, we denote an experimentally acquired quadrature from now on as X. Further, we denote the phase associated with it as Φ.

4.1.3 Quadrature Pair Sampling with an Eight-Port Detector

Up to this point, we have discussed the four-port detector, which samples the quadrature operator $\hat{\epsilon}_\varphi$. However, we obtain additional information about the quantum state by simultaneously sampling quadrature pairs from the two orthogonal quadrature operators $\hat{\epsilon}_\varphi$ and $\hat{\epsilon}_{\varphi+\frac{\pi}{2}}$. This simultaneous measurement can be realized using an eight-port detector, first introduced by N.G Walker and J. E. Carroll [52, 53]. The recorded quadrature pairs $(X_{\Phi,\mathrm{i}}, X_{\Phi+\frac{\pi}{2},\mathrm{i}})$ can be associated with points in phase space $(q_\mathrm{i}, p_\mathrm{i})$, whereby the two-dimensional frequency distribution of these points then corresponds to the Husimi-Q distribution $Q(q,p)$ of the sampled quantum state [11, p. 361-369]. This interpretation becomes clear when recalling that a point of the Husimi-Q distribution $Q(\alpha_0)$ is proportional to the probability of finding the system in the coherent state $|\alpha_0\rangle$. Using the relation between the phase space variables α and (q,p), we can write the coherent state in the form $|\alpha_0\rangle = |\frac{1}{\sqrt{2}}(|q_0 + ip_0\rangle)$. Consequently, the probability of detecting the system in a specific coherent state is equivalent to the probability of measuring the system in a state with a particular combination of position and momentum. The Husimi-Q distribution considers the uncertainty between $\hat{p}$ and $\hat{q}$ by its increased broadening.

4.2 Experimental Implementation

4.2.1 The Four-Port Detector

The Optical Setup

After introducing the theoretical principles of homodyne detection in the previous section, we now turn to the experimental implementation. We begin with the design of a stable and easily maintainable scheme for the four-port detector. This scheme forms the fundamental building block for all subsequent, more advanced homodyne-detection techniques. In principle, the construction of a four-port detector requires only a beam splitter to superimpose the light fields of signal and local oscillator

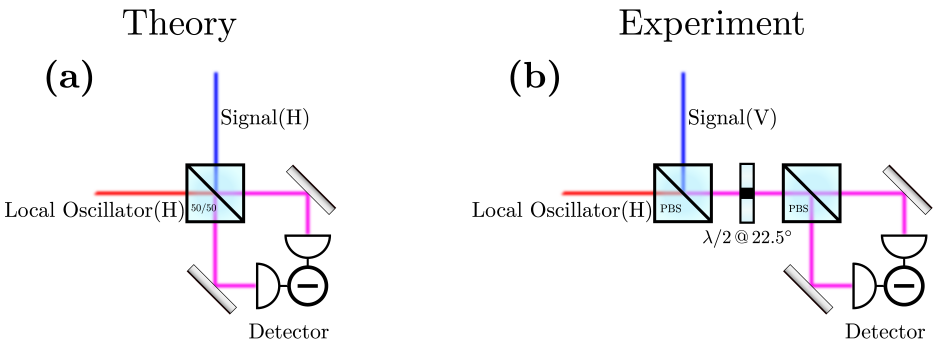

Figure 4.2: Schematic illustrations of the four-port detector design discussed in the theory (a) and used in the experiment (b). The labels 'H' and 'V' indicate horizontal and vertical polarization of the electric field. ($\lambda/2$: half-wave plate; PBS: polarizing beam splitter; 50/50 : non-polarizing 50/50 beam splitter).

and a balanced detector to measure the intensity difference between the two output ports. While this design, illustrated in figure 4.2 (a), is theoretically sufficient, it suffers from a major flaw: It relies on the assumption that the beam splitter provides a perfectly equal splitting ratio, such that the local oscillator intensity is balanced on the detector photodiodes. In practice, however, this condition is rarely fulfilled with sufficient accuracy, leading to a detector imbalance that is difficult to compensate for. To overcome this limitation, we employ a modified four-port detection scheme, shown in figure 4.2 (b). In this configuration, the effective splitting ratio is not determined solely by the intrinsic properties of the beam splitter but can instead be actively controlled via the polarization of the optical fields. The setup begins with a horizontally polarized local oscillator and a vertically polarized signal, whose beams are combined on a polarizing beam splitter (PBS). A half-wave plate then rotates the polarizations of both light fields to the diagonal and antidiagonal axes, so that their horizontal and vertical components have equal amplitudes. A second polarizing beam splitter subsequently mixes the local oscillator and the signal and distributes them according to polarization to the two output ports. Finally, a balanced detector measures the resulting intensity difference between the output ports. This configuration enables a precise detector balancing as the effective splitting ratio of the final beam splitter can be finely tuned by rotating the half-wave plate.

The complete four-port detector setup used in the experiments is shown schematically in figure 4.3. A Mira 900-D femtosecond laser, manufactured by Coherent, serves as the source of the local oscillator. The laser operates at a pulse repetition rate of around 75.39 MHz and emits pulses with an intrinsic pulse duration of about 100 fs. To match the local oscillator spectrally with the signal, the central wavelength of the

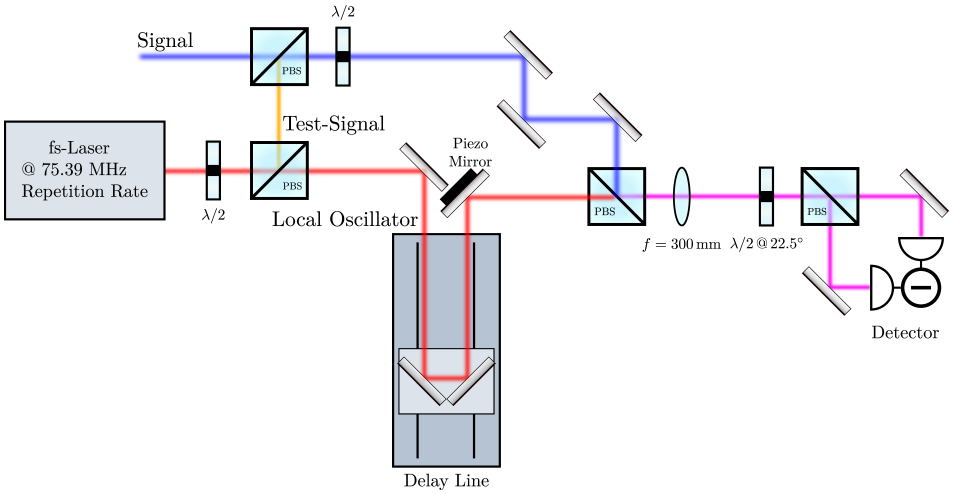

Figure 4.3: Schematic illustration of the complete four-port setup used in the experiments. A femtosecond laser serves as the source for both the local oscillator and the test-signal. The latter is aligned with the signal beam path and used during the alignment procedure. The four-port detection scheme corresponds to the design introduced in figure 4.2 (b). Further details are explained in the text. ($\lambda/2$: half-wave plate; PBS : polarized beam splitter).

laser can be tuned in a range between 700 and 1000 nm. A subsequent placed pulse shaper (not shown in figure 4.3) is used to adapt the spectral width of the laser to that of the signal. After this initial preparations, the local oscillator is directed on a beam splitter, which splits off a small fraction that is afterward coupled into the signal path. This beam, referred to as the test-signal, is used during the alignment to ensure a proper spatial overlap between the signal and the local oscillator at the detector. A delay line is employed to synchronize the arrival times of the local oscillator pulses and the test-signal pulses. Additionally, a piezo-actuated mirror controlled by an E725 piezo controller, constructed by Physik Instrumente, enables continuous modulation of the relative phase between the local oscillator and the signal. The balanced detector is a custom-built high-speed balanced photoreceiver with two integrated Silicon PIN photodiodes that attains a bandwidth of up to 100 MHz and yields an analog voltage signal proportional to the intensity difference between the two photodiodes. An achromatic lens with focal length $f = 300\,\mathrm{mm}$ focuses the optical beams onto the photodiodes.

During the experiments, we employed two configurations to ensure that the test-signal and the actual signal share the same optical path. In the first configuration, we transmit both signals to the detection setup via optical fibers while using a common fiber outcoupler. This method ensures identical spatial beam profiles

and perfectly overlapping beam paths. However, it restricts experiments to light fields with Gaussian intensity distributions and introduces intensity losses when the signal is injected into the fiber. In the second configuration, all light fields are transmitted to the detection setup in free space. While this configuration requires a more complex alignment procedure - since the beam shapes and the spatial overlap must be adjusted manually - it allows the study of arbitrarily shaped beams and typically results in lower optical losses. The configuration employing fiber optics was used for the experiments, discussed in the chapters 6 and 7, whereas a free-space configuration was used for the sixteen-port detector discussed in chapter 8.

The Alignment Procedure

Having introduced the general setup, we next establish a reproducible alignment procedure. At this stage, we assume that the delay line has already been aligned and that the test-signal and the signal share a common optical path. The remaining alignment for the four-port detector consists of two main steps. The first step is to overlap the beam paths of the signal and the local oscillator using the test-signal. To this end, we reduce the power of both beams to around 100 µW and place a charge-coupled device (CCD) in the focal plane of the lens to monitor the spatial overlap. The signal beam path is then aligned iteratively by optimizing the overlap alternately in real space and reciprocal space using the final two steering mirrors in the signal path. Proper alignment is achieved when the beams overlap simultaneously in both spaces. To fine-tune the spatial overlap, we exploit the interference pattern generated by the local oscillator and the test-signal. First, we synchronize the pulses of both beams using the delay line. Subsequently, we use the piezo-actuated mirror to modulate the relative phase between the two beams. We can now use the resulting moving interference pattern to further optimize the overlap. The pattern has the form of horizontally or vertically moving stripes if the beams are misaligned either horizontally or vertically. In contrast, perfect spatial overlap results in a single Gaussian mode with an oscillating intensity. The second step is to balance the local oscillator on the detector. Initially, we adjust the final mirrors in front of the detector to center the focused beam on the photodiodes. The pulse intensity detected on one photodiode can be monitored using the unfiltered detector signal while blocking the other photodiode. The beam is properly centered when the detector signal reaches its maximum value and remains stable under small perturbations. To balance the detector, we again increase the local oscillator power to the level used during measurements. The latter should exceed at least 1 mW to ensure that the detector operates in the shot-noise limited regime. A detailed performance analysis of the detectors employed in this work can be found in [12, p. 39-43]. Finally, we balance the detector by adjusting the final half-wave plate.

Once these steps have been completed, the setup is properly aligned and ready for actual measurements.

4.2.2 The Eight-Port Detector

The Optical Setup

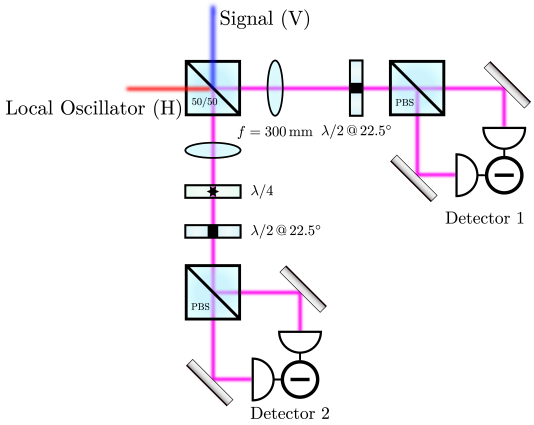

Figure 4.4: Schematic illustration of the eight-port detector setup as used for the experiments. The figure shows only the detector components; the remaining parts of the setup - analogous to those of the four-port detector - are omitted for clarity. The eight-port detector is a combination of two four-port detectors. A single non-polarizing 50/50-beamsplitter overlaps the signal and local-oscillator fields and distributes them equally between the two four-port detectors. An additional quarter-wave plate placed in one detector path introduces a passively stabilized orthogonal phase shift between the detectors, allowing simultaneous sampling of two orthogonal quadrature operators $\hat{\epsilon}_\varphi$ and $\hat{\epsilon}_{\varphi+\frac{\pi}{2}}$. ($\lambda/2$: half-wave plate; $\lambda/4$: quarter-wave plate, 50/50: non-polarizing 50/50 beam splitter; PBS: polarizing beam splitter).

In the next step, we extend the four-port detector setup - which samples one quadrature at a time - to an eight-port detector setup, that enables simultaneous sampling of pairs of orthogonal quadrature operators $\hat{\epsilon}_\varphi$ and $\hat{\epsilon}_{\varphi+\frac{\pi}{2}}$. The basic design of an eight-port detector as used in the experiments is shown schematically in figure 4.4. A non-polarizing 50/50 beam splitter overlaps the light fields of the signal and the local oscillator and distributes them equally to two four-port detectors. To ensure the measurement of orthogonally quadrature pairs, a quarter-wave plate is inserted into one detector path. The slow axis of this quarter-wave plate is aligned parallel to the polarization of the local oscillator, thereby introducing a passively stabilized phase shift of $\frac{\pi}{2}$ between the two four-port detectors.

The Alignment Procedure

The alignment procedure for the eight-port detector is, in principle, identical to that used for the four-port detector. However, it is sufficient to optimize the beam overlap for only one four-port detector, since the overlap at the second detector is automatically ensured by the symmetry of the setup. This property remains valid even if the coupling into the 50/50 beam splitter is misaligned. The correlation between the quadratures measured at the two detectors can be quantified using the Pearson correlation coefficient, which becomes zero for orthogonal quadrature pairs.

4.2.3 Data Acquisition and In-Situ Analysis

Signal Preprocessing

After detection of the light field on the balanced detector, the resulting analog voltage signal is preprocessed and subsequently transferred to an analog-to-digital converter (ADC) card for digitization. The preprocessing stage consists of two steps: In the first step, we suppress correlations originating from local oscillator noise that occurs at the repetition rate and its higher harmonics. For this purpose, two notch filters with center frequencies of 75.4 MHz and 150.8 MHz attenuate noise at the fundamental frequency and the second harmonic. A subsequent low-pass filter with a cut-off frequency of 100 MHz then suppresses the remaining higher harmonics. In the second step, the filtered signal is amplified using an SRS445A preamplifier from Stanford Research Systems. Depending on the configuration, the signal may be amplified once or twice, resulting in overall amplification factors of $\times 5$ or $\times 25$, respectively.

Data Acquisition

Following the preprocessing stage, the signal is transferred to an ADC card of type M4i.2234-x8, manufactured by Spectrum Instrumentation, which enables simultaneous sampling on up to four input channels at a sampling rate of up to 5 GHz and a resolution of 8-bit. In order to reconstruct the pulse positions from the recorded data at a later stage, the data cannot be acquired in the form of a single continuous stream. Instead, the acquisition must be performed segment-wise, where all segments are synchronized such that the pulse positions within the segments are identical. The synchronization of the segments is achieved via an external trigger signal whose definition depends on the measurement type.

To this end, we distinguish between two measurement types that differ by the phase relationship between the local oscillator and the signal. The first type is the phase-averaged measurement, which corresponds to signals whose phase relation to the local oscillator randomizes on timescales smaller than the time between two consecutive pulses. This case represents the more general situation in which the signal and the local oscillator originate from different light sources. In such measurements, the trigger signal is generated by a photodiode that monitors the local-oscillator pulses. This trigger signal is hereafter referred to as the simple-trigger. The second type is the phase-sensitive measurement, which requires a stable phase relation between the signal and the local oscillator. This condition is usually only fulfilled when both light fields originate from the same light source. In this case, the phase is actively modulated using the piezo-actuated mirror to record quadratures at all phases. Since the phase modulation is deterministic, the instantaneous phase can be reconstructed from the recorded data afterward. Ideally, the piezo motion would be linear, leading to a uniform phase distribution. Due to mechanical stability issues, however, the piezo motion is in practice sinusoidal and the phase modulation consequently nonlinear. To obtain a uniform phase distribution in the recorded data, nonetheless, we restrict the quadrature sampling process to time intervals during which the piezo-actuator motion is approximately linear. To achieve this, we combine the simple-trigger with a second trigger signal that depends on the displacement of the piezo mirror, as shown schematically in figure 4.5. The combined trigger signal, generated from the photodiode and the piezo controller, is referred to as the complex-trigger.

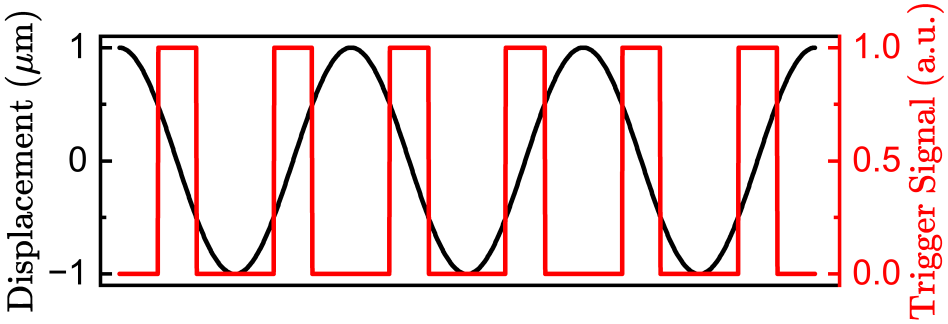

Figure 4.5: Schematic illustration of the piezo trigger signal (red) as a function of the piezo displacement (black).

Finally, the measurement of a quantum state requires two separate homodyne measurements: one measurement of the vacuum state, which is used to determine the amplification factor introduced by the local oscillator and the electronics, and one measurement of the signal state. These measurements are recorded subsequently and stored in separate files. Each homodyne measurement generates three files: a data file, containing the recorded digitized voltages, a file containing the timestamps of the recorded segments, and a configuration file storing the acquisition parameters and software settings. The size of the data file depends on several factors, including the number of active channels, the sampling rate of the ADC card, the measurement type, and the characteristics of the signal under investigation. For a vacuum measurement, data volumes of around $100 - 200\,\mathrm{MiB}$ are typically sufficient, whereas signal measurements may range from several hundred MiB up to several GiB.

In-Situ Analysis Using Homodyne Detection

One of the major challenges in scientific experiments is the time delay between data acquisition and data analysis, slowing down the usually iterative process of identifying optimal experimental parameters. This issue becomes particularly critical when experiments become more complex, often accompanied by larger parameter spaces and longer experimental preparation times. In such situations, it is advantageous to be able to perform preliminary in-situ analyses during the experiment. While such in-situ analysis schemes cannot be implemented for all types of experiments and analyses, it is possible for a wide range of analyses based on quadratures, sampled via homodyne detection. For this reason, we developed a dedicated recording software that not only automates homodyne measurements, but also enables an in-situ analysis of the signal based on smaller datasets consisting of around $1000 - 1000000$ quadratures. The software builds upon the earlier works of J. Thewes [12] and C. Lüders [54], who implemented the predecessor, capable of performing homodyne measurements on up to three four-port detectors. Building on this foundation, we restructured the original code base and extended it to support a wide range of the most common analysis techniques used throughout this work. This includes:

- Computation of the normalized and cleaned quadratures
- Phase-averaged measurements:
  - Computation of $\langle \hat{n} \rangle$ and $g^{(2)}(0)$ with and without time resolution on up to four detection channels
  - Computation and analysis of the Husimi-Q distribution on up to two detection channel pairs.

- Phase-sensitive measurements:
  - Computation and analysis of the density matrix and the Wigner distribution on one detection channel

To keep the software both easy to control and easy to extend, the software architecture is organized as a finite-state machine that separates the codes for preparation, detection, and analysis. The graphical user interface, the communication with devices, and the overall data flow are handled in LabVIEW, while the computationally demanding analysis routines are implemented in MATLAB. To improve computational performance, most analysis algorithms are implemented in a vectorized form and are partially accelerated using a GPU of type RTX 3090, manufactured by Nvidia. The duration of a single analysis cycle depends strongly on the selected analysis routines, the number of active channels, and the size of the recorded dataset. For example, calculating the average $\langle \hat{n} \rangle$ and $g^{(2)}(0)$ on a single channel based on approximately 10000 quadratures requires about 30 ms. In contrast, a density-matrix reconstruction or a complete Husimi-Q analysis may require approximately 1-3 s.

4.3 Data Analysis

In the previous sections, we have introduced the concept of homodyne detection, which enables the sampling of the quadrature operator $\hat{\epsilon}_\varphi$ of a light field. Depending on the measurement type and the experimental configuration, the recorded quadratures enable a wide range of different analysis techniques. An overview of the techniques employed in this work is presented in the flow chart shown in figure 4.6. In the following sections, we briefly discuss most of these methods. The calculation of the Q distribution is excluded from the discussion, as its construction from measured quadratures is straightforward. The implemented analysis procedures are based on the approaches presented in [12][54].

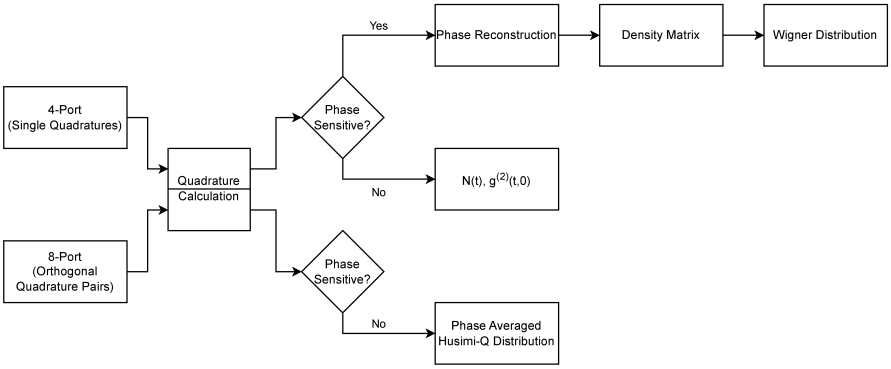

Figure 4.6: Overview of the analysis methods, based on homodyne-detection, that were used in the experiments.

4.3.1 Quadrature Calculation

The basis of all analysis methods employed in this work is the calculation of quadratures from the recorded raw data. This calculation involves several processing steps, which are briefly described in the following.

Integration of the Pulses

The first step of the quadrature calculation is the determination of the unnormalized quadratures from the digitized voltages. To determine the positions of the pulses within the recorded data, we consider several synchronized segments of equal length and calculate the variance of the digitized voltages for a fixed position across all segments. The variance maximizes at the positions corresponding to the pulses. This behavior arises because the overlap between the local oscillator and the signal becomes maximal, which maximizes the amplification of the signal noise and, consequently, the variance across the segments. The visibility of the maxima improves with the number of segments. To ensure a reliable automatic detection of the maxima, we used at least 100 segments to calculate the variance. Since the detector response to a pulse is longer than the time between two consecutive samples of the ADC card, the recorded voltages must be integrated over a time window around the pulse center. Throughout this work, the integration window was set to one-third of the time interval between two consecutive pulses.

Removal of the Offset

The second step of the quadrature calculation is the removal of offsets from the quadrature distribution. Offset correction can be applied when the phase distribution is uniform across the dataset such that the quadrature average must be zero. The type of applicable offset correction depends on the timescales of the averaging process. If the averaging process takes place on long timescales, as in phase-sensitive measurements, one is limited to the removal of a constant offset, calculated from the whole data set. However, if the averaging takes place on short timescales, as in typical phase-averaged measurements, one can also use a stepwise offset that is calculated on and applied to smaller data subsets. The stepwise offset-correction is, in general, more precise, as it also compensates for slow temporal drifts in the offset.

Removal of the Detector Response

The third step of the quadrature calculation is the removal of correlations between consecutive quadratures X_i, $X_{\mathrm{i}+1}$, ..., $X_{\mathrm{i}+m}$. Such correlations arise when the detector response time exceeds the time interval between consecutive pulses, causing the response of one pulse to partially overlap with the response of the subsequent ones. In general, it is not possible to remove these correlations retrospectively, since correlations originating from the detector cannot be distinguished from those arising from the signal itself. However, in the special case of light fields with coherence times that are significantly shorter than the time between two consecutive pulses, one may assume that the pulses are intrinsically uncorrelated. This condition is fulfilled, for example, for the vacuum, thermal light fields, or the emission of a polariton condensate.

A method for eliminating the detector response was introduced by Kumar et al. [55]. The idea is to construct a new set of uncorrelated quadratures from the measured correlated quadratures using a procedure analogous to the Gram-Schmidt orthogonalization algorithm. We begin with a set of N correlated quadratures and construct a set of m vectors $\{\vec{w}_\mathrm{i}\}$ from it, such that consecutively measured quadratures X_i, $X_{\mathrm{i}+1}$, ..., $X_{\mathrm{i}+m}$ are placed at the same position, but in consecutive vectors $\vec{w}_\mathrm{i}$, $\vec{w}_{\mathrm{i}+1}$, ..., $w_{\mathrm{i}+m}$. The parameter m defines up to which subsequent pulse, correlations should be removed. The simplest way to construct these vectors from the measured quadratures is the linear filling scheme depicted in equation (4.13). In this notation, $X[\mathrm{i}]$ denotes the quadrature at index [i] in the data set. The new set of uncorrelated vectors $\{\vec{v}_\mathrm{i}\}$ is then obtained using the Gram-Schmidt

orthogonalization

$$\vec{v}_\mathrm{j} = \vec{w}_\mathrm{j} - \sum_{\mathrm{i}=1}^{j-1} \frac{\langle \vec{v}_\mathrm{i}, \vec{w}_\mathrm{j} \rangle}{\langle \vec{v}_\mathrm{i}, \vec{v}_\mathrm{i} \rangle} \vec{v}_\mathrm{i} \,. \tag{4.12}$$

Finally, the entries of the new vectors $\{\vec{v}_\mathrm{i}\}$ - excluding those of the first vector $\vec{v}_1$ - constitute the decorrelated quadratures. The algorithm remains valid as long as the correlations between different vectors remain small compared to their autocorrelations, that is $\langle \vec{w}_\mathrm{i}, \vec{w}_\mathrm{k} \rangle \ll \langle \vec{w}_\mathrm{i}, \vec{w}_\mathrm{i} \rangle$ for $\mathrm{i} \neq \mathrm{k}$. As $\dim(\vec{w}_\mathrm{i})$ is typically larger than m, the orthogonalization algorithm is incomplete. A side effect of the algorithm is that it reduces the average magnitude of the quadratures. This arises as the Gram-Schmidt orthogonalization returns the part of the vector that is orthogonal to all previous vectors. Consequently, the magnitude of the new vector is smaller than that of the original vector $|\vec{v}_\mathrm{j}| \leq |\vec{w}_\mathrm{j}|$. On average, this effect then also translates to the individual quadratures. Finally, the strength of the observed reduction decreases with the vector dimension. This follows, as the scalar product between two randomly oriented vectors vanishes with increasing vector-space dimension.

The effect becomes problematic when the number of quadratures differs between the vacuum and the signal measurement. In such cases, the algorithm rescales the two datasets differently, resulting in an incorrect normalization of the quadratures. One way to avoid this issue while using datasets of different sizes is to employ high-dimensional vectors with $\dim(\vec{w}_\mathrm{i}) \gg 100000$, such that the difference in rescaling becomes negligible. We can construct these high-dimensional vectors even from smaller datasets using an alternative vector construction method given in equation (4.14), which reuses quadratures. With this approach, we can construct m vectors of dimension $N - m$ from a set of N quadratures. In contrast, the linear construction method yields only m vectors of dimension $\frac{N}{m}$. In the experiments, we used a minimal vector dimension of one million.

$$\left\{ \begin{pmatrix} X[1] \\ X[m+1] \\ X[2m+1] \\ \vdots \\ X\left[\frac{m-1}{m}N+1\right] \end{pmatrix}, \begin{pmatrix} X[2] \\ X[m+2] \\ X[2m+2] \\ \vdots \\ X\left[\frac{m-1}{m}N+2\right] \end{pmatrix}, \ldots, \begin{pmatrix} X\,[m] \\ X\,[3m] \\ X\,[2m] \\ \vdots \\ X\,[N] \end{pmatrix} \right\} \tag{4.13}$$

$$\left\{ \begin{pmatrix} X[1] \\ X[2] \\ X[3] \\ \vdots \\ X[N-m] \end{pmatrix}, \begin{pmatrix} X[2] \\ X[3] \\ X[4] \\ \vdots \\ X[N-m+1] \end{pmatrix}, \ldots, \begin{pmatrix} X[m] \\ X[m+1] \\ X[m+2] \\ \vdots \\ X[N] \end{pmatrix} \right\} \tag{4.14}$$

Normalization of the Quadratures

In the fourth step of the quadrature calculation we use the quadrature distribution obtained from the vacuum measurement to determine a normalization constant $\mathcal{N}$ for the signal measurement that includes the amplification due to the local oscillator and the electronics. To this end, we exploit that the Wigner distribution of the vacuum state $W(q,p)_{\mathrm{Vac}}$ has a characteristic width of $\frac{1}{\sqrt{2}}$. Accordingly, $\mathcal{N}$ is given by

$$\mathcal{N} = \frac{1}{\sqrt{2}\sigma(\{X_{\mathrm{Vac}}\})}\,, \tag{4.15}$$

where $\sigma(\{X_{\mathrm{Vac}}\})$ denotes the width of the unnormalized quadrature distribution obtained from the vacuum measurement.

Data Segmentation Based on the Piezo Motion

The final step of the quadrature calculation is only required for phase-sensitive measurements, where the phase is actively modulated using the piezo-actuated mirror. In this case, the normalized quadratures are segmented according to the piezo motion using the timestamps. This segmentation allows the reconstruction of the initial direction of motion of the piezo mirror, which is necessary for recovering the phase information of the signal.

4.3.2 Analyses Based on Phase-Sensitive Four-Port Measurements

After the quadrature calculation, we next focus on analysis techniques that are based on phase-sensitive measurements.

Reconstruction of the Phase Information

The foundation of all phase-sensitive analysis technqiues is the reconstruction of the phase information. We begin with a data set of quadratures, segmented according to the motion of the piezo mirror. The time series $X(t)$ of the quadratures within a segment typically resembles a curve, as shown in figure 4.7, and corresponds to a sinusoidal curve with a finite width. The modulation of the curve arises from the piezo induced phase modulation, while the finite width originates from the intrinsic quantum noise of the signal state. For phase reconstruction, only the slowly varying, piezo induced phase is of interest. Ideally, one could reconstruct the slowly changing

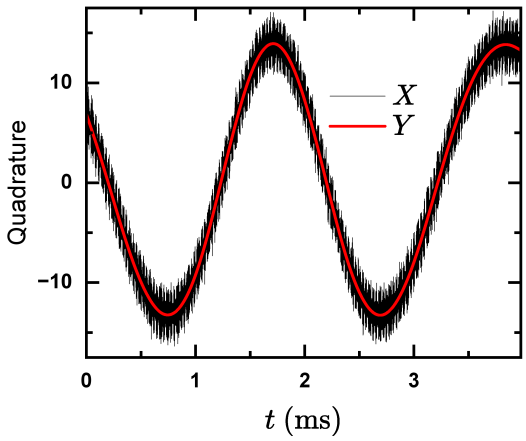

Figure 4.7: Illustration of the time evolution of the raw quadratures $X(t)$ (black) and the corresponding spline interpolation $Y(t)$ (red) over one piezo segment.

phase by applying a sinusoidal fit to $X(t)$. In practice, however, this approach is not robust enough as the modulation is not perfectly sinusoidal. Deviations from ideal sinusoidal behavior may stem from residual nonlinearities in the piezo motion or from external perturbations such as air fluctuations. To determine the phase nonetheless, we employ a more general reconstruction procedure consisting of four steps:

1. We smooth the quadratures time series $X(t)$ using spline interpolation. The resulting curve $Y(t)$ then corresponds to the active phase modulation.

2. We identify the extrema of $Y(t)$ and divide the curve into segments such that each segment $Y_\mathrm{i}(t)$ is either monotonically increasing or monotonically decreasing.

3. We normalize each segment $Y_\mathrm{i}(t)$ to the interval $(-1, 1)$.

4. We calculate the phase in each segment individually using $\Phi(Y_\mathrm{i}(t)) = \arcsin(Y_\mathrm{i}(t))$ for rising segments and $\Phi(Y_\mathrm{i}(t)) = \pi - \arcsin((Y_\mathrm{i}(t)))$ for falling segments.

This procedure still assumes a sinusoidal modulation but allows for a nonlinearly evolving phase. In practice, the implementation used for the data analysis is more sophisticated than the simplified description given above, as it also accounts for several special cases that may occur in the experimental data.

Reconstruction of the Density Matrix

After reconstructing the phase information, we can use the set of quadrature-phase pairs $\{(X_\mathrm{i}, \Phi_\mathrm{i})\}$ to reconstruct the quantum state of the light field. The objective is to determine the density operator $\hat{\rho}_0$ that maximizes the likelihood to reproduce the measured data set. This likelihood is described by the likelihood function

$$\mathcal{L}_{X,\Phi}(\hat{\rho}) = \prod_\mathrm{i} \mathrm{Prob}_{X_\mathrm{i},\Phi_\mathrm{i}}(\hat{\rho})\,, \tag{4.16}$$

where $\mathrm{Prob}_{X_\mathrm{i},\Phi_\mathrm{i}}(\hat{\rho})$ denotes the probability to measure $\hat{\rho}$ in the quadrature operator eigenstate $|X_\mathrm{i}, \Phi_\mathrm{i}\rangle$. This Probability is given by

$$\mathrm{Prob}_{X_\mathrm{i},\Phi_\mathrm{i}}(\hat{\rho}) = \langle X_\mathrm{i}, \Phi_\mathrm{i}|\hat{\rho}|X_\mathrm{i}, \Phi_\mathrm{i}\rangle = \mathrm{tr}(|X_\mathrm{i}, \Phi_\mathrm{i}\rangle\langle X_\mathrm{i}, \Phi_\mathrm{i}|\hat{\rho})\,, \tag{4.17}$$

where $|X_\mathrm{i}, \Phi_\mathrm{i}\rangle\langle X_\mathrm{i}, \Phi_\mathrm{i}|$ is the projection operator of the quadrature eigenstate. Based on the likelihood function, we employ the following iterative algorithm originally proposed by A. I. Lvovsky [56], to determine $\hat{\rho}_0$ starting from an arbitrary initial density operator. Each iteration consists of two steps. In the first step, we construct the transition operator $\hat{R}(\hat{\rho})$, defined by

$$\hat{R}\,(\hat{\rho}) = \sum_\mathrm{i} \frac{|X_\mathrm{i}, \Phi_\mathrm{i}\rangle\langle X_\mathrm{i}, \Phi_\mathrm{i}|}{\mathrm{Prob}_{X_\mathrm{i},\Phi_\mathrm{i}}(\hat{\rho})}\,. \tag{4.18}$$

In the second step, we use the transition operator to generate the next iteration of the density operator $\hat{\rho}^{(n+1)}$ according to the recurrence relation

$$\hat{\rho}^{(\mathrm{n}+1)} = \mathcal{N}\hat{R}(\hat{\rho}^{(\mathrm{n})})\hat{\rho}^{(\mathrm{n})}\hat{R}(\hat{\rho}^{(\mathrm{n})})\,, \tag{4.19}$$

where $\mathcal{N}$ is a normalization constant that ensures $\mathrm{tr}(\hat{\rho}^{(\mathrm{n}+1)}) = 1$. The described algorithm represents a special case of the classical expectation-maximization algorithm [57], which guarantees that $\hat{\rho}^{(n)}$ converges to $\hat{\rho}_0$. Overfitting is avoided, as the recurrence relation converges to $\hat{R}(\hat{\rho}_0)\hat{\rho}_0\hat{R}(\hat{\rho}_0) \propto \hat{\rho}_0$.

Up to this point, the entire description has been based on abstract density operators. To obtain the density matrix in the Fock representation, all operators must be represented in the Fock basis. Central element in this operation is the Fock representation of the quadrature operator eigenstates $|X, \Phi\rangle$. Using the commutation

convention $[\hat{q}, \hat{p}] = i$, the representation is derived by

$$\begin{aligned} |X, \Phi\rangle &= \sum_{n=0}^{\infty} \langle n|X, \Phi\rangle |n\rangle \\ &= \sum_{n=0}^{\infty} \mathrm{e}^{in\Phi} \langle n|X, 0\rangle |n\rangle \\ &= \sum_{n=0}^{\infty} \mathrm{e}^{\mathrm{i}n\Phi} \pi^{\frac{1}{4}} \mathrm{e}^{-\frac{1}{2}X^2} \frac{1}{\sqrt{2^n n!}} H_n(X) |n\rangle \,. \end{aligned} \tag{4.20}$$

In the first step, we exploit that the quadrature operator eigenstate $|X, \Phi\rangle$ corresponds to a position operator eigenstate $|X, 0\rangle$ that is rotated in phase space by the angle Φ. The Fock representation then follows, by inserting the well-known overlap of the position and photon number operator eigenstates $\langle n|X\rangle$. The calculation of these overlaps involves Hermite polynomials, which become numerically unstable for large values of n. A numerically more stable approach to compute $F_n = \langle n|X\rangle$ is to use the recurrence relation [58]

$$\begin{aligned} F_0(X) &= \pi^{-\frac{1}{4}} \mathrm{e}^{-\frac{X^2}{2}} \\ F_1(X) &= \sqrt{2} X F_0(X) \\ F_{n>1}(X) &= \sqrt{\frac{2}{n}} X F_{n-1}(X) - \sqrt{\frac{n-1}{n}} F_{n-2}(X) \,. \end{aligned} \tag{4.21}$$

Despite its conceptual simplicity, the density-matrix reconstruction algorithm is computationally demanding, which limits its use in real-time applications. For this reason, we implemented an optimized, vectorized version of the algorithm using matrix operations that can run parallelized on a GPU. Assuming a dataset of N quadrature-phase pairs and a truncated Hilbert space of dimension $n_{\max} + 1$, we first construct the projection matrix $\boldsymbol{M}$, whose elements are defined as $M_{\mathrm{i,j}} = \langle n_{\mathrm{i}}|X_{\mathrm{j}}, \Phi_{\mathrm{j}}\rangle$. The iterative reconstruction algorithm of the density matrix $\boldsymbol{\rho}$ is then given by

$$\begin{aligned} \boldsymbol{P} &= N \boldsymbol{J}_{n_{\max}+1} \cdot \left[\left(\boldsymbol{\rho}^{(n)\top} \cdot \boldsymbol{M}^* \right) \odot \boldsymbol{M} \right] \\ \boldsymbol{R} &= (\boldsymbol{M} \oslash \boldsymbol{P}) \cdot \boldsymbol{M}^\dagger \\ \tilde{\boldsymbol{\rho}}^{(n+1)} &= \boldsymbol{R} \cdot \boldsymbol{\rho}^{(n)} \cdot \boldsymbol{R} \\ \boldsymbol{\rho}^{(n+1)} &= \frac{\tilde{\boldsymbol{\rho}}^{(n+1)}}{\mathrm{tr}\left(\tilde{\boldsymbol{\rho}}^{(n+1)} \right)} \,, \end{aligned} \tag{4.22}$$

where the matrices $\boldsymbol{P}$ and $\boldsymbol{R}$ serve as auxiliary matrices, with $\boldsymbol{R}$ being the matrix representation of the transition operator $\hat{R}$. Further, the matrix $\boldsymbol{J}_{n_{\max}+1}$ denotes

a matrix of dimension $n_{\max}+1$ with all entries equal to one. The matrix operations involve standard matrix multiplication $\cdot$, the Hadamard product $\odot$, and the Hadamard division $\oslash$.

Reconstruction of the Wigner Distribution

Based on the density matrix, we next calculate the Wigner distribution as introduced in (2.31). To evaluate the Wigner distribution more efficiently, we insert the completeness relation of the Fock basis into the Weyl transformation [12]

$$\begin{aligned} W(q,p) &= \mathcal{FT}\left[\langle q+\frac{1}{2}\zeta|\hat{\rho}|q-\frac{1}{2}\zeta\rangle\right] \\ &= \sum_{m,n}\rho_{m,n}\underbrace{\frac{1}{2\pi}\mathcal{FT}\left[\langle q+\frac{1}{2}\zeta|m\rangle\langle n|q-\frac{1}{2}\zeta\rangle\right]}_{F_{m,n}(q,p)} \\ &= \sum_{m,n}\rho_{m,n}F_{m,n}(q,p)\,. \end{aligned} \tag{4.23}$$

This procedure allows us to separate the calculations that depend on the phase space variables from those that depend on the density operator. Consequently, the Wigner distribution is a sum of density-matrix independent functions $F_{m,n}(q,p)$, which are weighted by the corresponding density matrix elements $\rho_{m,n}$. To reduce the memory consumption, we further exploit the hermiticity of the density matrix, leading to the final expression

$$W(q,p) = \sum_{n}\rho_{m,m}F_{m,m}(q,p) + 2\sum_{n>m}\mathrm{Re}(\rho_{m,n})F_{m,n}(q,p)\,. \tag{4.24}$$

4.3.3 Analyses Based on Phase-Averaged Four-Port Measurements

In the previous section, we discussed analysis techniques that rely on phase-sensitive measurements. In most practical situations, however, a stable phase relation between the local oscillator and the signal is not available. This may occur either because the signal and local oscillator originate from different light sources or because the phase relation is lost in the experiment. Nevertheless, we can still access information that depend solely on the photon statistics. In the following subsections, we briefly derive how we can obtain the average photon number $\langle\hat{n}\rangle$ and the equal-time second-order correlation function $g^{(2)}(0)$ from a set of phase-averaged quadratures $\{X_{\mathrm{i}}\}$. We also discuss how this approach can be extended to time-resolved analysis.

Computation of the Average Photon Number

We begin the derivation by reconsidering the quadrature operator $\hat{\epsilon}_\varphi = \frac{1}{\sqrt{2}}\left(\hat{a}\mathrm{e}^{-i\varphi} + \hat{a}^\dagger \mathrm{e}^{i\varphi}\right)$ that contains both annihilation and creation operators. Consequently, higher powers of this operator include product terms of $\hat{a}$ and $\hat{a}^\dagger$. This finding will be the foundation for the following calculations [59]. For the calculation of $\langle\hat{n}\rangle = \langle\hat{a}^\dagger\hat{a}\rangle$, we begin with the calculation of the phase-averaged second moment of the quadrature operator $\langle\hat{\epsilon}_\varphi^2\rangle_\varphi$, which is given by

$$\langle\hat{\epsilon}_\varphi^2\rangle_\varphi = \frac{1}{2}\langle\hat{a}^\dagger\hat{a} + \hat{a}\hat{a}^\dagger + \mathrm{e}^{i2\varphi}\hat{a}^\dagger + \mathrm{e}^{-i2\varphi}\hat{a}\rangle_\varphi\,. \tag{4.25}$$

Assuming that φ is uniformly distributed, all terms proportional to $\mathrm{e}^{in\varphi}$ vanish under the phase average. The remaining terms then simplify to

$$\langle\hat{\epsilon}_\varphi^2\rangle_\varphi = \frac{1}{2}\langle\hat{a}^\dagger\hat{a} + \hat{a}\hat{a}^\dagger\rangle = \langle\hat{a}^\dagger\hat{a}\rangle + \frac{1}{2}\,. \tag{4.26}$$

Consequently, the mean photon number is given by

$$\langle\hat{n}\rangle = \langle\hat{a}^\dagger\hat{a}\rangle = \langle\hat{\epsilon}_\varphi^2\rangle_\varphi - \frac{1}{2}\,. \tag{4.27}$$

Computation of the Equal-Time Second-Order Correlation Function

A similar approach can be used to derive an expression for $g^{(2)}(0)$. In this case, we have to evaluate the phase-averaged fourth moment $\langle\hat{\epsilon}_\varphi^4\rangle_\varphi$ in order to obtain an expression for $\langle\hat{a}^\dagger\hat{a}^\dagger\hat{a}\hat{a}\rangle$. Expanding $\langle\hat{\epsilon}_\varphi^4\rangle$ in terms of annihilation and creation operators yields

$$\begin{aligned}\langle\hat{\epsilon}_\varphi^4\rangle_\varphi = \frac{1}{4}\langle&\hat{a}^\dagger\hat{a}^\dagger\hat{a}\hat{a} + \hat{a}^\dagger\hat{a}\hat{a}^\dagger\hat{a} + \hat{a}^\dagger\hat{a}\hat{a}\hat{a}^\dagger + \hat{a}\hat{a}^\dagger\hat{a}^\dagger\hat{a} + \hat{a}\hat{a}^\dagger\hat{a}\hat{a}^\dagger + \hat{a}\hat{a}\hat{a}^\dagger\hat{a}^\dagger\rangle_\varphi \\ &+\frac{1}{4}\langle\mathcal{O}(\mathrm{e}^{\pm i2\varphi}) + \mathcal{O}(\mathrm{e}^{\pm i4\varphi})\rangle_\varphi\,.\end{aligned} \tag{4.28}$$

Applying the same phase-averaging procedure as before again eliminates all terms proportional to $\mathrm{e}^{in\varphi}$. The remaining contributions yield

$$\langle\hat{\epsilon}_\varphi^4\rangle_\varphi = \frac{3}{2}\langle\hat{a}^\dagger\hat{a}^\dagger\hat{a}\hat{a}\rangle + 3\langle\hat{a}^\dagger\hat{a}\rangle + \frac{3}{4}\,. \tag{4.29}$$

Finally, we obtain the expression

$$g^{(2)}(0) = \frac{\langle\hat{a}^\dagger\hat{a}^\dagger\hat{a}\hat{a}\rangle}{\langle\hat{a}^\dagger\hat{a}\rangle^2} = \frac{\frac{2}{3}\langle\hat{\epsilon}_\varphi^4\rangle_\varphi - 2\langle\hat{\epsilon}_\varphi^2\rangle_\varphi + \frac{1}{2}}{\left(\langle\hat{\epsilon}_\varphi^2\rangle_\varphi - \frac{1}{2}\right)^2}\,. \tag{4.30}$$

Time-Dependent Analysis

When we implement the theoretical considerations discussed above in experiments, expectation values are replaced by ensemble averages. Assuming a sufficiently high sampling rate, this approach enables us to determine both quantities $\langle\hat{n}\rangle(t)$ and $g^{(2)}(t,0)$, dependent on t. For this purpose, we first divide the recorded dataset into smaller subsets, corresponding to recording intervals $[t_\mathrm{i} - \frac{\delta t}{2}, t_\mathrm{i} + \frac{\delta t}{2}]$, and associate them with their central times t_i. Afterward, we calculate $\langle\hat{n}\rangle$ and $g^{(2)}(0)$ on each subset individually. Using a homodyne setup as described in section 4.2.1, this procedure enables us to study the fluctuations in a light field with a time resolution down to 10 µs [60]. A side effect of the time-resolved analysis is that $g^{(2)}(t,0)$ decreases with decreasing δt. This originates from the third term in the equation of $g^{(2)}(t,0)$, see equation(2.45), which increases with the photon-number variance. Considering the calculation of the variance on finite time intervals, the variance only includes photon-number fluctuations that occur on timescales comparable to or shorter than δt. Consequently, fluctuations acting on longer timescales - such as those caused by external mechanical noise - do not contribute to $g^{(2)}(t,0)$. We can exploit this effect to distinguish between high-frequency noise originating from the light source and low-frequency noise created by external mechanical instabilities [61].

5 Experimental Methods - Excitation and Spectroscopic Analysis of Exciton-Polaritons in a Microcavity

This chapter introduces the experimental setup used to excite a polariton condensate inside an optical annular trap and to study the emitted light field spectroscopically and via homodyne detection. The corresponding experimental results are presented and discussed in chapter 7.

5.1 The Sample

The sample used in the experiments is a high-quality $3\lambda/2$ microcavity consisting of two DBR mirrors. The front and back mirrors consist of 32 and 40 alternating $AlAs/Al_{0.2}Ga_{0.8}As$ layers, respectively. Twelve $GaAs$ quantum wells with a thickness of 7 nm are arranged in groups of four at the three antinodes of the cavity field. The polariton lifetime at $\Delta_{\text{c-x}}(0) = 0$ is approximately 200 ps [62] and the Rabi splitting is about 10 meV. All measurements reported in this work were performed at $\Delta_{\text{c-x}}(0) = 0$.

5.2 Experimental Spectroscopy Setup

To excite the sample non-resonantly and to collect its emission, we used the experimental setup schematically depicted in figure 5.1. A SolsTiS 2000 PSX-F continuous-wave laser, manufactured by M-Squared, was used to excite the sample non-resonantly through the first upper Bragg minimum at an energy of 1.746 eV. The excitation power was adjusted using a combination of a motorized half-wave plate and a Glan-Thompson prism, while the intensity profile of the excitation beam was reshaped into an annular distribution using a spatial light modulator (SLM) with an imprinted axicon phase profile. The sample, mounted in a cold-finger flow cryostat and cooled down to approximately 10 K, was excited in reflection geometry. A 20x microscope objective with a numerical aperture of 0.26 and a focal length of $f_{\text{MO}} = 10$ mm focused the excitation beam to a ring with a diameter of 9.6 µm and

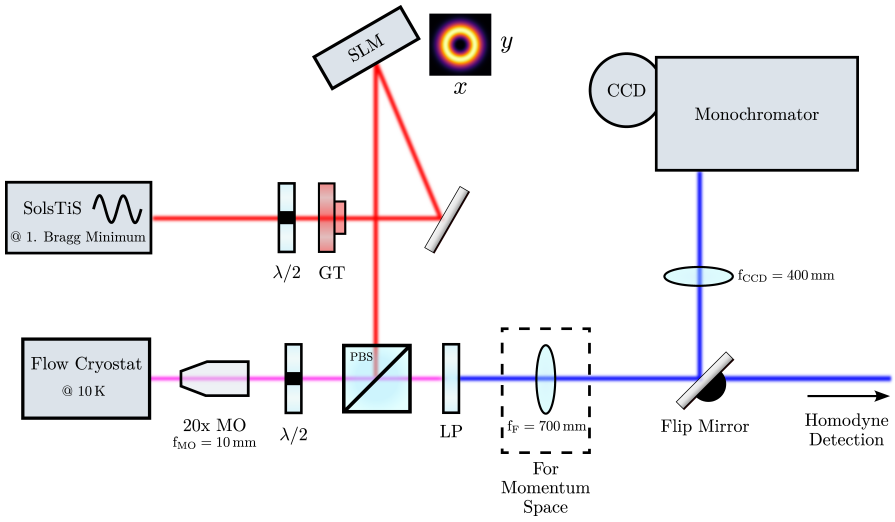

Figure 5.1: Schematic illustration of the spectroscopy setup used for the experiments discussed in chapter 7. A continuous-wave laser with an annular intensity profile excites the sample non-resonantly in reflection geometry. The photoluminescence of the sample is analyzed either by conventional spectroscopy in real and momentum space or by homodyne detection. Further details are provided in the text. ($\lambda/2$: half-wave plate; GT: Glan-Thompson prism; PBS: polarizing beam splitter; LP: long-pass filter; MO: microscope objective; SLM: spatial light modulator). Adapted from [63].

simultaneously collected the emitted light. After collection, the photoluminescence was polarization filtered to select the component parallel to the cavity's principal axis. At high excitation powers, this polarization corresponds to the polarization of the polariton condensate. Subsequently, two long-pass filters with an edge energy of 1.653 eV were used to remove residuals of the excitation laser from the signal beam.

The emission was analyzed with conventional spectroscopy and with homodyne detection. For the former, a lens with $f_{\mathrm{CCD}} = 400\,\mathrm{mm}$ focused the emission onto the slit of a spectrometer connected to a CCD to analyze the spatial distribution and the dispersion relation. The spectrometer had three blazed gratings with 300, 1200, or 1800 lines per millimeter, the CCD had a pixel size of 20 µm. To perform measurements in momentum space, a second lens of $f_{\mathrm{F}} = 700\,\mathrm{mm}$ was placed in the beam path. Alternatively, the emission was directed to an eight-port detector, as introduced in section 4.2.2, to study the coherence properties of the emission. Below the condensation threshold, the average number of signal photons overlapping with a single local-oscillator pulse was nearly zero, since the emission intensity of the uncondensed state was too weak. For this reason, we focused exclusively on the

characterization of the condensed state and tuned the energy of the local oscillator to match with the energy of the condensate mode, while avoiding spectral overlap with the emission of the uncondensed polaritons.

6 Quantum Resource Theory of Lasers

In section 2.2.2, we introduced a set of density-matrix-based quantifiers, consisting of the quantum coherence $\mathcal{C}$, the mixedness $\mathcal{M}$, and the purity of the dephased state $\mathcal{P}_{\text{Inc}}$ to characterize coherence phenomena in a system beyond the conventional $g^{(2)}$. In this chapter, we go one step further and consider the role of quantum coherence within the broader framework of quantum resource theories. A quantum resource theory (QRT) formalizes the set of quantum informational processes that can be realized under a restricted set of physically allowed operations. These allowed operations are referred to as free operations, while the corresponding accessible states are regarded as free states. Conversely, states that cannot be generated by free operations are regarded as resources [1]. A prominent example of a quantum resource theory is the resource theory of entanglement in the context of quantum communication between two separated parties [64], where entangled states emerge as resources due to both parties being restricted to local quantum operations and classical communication channels (LOCC). Based on the distinction between resources and free states, a quantum resource theory classifies a quantum state according to its usefulness in accomplishing a specific quantum informational task [1]. This includes fields such as quantum communication, quantum computation, or quantum random number generation. Quantum resource theories are often formulated from a point of view that emphasizes non-classicality, leading to the assumption that only non-classical states are considered resourceful, whereas classical states are treated as free. However, this one-to-one correspondence between non-classicality and resourcefulness does not necessarily hold for the use of light fields in real tasks arising in applied quantum technologies. On the contrary, numerous experiments, performed over the decades, have demonstrated that classical light fields indeed play an essential role in various quantum information processes. For instance, fluctuations of the vacuum state [65, 66] and thermal states [5, 6] have been employed as sources for quantum random number generators. Similarly, classical coherent light has already become the standard choice for coherent qubit control [2, 3, 4], while low-intense coherent light pulses are used instead of single-photons to enable faster quantum key distribution [67]. It has even been shown that certain types of quantum computations can be accelerated by the use of optically classical light field states [68, 69]. Consequently, there exists a discrepancy between the value of classical light fields in the established quantum resource theories and their value in a wide range of experimental applications.

We address part of this gap by introducing a new quantum resource-theoretical model for masers and lasers, which treats coherent states as resourceful and incoherent states as free. The model is built upon the framework of the quantum resource theory of quantum coherence, which quantifies the amount of quantum superpositions of a quantum state represented in a designated basis. It is important to note that quantum coherence therefore, is a basis-dependent concept, so that some bases are considered more classical than others. In finite-dimensional systems such as qubits, the resourcefulness of a state carrying quantum coherence in a reasonable basis is intuively evident, as it indicates non-classicality. This intuition is confirmed as the purity of the state limits the amount of quantum coherence one can obtain via unitary transformations [70], and the quantum coherence may be converted into quantum discord or quantum entanglement [71, 72]. The relation between non-classicality and quantum coherence, however, becomes less evident when considering light fields that are defined on infinite-dimensional Hilbert spaces. One of the problems, for example, is the lack of a well-defined maximal-mixed state. This discrepancy, however, poses no significant problem as we have already seen that non-classicality is no prerequisite for the usefulness of light fields in quantum information tasks. In our analysis, we focus on partially coherent light sources containing thermal noise that are described by the model of displaced thermal states. While such an analysis may seem unnecessary for high-end laboratory equipment, it becomes crucial when considering miniaturized coherent light sources that are embedded in compact quantum devices. Although laser technology has advanced tremendously since the first laser was built in 1960 [73], optimizing laser performance remains a relevant challenge [74, 75], and one must balance priorities between optimal intensity, optimal coherence, low cost, and device compactness. In this context, it becomes essential to determine how far a laser system can deviate from an ideal coherent light source without losing its functionality for the demanded task. To quantify the quantum coherence, we measure the distance between a given state $\hat{\rho}$ and its closest incoherent counterpart $\hat{\rho}_{\mathrm{Inc}}$ using the squared Hilbert-Schmidt norm as a distance measure. This approach guarantees a finite measure of quantum coherence upper-bounded by both the mixedness of the state and the purity of the closest incoherent state. Nevertheless, it cannot be applied universally to all kinds of states and operations, as certain cases may violate the monotonicity condition of the quantifier [27]. Considering these limitations, we restrict ourselves to classical Gaussian states that can be modeled as a displaced thermal state and limit the set of allowed operations to basic operations. These operations include the propagation through vacuum or simple media and the interaction with a qubit. Under these constraints, our quantifier remains a valid measure of coherence [76, 77].

The remainder of the chapter bases on the published paper 'Quantum resource theory of lasers' [78] and is organized in four sections. We begin by establishing a resource-theoretical model of lasers and masers in section 6.1, where we discuss the properties of the light field emitted by a laser in the different phases of the onset of lasing. In the second section 6.2, we verify our model experimentally. By superimposing coherent and thermal light fields, we generate displaced thermal states of tailored compositions. A quantum state tomography setup then enables us to compare the predictions of the model with experimental results obtained directly from reconstructed density matrices. Following these two more general sections, we focus our analysis on a specific quantum information task and examine the role of quantum coherence in preparing high-quality qubit superposition states. We begin this part of the study qualitatively in section 6.3, where we consider three different excitation scenarios, identify emerging decoherence mechanisms, and define meaningful reference frames for each case. Finally, in section 6.4, we complete our analysis by quantitatively investigating the qubit initialization in these scenarios via numerical simulations.

6.1 A Resource-Theoretical Model for Real Lasers

We start our considerations by constructing a resource-theoretical model that describes the start-up process of real lasers and masers in four phases. Although these phases are not sharply separated in practice, they serve as a conceptual guide to understand how the resource-theoretical properties of the emitted light field change during laser startup. For each phase, we quantify the coherence properties of the corresponding quantum state by the set of quantum coherence $\mathcal{C}$, mixedness $\mathcal{M}$, and purity of the closest incoherent state $\mathcal{P}_{\mathrm{Inc}}$. Representative density matrices and Wigner distributions of the light field in each phase are illustrated in figure 6.1. We begin with the situation before any light is present (phase (I)). In this phase, the emission corresponds to a vacuum state described by the density operator $\hat{\rho}_{\mathrm{vac}}$. As the vacuum state is pure but diagonal, we find $\mathcal{P}(\hat{\rho}_{\mathrm{vac}}) = \mathcal{P}_{\mathrm{Inc}}(\hat{\rho}_{\mathrm{vac}}) = 1$ and consequently $\mathcal{M}(\hat{\rho}_{\mathrm{vac}}) = 0$ and $\mathcal{C}(\hat{\rho}_{\mathrm{vac}}) = 0$. Next, we consider the moment immediately after the initial spontaneous emission into the lasing mode, when the active medium has not reached population inversion and the emitted light field, yet, originating from spontaneous emission, is thermal (phase (II)). The thermal state is incoherent and mixed, such that $\hat{\rho}_{\mathrm{th}} = \hat{\rho}_{\mathrm{th,Inc}}$, and in turn $\mathcal{P}(\hat{\rho}_{\mathrm{th}}) = \mathcal{P}_{\mathrm{Inc}}(\hat{\rho}_{\mathrm{th}})$. Consequently, $\hat{\rho}_{\mathrm{th}}$ possesses no quantum coherence. The purity of a thermal state of average photon number n_{th} is given by [77]

$$\mathcal{P}(\hat{\rho}_{\mathrm{th}}) = \frac{1}{2n_{\mathrm{th}} + 1}\,, \tag{6.1}$$

such that the mixedness is

$$\mathcal{M}(\hat{\rho}_{\mathrm{th}}) = 1 - \mathcal{P}(\hat{\rho}_{\mathrm{th}}) = \frac{2n_{\mathrm{th}}}{2n_{\mathrm{th}}+1}\,. \tag{6.2}$$

Accordingly, thermal states of large mean photon number are more mixed than thermal states of low average photon number. After some time, the active medium reaches population inversion, and the system crosses the lasing threshold. From this point onward, stimulated emission dominates the emission process, leading to predominantly coherent emission. In our model, we assume - in a simplified description - that stimulated emission occurs in addition to spontaneous emission (phase (III)). Mathematically, the transition is then described by applying the displacement operator $\hat{D}(\alpha)$ on $\hat{\rho}_{\mathrm{th}}$, yielding the displaced thermal state $\hat{\rho}_{\mathrm{DT}}$. The mixedness $\mathcal{M}$, however, remains invariant under this transformation as the displacement operator is unitary. This leads to our first central observation: the mixedness of the light field emitted by a laser depends solely on the absolute number of residual thermal photons and is independent of the number of coherent photons. Moreover, the number of thermal photons not only determines the mixedness of the light field but also constrains the maximal achievable quantum coherence. In particular, even a single thermal photon reduces the maximal possible quantum coherence to 0.5. In addition to the state's mixedness, we further calculate the purity of the closest incoherent state $\mathcal{P}_{\mathrm{Inc}}$ of the light field [77]

$$\mathcal{P}_{\mathrm{Inc}}(\hat{\rho}_{\mathrm{DT}}) = \frac{\exp\left[-2|\alpha|^2/(2n_{\mathrm{th}}+1)\right]}{2n_{\mathrm{th}}+1} I_0\left[\frac{2|\alpha|^2}{2n_{\mathrm{th}}+1}\right]\,, \tag{6.3}$$

where $I_0(x) = \frac{1}{2\pi}\int_0^{2\pi} \mathrm{d}\varphi\, \mathrm{e}^{x\cos(\varphi)}$ denotes the zeroth modified Bessel function of the first kind. With this expression, we then obtain the quantum coherence of the displaced thermal state

$$\mathcal{C}(\hat{\rho}_{\mathrm{DT}}) = \frac{1 - \exp\left[-2|\alpha|^2/(2n_{\mathrm{th}}+1)\right] I_0\left[2|\alpha|^2/(2n_{\mathrm{th}}+1)\right]}{2n_{\mathrm{th}}+1}\,. \tag{6.4}$$

Finally, we consider dephasing effects, for instance caused by turbulent air fluctuations along the beam path or mechanical fluctuations of the used optical components. To keep the model simple, we assume that the dephasing channels predominantly act on the phase information and neglect alterations of the photon statistics. In the most extreme scenario, all phase information vanishes, and one ends up with a completely incoherent state $\hat{\rho}_{\mathrm{DT,Inc}}$ which retains the photon statistics but lacks all off-diagonal matrix elements (phase (IV)). In this scenario, we note that all quantum coherence is converted into additional mixedness while $\mathcal{P}_{\mathrm{Inc}}$ remains constant.

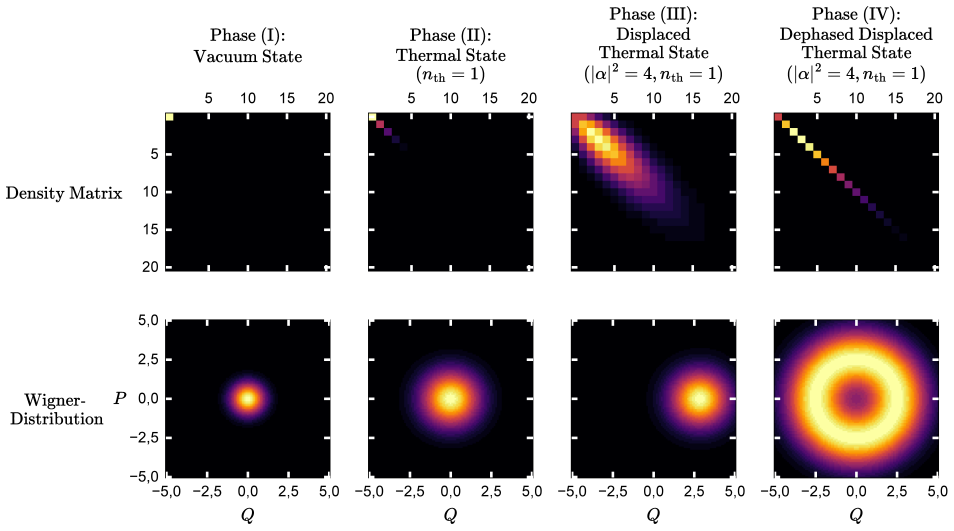

Figure 6.1: Density matrices and Wigner distributions of the four phases (I)-(IV), discussed in the resource-theoretical model.

6.2 Experimental Validation of the Displaced Thermal State Model

After introducing the resource-theoretical model for real lasers and masers, we proceed to experimentally verify the model. To this end, we consider that the phases (I)-(III) can be effectively described within the displaced thermal state model. Consequently, it is sufficient to validate its predictions for the coherence by comparing the theoretical curves for $\mathcal{C}$, $\mathcal{M}$, and $\mathcal{P}_{\mathrm{Inc}}$ with corresponding experimental values obtained directly from reconstructed density matrices. To this end, we combine coherent and thermal light fields on a beam splitter to generate artificial displaced thermal light fields with controllable coherent and thermal photon numbers and study the created quantum states with quantum state tomography. Phase (IV) is excluded from the experimental analysis, as we obtain the density matrix of the dephased state from the density matrix of the reconstructed full state by removing all off-diagonal density matrix elements.

6.2.1 Experimental Setup and Data Processing

Quantum state tomography was performed using the four-port detector setup introduced in section 4.2.1. The test-signal derived from the same laser source as the local oscillator served as the coherent component of the signal, thereby maintaining a stable phase relation to the local oscillator. The thermal component of the signal was provided by a continuous wave superluminescent diode (SLD). Both light fields were centered to a wavelength of 830 nm. The laser pulses were reshaped to a rectangular spectral pulse profile with a spectral full-width at half-maximum (FWHM) of approximately 10 nm corresponding to a pulse duration of about 200 fs, whereas the emission of the SLD was spectrally broader. This broader spectrum, however, did not affect the analysis, as only the spectral component overlapping with the local oscillator contributed to the recorded quadratures. The coherent and thermal signal components were superimposed on a non-polarizing fiber beam splitter. Their relative contributions, as well as the overall intensity, were adjusted by combinations of half-wave plates and Glan-Thompson polarizers. To monitor the composition of the light field during the state preparation, the light field was characterized in situ via optical homodyne tomography. Further, each state was recorded multiple times to compensate for photon-number fluctuations between successive measurements. During data analysis, we determined the values of $\mathcal{C}$, $\mathcal{M}$, and $\mathcal{P}_{\mathrm{Inc}}$ using two different approaches. Experimental data points were directly calculated from the reconstructed density matrices using the definitions introduced in section 2.2.2. In parallel, theoretical curves predicted by the displaced thermal state model were computed from the coherent and thermal photon numbers $|\alpha_0|^2$ and n_{th} using the equations (6.2)-(6.4) introduced in the previous section. Both photon numbers were extracted from the Wigner distributions of the states calculated from the density matrices using the algorithm introduced in section 4.3.2. For extraction, we used the Wigner distribution of the displaced thermal state [77]

$$W(\alpha) = \frac{2}{\pi(2n_{\mathrm{th}}+1)} \exp\left[-2\frac{|\alpha-\alpha_0|^2}{2n_{\mathrm{th}}+1}\right] \tag{6.5}$$

where α_0 denotes the displacement of the state in phase space.

6.2.2 Validation of the Model

To validate the displaced thermal state model, we consider two scenarios. In the first scenario, we follow the laser model and analyze the transition from phase (II) to phase (III). To this end, we begin with a fixed number of thermal photons and gradually increase the number of coherent photons. As photon number fluctuations were negligible, all iterations of a measurement point were taken into account.

Further, the mean thermal photon number used for model curves was averaged from the whole measurement. The results are presented in figure 6.2. Experimental points obtained from the density matrices are shown as scatter plots, while theoretical predictions from the displaced thermal state model are displayed as continuous lines. Overall, we find good agreement between the model and the experiment. Minor deviations between theory and experiment can be attributed to fluctuations of the thermal photon number during the measurement. As predicted by the model, we observe that $\mathcal{M}$ remains independent of the coherent photon number and stays at a value of approximately 0.52, corresponding to a thermal photon number of around 0.54. At the same time, we note that $\mathcal{P}_{\text{Inc}}$ decreases with increasing photon number, while $\mathcal{C}$ increases.

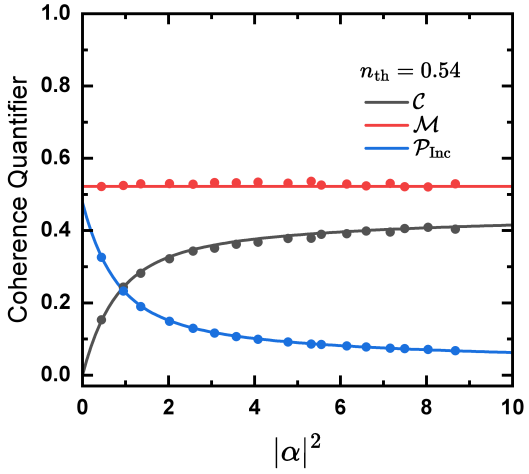

Figure 6.2: Quantum coherence (black), mixedness (red), and purity of the closest incoherent state (blue) for a displaced thermal state of a fixed mean thermal photon number of $n_{\text{th}} = 0.54$ and varied coherent photon number $|\alpha|^2$. The experimental points, calculated from the states' density matrices, are displayed as scatter plots. The theory curves predicted by the displaced thermal state model are displayed as line plots.

In the second scenario, we keep the absolute photon number constant while varying the ratio between coherent and thermal contributions $R = \frac{|\alpha|^2}{n_{\text{th}}}$. Since R becomes at large values highly sensitive to fluctuations in n_{th}, averaging over all recorded iterations does not result in meaningful results. Instead, we restrict the set of considered density matrices according to the following rules. First, we discard all density matrices yielding unphysical negative values for R. Second, we sort the remaining density matrices into quartiles with respect to R and include only

measurements whose extracted R satisfy the condition

$$Q_{50} - 3 \cdot (Q_{50} - Q_{25}) \leq R \leq Q_{50} + 3 \cdot (Q_{75} - Q_{50}) \,, \tag{6.6}$$

where Q_{25}, Q_{50}, and Q_{75} denote the lower quartile, median, and upper quartile of the distribution of the found R. This filter condition ensures that the most measurements are included in the averaging process, while excluding single outliers whose R may be several orders of magnitude larger. The model curves and the experimental results, measured at a mean photon number of $\langle \hat{n} \rangle = 4.5$ and an R varied between 0.01 and 1000, are displayed in figure 6.3 (a). As in the first scenario,

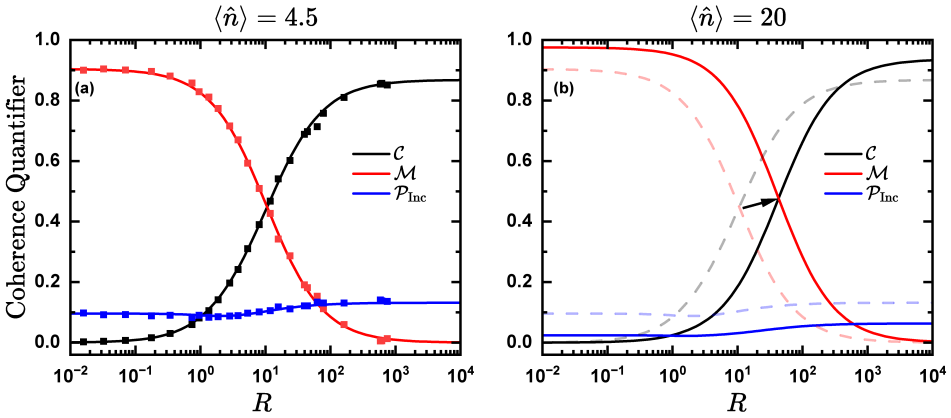

Figure 6.3: Quantum coherence (black), mixedness (red) and purity of the closest incoherent state (blue) for displaced thermal states of mean photon numbers of (a) $\langle \hat{n} \rangle = 4.5$ and (b) $\langle \hat{n} \rangle = 20$, under variation of the coherent to thermal photon number ratio $R = \frac{|\alpha|^2}{n_{\mathrm{th}}}$. The predicted curves are depicted as line plots. Additionally, panel (a) includes experimental result obtained from reconstructed density matrices as scatter plots. To illustrate the differences between $\langle \hat{n} \rangle = 4.5$ and $\langle \hat{n} \rangle = 20$, panel (b) also includes the curves of the former, but grayed out. Adapted from [78].

we observe excellent agreement between the experimental data and the curves predicted by the model. This consistency not only validates the displaced thermal state model but also confirms the reliability of our density matrix reconstruction setup. Minor discrepancies can be primarily attributed to residual deviations of R, which manifest as horizontal shifts between experiment and model. We identify a clear transition from a predominantly thermal state, characterized by significant mixedness, to a predominantly coherent state, characterized by a large quantum coherence. The intersection point of the two quantities lies at around $R = 10$. In contrast, R has only a minor influence on $\mathcal{P}_{\mathrm{Inc}}$ which remains at around 0.1. Further, the relation between R and $\mathcal{P}_{\mathrm{Inc}}$ is unambiguous as $\mathcal{P}_{\mathrm{Inc}}$ exhibits a local minimum at

around $R = 2$. In addition to the comparison between model and experiment, figure 6.3 (b) illustrates the comparison between the predicted curves for $\langle \hat{n} \rangle = 4.5$ and $\langle \hat{n} \rangle = 20$. The increased photon number shifts the curves for quantum coherence and mixedness towards higher ratios, leading to a new intersection point at around $R = 50$. Consequently, increasing the mean photon number does not necessarily increase the amount of quantum coherence. Such a relation holds only for highly coherent states of large R, while $\mathcal{C}$ even reduces for light fields with low and medium R.

6.3 Quantum Coherence and Its Role in Coherent Qubit Control

After validating the displaced thermal state model, we now evaluate the role of quantum coherence in a specific use case: the preparation of qubit states. Our objective is to use two consecutive laser pulses to excite qubits, initialized in the ground state $|g\rangle$, first into the superposition state $|+\rangle = \frac{1}{\sqrt{2}}(|g\rangle + |e\rangle)$ and subsequently into the excited state $|e\rangle$. To describe the excitation protocol in a more intuitive way, we represent the possible qubit states as points on the Bloch sphere [9, p.54-58]. In this representation, the ground and excited states $|g\rangle$ and $|e\rangle$ correspond to the north and south poles of the sphere, while equal superposition states lie on the equator. The first pulse transfers the system from the ground state into a superposition state, whereby the exact polar angle is determined by the time-integrated amplitude of the excitation pulse and the azimuthal angle by its phase. Consequently, the pulse profile must be optimized such that the state is rotated precisely to the equator. Given the first pulse, only a second pulse of identical amplitude and a relative phase of 0 enables an excitation into the excited state. In contrast, a pulse with the correct amplitude but a relative phase of π would drive the system back into the ground state. Therefore, successful state preparation is achieved only when the amplitudes and the relative phase of both pulses are coordinated. This coordination is degraded when the excitation beams include amplitude or phase uncertainties, ultimately preventing an ideal state preparation. The effect of such uncertainties can be interpreted from two equivalent perspectives. In the first perspective, we consider the first pulse well-defined, for example, by rotating the Bloch sphere so that the pulse transfers the system into the state $|+\rangle$. In this case, the shift due to the second pulse becomes uncertain, so that the final state is not known exactly. In the second perspective, we consider the relative shift induced by the second pulse as well-defined. However, the starting point on the Bloch sphere becomes uncertain because the state produced by the first pulse is not perfectly known. In the following three sections, we consider the qubit excitation

protocol in three different excitation scenarios and discuss the quantum coherence in the corresponding reference frames:

1. In the first scenario, a pulsed laser serves as a seed for an optical amplifier as well as a source of the first pulse. The first pulse excites the qubit from the ground into the superposition state, while the output of the optical amplifier is used to drive the system from the superposition into the excited state afterward.
2. In the second scenario, the amplified signal is split into two pulses, which are then used sequentially to perform the qubit excitation.
3. In the third scenario, the amplified signal is again split into two pulses, but we take additional dephasing between the pulses along the optical beam paths into account.

6.3.1 The Synchronization Scenario

In the first scenario, we employ a classical light field as a seed for an optical amplifier. We then use a portion of the seed to excite the qubit from $|g\rangle$ to $|+\rangle$ and the output pulse of the amplifier to drive the system from $|+\rangle$ to $|e\rangle$. In this scenario, the seed acts as the reference frame for the second pulse. Consequently, quantum coherence is degraded by two aspects: First, thermal noise in the emitted light limits the achievable quantum coherence through increased mixedness. Second, fluctuations in the relative phase between the seed and the amplifier emission introduce additional dephasing. Since this issue corresponds to the synchronization of the reference frames of the seed and the amplified light, we refer to this configuration as the synchronization scenario. A direct consequence of the additional phase uncertainty is that the exact amount of quantum coherence cannot be determined solely from its coherent and thermal photon numbers. Instead, quantum state tomography must be employed, using a portion of the seed field as the local oscillator. Nevertheless, knowledge of the state's coherent and thermal photon numbers still allows an estimation of the maximal achievable quantum coherence. Because the random phase fluctuations introduced by the optical amplifier are difficult to suppress, the synchronization scenario is impractical for coherent qubit control. We therefore turn to more promising scenarios in the following sections.

6.3.2 The Interferometric Scenario

In the second scenario, hereafter referred to as the interferometric scenario, we apply a more practical excitation scheme and use a beam splitter to generate both pulses from the field emitted by the optical amplifier. Since any phase fluctuations between the amplifier output and the seed are equally transferred to both pulses, the relative phase between the two pulses remains unaffected. Consequently, the amplifier can be omitted from the subsequent theoretical considerations. In the absence of external phase noise along the beam paths and neglecting the vacuum noise induced by the beam splitter, this configuration produces two pulses that are identical copies of each other and therefore perfectly phase-coherent. This scenario resembles the situation in interferometric experiments, in which one creates two copies of a light field to determine, for example, its classical first-order coherence time. Similarly, we investigate in the interferometric scenario how well a light field can serve as a phase reference for other light fields. However, $\mathcal{C}$ provides an advantage over $g^{(1)}$. In the case of $g^{(1)}$, a relative shift between the two copies - either in time or space - is required to obtain information about the light field. If no delay is introduced, every single-mode light field yields $g^{(1)} = 1$. In contrast, when two unshifted copies are used as signal and phase reference to evaluate $\mathcal{C}$, the result still depends on the state of the light fields. In particular, any thermal component introduces mixedness, which reduces the quantum coherence, even when the two pulses are perfectly phase-aligned. This property implies that, in the interferometric scenario, it is sufficient to determine the coherent and thermal photon numbers of the light field, for example, by measuring the phase-averaged Husimi-Q distribution. As a result, experimental access is significantly simplified, since a stable phase relation between the signal and the local oscillator is no longer required.

6.3.3 The Dephasing Scenario

In the third scenario, we reconsider the excitation scheme of the interferometric scenario, but relax its assumptions to a more realistic level by including additional phase noise between the two pulses. Such phase noise can arise from various sources. For example, coherence may degrade when the optical beam paths are exposed to turbulent airflows or mechanical vibrations. In such cases, the degree of dephasing typically increases with the setup size. Alternatively, instead of splitting a single pulse, consecutive laser pulses may be used to control the qubit. In this situation, the finite coherence time of the light source inherently limits the achievable quantum coherence. Since all these phenomena can be traced back to dephasing, we refer to this configuration as the dephasing scenario. With respect to the underlying decoherence mechanisms, this scenario is closely related to the synchronization

scenario. The crucial difference is that the achievable quantum coherence is not fundamentally limited by the processes of an optical amplifier, which can only be optimized to a limited extent, but can instead often be improved through careful optimization of the setup. In the limit where the coherence time is much longer than the time delay between the two pulses, the dephasing scenario reduces to the interferometric scenario. This distinction is particularly important for the characterization of light sources, as it allows us to differentiate between intrinsic phase noise, which occurs on time scales shorter than the pulse width, and external slow phase noise arising from the experimental setup.

6.4 The Role of Quantum Coherence in Qubit-State Preparation

Following the preceding qualitative discussion of the different excitation scenarios, we next simulate the excitation process to study the role of quantum coherence in the preparation of qubit superposition states quantitatively. These states then serve as a start point for subsequent operations. To this end, we employ the purity of the qubit subsystem to quantify the quality of the created qubit superposition states. The purity reaches a maximal value of $\mathcal{P} = 1$ for a perfect superposition and minimizes at $\mathcal{P} = 0.5$ for a completely mixed state.

6.4.1 Simulation of the Jaynes-Cumming Model

To keep the description of the excitation process both simple and focused on the role of quantum coherence, we consider the simplest system possible: the resonant driving of a qubit $\hat{\rho}_\mathrm{q}$, initially prepared in the ground state $|g\rangle$, by a single-mode light field $\hat{\rho}_\mathrm{c}$, neglecting all kinds of losses or other perturbations. Under these assumptions, the system corresponds to the resonant lossless Jaynes-Cumming model [79, p. 423], described by the Hamilton operator

$$\hat{H} = \frac{1}{2}\hbar\omega_\mathrm{q}\hat{\sigma}_\mathrm{z} + \hbar\omega_\mathrm{c}\hat{a}^\dagger\hat{a} + \hbar g\left(\hat{a}^\dagger\hat{\sigma} + \hat{a}\hat{\sigma}^\dagger\right), \tag{6.7}$$

where $\hat{a}$ and $\hat{a}^\dagger$ denote the annihilation and creation operators of the light field, $\hat{\sigma}$ and $\hat{\sigma}^\dagger$ define the lowering and raising operators of the qubit, and $\sigma_\mathrm{z} = \hat{\sigma}^\dagger\hat{\sigma}$ represents the qubit inversion operator. Furthermore, we define the energy level separation of the qubit states $\hbar\omega_\mathrm{q}$, the energy of the photon mode $\hbar\omega_\mathrm{c}$, and the Rabi energy $\hbar g$. Since we consider resonant excitation, we set $\hbar\omega_\mathrm{q} = \hbar\omega_\mathrm{c}$. The time

evolution of the coupled system, described by $\hat{\rho}_\mathrm{j} = \hat{\rho}_\mathrm{c} \otimes \hat{\rho}_\mathrm{q}$, is then given by the Liouville-von Neumann equation [79, p. 24]

$$\frac{\mathrm{d}}{\mathrm{d}t}\hat{\rho}_\mathrm{j} = -\frac{i}{\hbar}\left[\hat{H}, \hat{\rho}_\mathrm{j}\right] . \tag{6.8}$$

Finally, we obtain the time evolution of the qubit state by tracing out the photon mode. The simulations were executed numerically using Python and the QuTIP package [80].

We begin the analysis by studying the time evolution of a single qubit that is coupled to different light fields. For this purpose, figure 6.4 illustrates the time traces of the qubit excitation probability (black) and the qubit purity (red) of a qubit coupled either to a coherent light field $\hat{\rho}_\mathrm{Coh}$, a thermal light field $\hat{\rho}_\mathrm{th}$, or a completely dephased coherent light field $\hat{\rho}_\mathrm{Coh,Inc}$ of average photon number $\langle\hat{n}\rangle = 30$. The graphs in the left column [panels (a), (c), and (e)] display the time evolution on long timescales up to $gt = 50$, while the graphs in the right column [panels (b), (d), and (f)] focus on the time evolution on short timescales up to $gt = 3$. We begin the discussion with the coherently driven qubit, where the light field exhibits coherence both in terms of conventional second-order correlations and quantum superpositions. In this case, the time evolution of the qubit follows the well-documented nontrivial Jaynes-Cummings dynamics. On long timescales, we observe initial collapse and later revival of the qubit excitation probability [81, 82, 83]. Meanwhile, we note that the purity reaches a local maximum inside the collapse region, reaching a value of almost one [82, 83]. On short timescales, the excitation probability exhibits damped Rabi oscillations that converge to 0.5. Particular attention is drawn to $gt \approx 0.15$, where the system reaches a nearly perfect superposition state, associated with the excitation by a $\frac{\pi}{2}$ pulse. In the next step, we examine how the dynamics change in the interferometric and the dephasing scenario. For the interferometric scenario, we consider the most extreme case and drive the qubit with a thermal state $\hat{\rho}_\mathrm{th}$ that is incoherent both in terms of second-order coherence and quantum coherence. In this case, the excitation probability exceeds 0.5 once before it decays. Simultaneously, we observe that the purity decays nearly immediately and remains at 0.5 for times beyond $gt = 0.5$. For the dephasing scenario, we again consider the extreme case and excite the qubit with a completely dephased coherent state $\hat{\rho}_\mathrm{Coh,Inc}$, which is coherent according to $g^{(2)}$ but incoherent in terms of quantum coherence. We observe that the time evolution of the qubit excitation probability is identical to that of a coherently driven qubit, indicating that the qubit excitation probability solely depends on the photon statistics of the excitation light field. In contrast, the time evolution of the purity differs significantly, showing that the qubit purity depends on the quantum coherence of the driving light field. The purity may increase when the excitation probability becomes extremal, but returns to 0.5 when

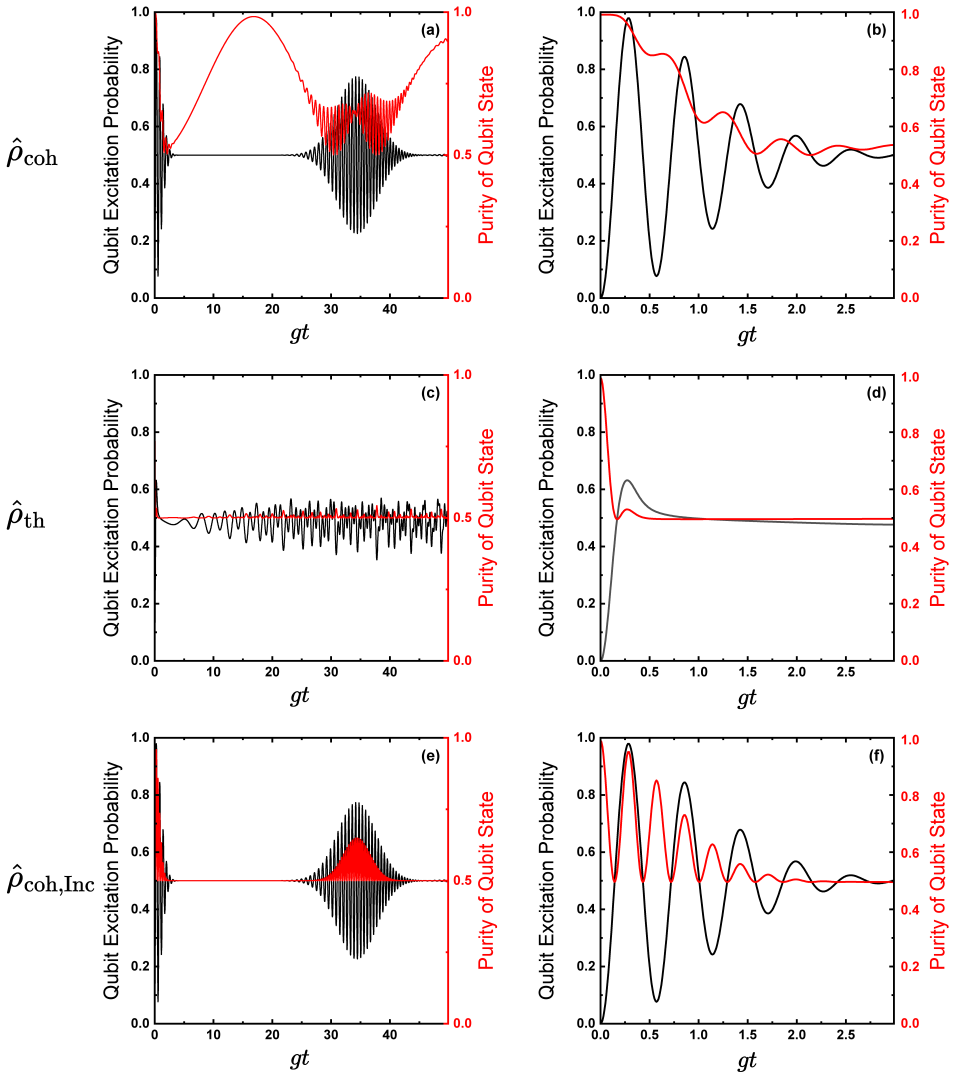

Figure 6.4: Time evolution of a single qubit coupled to a coherent light field (first row), a thermal light field (second row), and a completely dephased coherent light field (third row), with a mean photon number of 30, respectively. The left column [panels (a), (c) and (e)] displays the time evolution on long timescales up to $gt = 50$, while the right column [panels (b), (d) and (f)] focuses on the short-time dynamics up to $gt = 3$. Each panel shows the probability of finding the qubit in the excited state (black) and the state's purity (red). Adapted from [78].

the probability drops back to 0.5. As a consequence, the purity also exhibits no rephasing peak within the collapse region. This leads to our first central result: The generation of pure qubit superposition states with a classical light field requires the presence of quantum coherence in the driving field. Further, we note that the purest superposition states are achieved by excitation with a single $\frac{\pi}{2}$ pulse. For this reason, we focus from now on exclusively on the excitation with $\frac{\pi}{2}$ pulses, while denoting the purity of the created qubit superposition state $|+\rangle$ with $\mathcal{P}_{\frac{\pi}{2}}$. Using these results as a starting point, we study the relationship between the quantum coherence of the driving field and the achievable $\mathcal{P}_{\frac{\pi}{2}}$ in the interferometric and dephasing scenario in the following two sections in more detail.

6.4.2 Qubit Preparation in the Interferometric Scenario

We begin the analysis with the qubit preparation in the interferometric scenario. To this end, we keep the mean total photon number $n_{\mathrm{DT}} = |\alpha|^2 + n_{\mathrm{th}}$ constant, while varying the ratio between the coherent and thermal contributions $R = \frac{|\alpha|^2}{n_{\mathrm{th}}}$. All simulations are repeated for mean photon numbers of 3, 5, 10, 15, and 20. The dependence of $\mathcal{P}_{\frac{\pi}{2}}$ on the quantum coherence of the driving light field $\mathcal{C}$ is depicted in figure 6.5 (a). In the case of thermal excitation, the qubit always evolves into

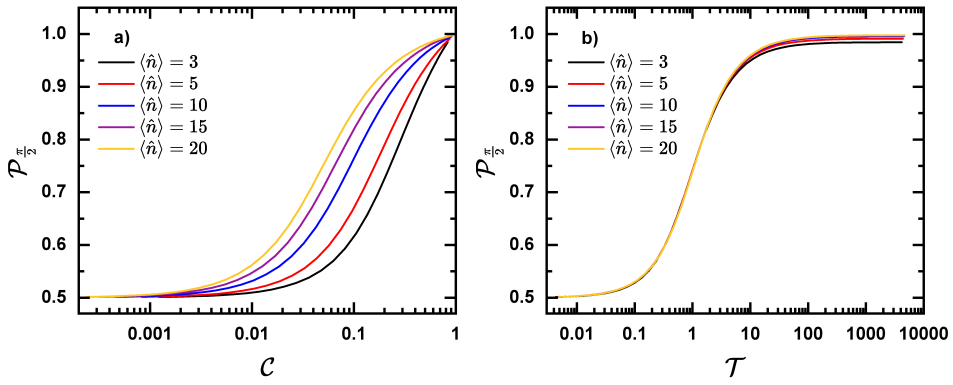

Figure 6.5: Purity of the excited superposition state $\mathcal{P}_{\frac{\pi}{2}}$ in the interferometric scenario, dependent on the quantum coherence $\mathcal{C}$ (a) and the tightness $\mathcal{T}$ (b) of the exciting light field. The simulations are performed for mean photon numbers of 3, 5, 10, 15, and 20. Adapted from [78].

a maximally mixed state, independent of the photon number. However, as the quantum coherence increases, the curves begin to separate. Accordingly, a larger photon number leads, at equal quantum coherence, to a higher $\mathcal{P}_{\frac{\pi}{2}}$. This behavior is expected, as the duration of a $\frac{\pi}{2}$ pulse reduces with increasing photon number,

thereby reducing the time available for the qubit to dephase. For nearly coherent excitation, the quantum coherence is limited solely by the remaining $\mathcal{P}_{\mathrm{Inc}}$, which decreases with increasing mean photon number. Consequently, a coherent state of higher photon number exhibits a higher quantum coherence and, correspondingly, leads to a higher $\mathcal{P}_{\frac{\pi}{2}}$. Our simulations display that the quantum coherence constitutes a suitable quantity to estimate the achievable $\mathcal{P}_{\frac{\pi}{2}}$. However, its dependency on the photon number as well as its limited discriminatory power in the regime of highly coherent states, complicates its practical application in industrial environments. To provide a more intuitive relationship between the coherence of the driving field and the achievable qubit superposition purity, we introduce the tightness $\mathcal{T}$, defined by

$$\mathcal{T} = \frac{\mathcal{C}}{\mathcal{M}} \langle \hat{n} \rangle \,. \tag{6.9}$$

To compare the dependencies of $\mathcal{P}_{\frac{\pi}{2}}$ on $\mathcal{C}$ and $\mathcal{T}$, figure 6.5 (b) displays the same set of simulations, now plotted against the thightness of the driving field. We note that the tightness unifies the relationship between the coherence of the field and $\mathcal{P}_{\frac{\pi}{2}}$ in the regime of low and medium-coherent light fields. For highly coherent fields, the curves separate again according to the photon number; however, this separation is easier to identify.

Following this more application-oriented discussion, we next examine the connection between the quantum coherence of the driving field and obtainable $\mathcal{P}_{\frac{\pi}{2}}$ in more detail. To this end, it is important to note that we consider a two-level system, and the qubit accordingly interacts only with a single photon of the field at a time. This means, in return, that only quantum superpositions of adjacent Fock states - associated with the first off-diagonal elements of the density matrix - will play a relevant role in preparing the qubit superposition state. The situation may change when considering systems with more than two energy levels. To account for this restriction of a two-level system, we introduce, alongside the regular quantum coherence $\mathcal{C}$, the first-order quantum coherence $\mathcal{C}_1$

$$\mathcal{C}_1 = \sum_{m \in \mathbb{N}} \left[|\rho_{m+1,m}|^2 + |\rho_{m,m+1}|^2 \right] \tag{6.10}$$

which arises from the first-order off-diagonals of the density matrix. The relation between $\mathcal{P}_{\frac{\pi}{2}}$ and $\mathcal{C}_1$ is illustrated in figure 6.6. The curves exhibit the same splitting behavior as observed for the regular quantum coherence and are likewise ordered according to photon number. The purity $\mathcal{P}_{\frac{\pi}{2}}$ initially increases approximately linearly with $\mathcal{C}_1$ before reaching a plateau after the thermal contribution diminishes. Both the gradient of the initial increase and the width of the plateau grow with increasing photon number. Furthermore, we note that the maximal first-order

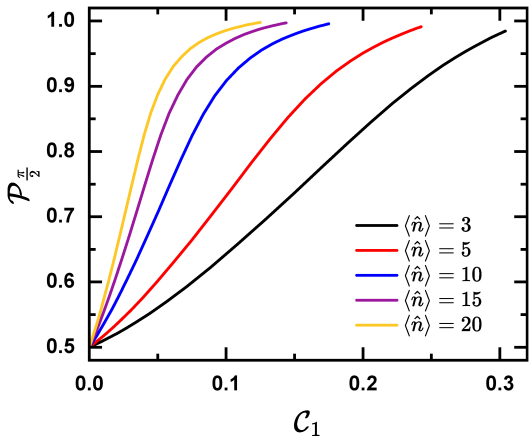

Figure 6.6: Purity of the excited super position state $\mathcal{P}_{\frac{\pi}{2}}$ in the interferometric scenario, dependent on the first-order quantum coherence $\mathcal{C}_1$ of the excitation light field. The simulations are performed for mean photon numbers of 3, 5, 10, 15, and 20. Adapted from [78].

quantum coherence $\mathcal{C}_1$, obtained for a coherent state, decreases with increasing photon number, which is contrary to the behavior of the regular quantum coherence. This effect arises from the distribution of the off-diagonal elements within the density matrix of the coherent state, which broadens along the matrix anti-diagonal axis with increasing mean photon number. In return, the absolute value of the individual off-diagonal elements decreases, even though their total sum, and thus $\mathcal{C}$, increases.

We conclude the discussion of the interferometric scenario by studying the maximal achievable purity $\mathcal{P}_{\frac{\pi}{2},\max}$, attained when driving the qubit with an ideal coherent state, as a function of $|\alpha|^2$. The associated graph, extracted from corresponding simulations, is displayed as a black line plot in figure 6.7. The curve begins at a minimal coherent photon number of 0.9, leading to a qubit superposition purity $\mathcal{P}_{\frac{\pi}{2},\max}$ of around 0.91. Below 0.9 photons, no purity could be determined as the excitation field is too weak to drive the qubit into the desired superposition state. From this threshold on, the purity increases highly nonlinearly with photon number. It exceeds 0.98 at 2.5 photons and reaches 0.99 at 5 photons. For higher photon numbers, the curve gradually saturates and slowly converges towards unity. For practically relevant photon numbers of 10 and above, we can approximate the simulated relation by the analytic expression

$$\mathcal{P}_{\frac{\pi}{2}} \approx 1 - \frac{1}{2}\mathcal{P}_{\mathrm{Inc}}^2\,, \tag{6.11}$$

which shows that the attainable qubit purity is limited by the residual $\mathcal{P}_{\mathrm{Inc}}$ of the excitation light field. The associated curve is shown as a red dashed line in

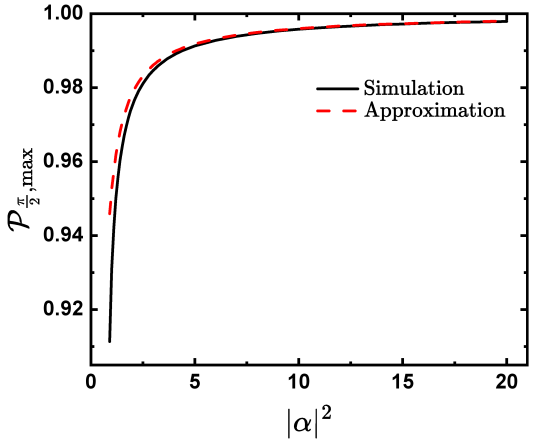

Figure 6.7: Maximal obtainable qubit purity $\mathcal{P}_{\frac{\pi}{2},\max}$ following excitation with a coherent $\frac{\pi}{2}$ pulse, dependent on mean photon number of the exciting pulse $|\alpha|^2$. Simulation results are displayed in black. A corresponding analytical approximation is shown as a dashed red line. Further details are given in the text. Adapted from [78].

figure 6.7. The approximation breaks down for small photon numbers of 5 or below, where the photon number fluctuations exceed the photon number itself. This additional noise reduces the achievable qubit purity compared to the value predicted by the approximation. The effect can be compensated by subtracting an additional phenomenological term of the form $\frac{1}{2}\exp(-3|\alpha|^2)$. In practice, however, one should avoid the regime of low photon numbers anyway, as the enlarged photon-number noise complicates the generation of well-defined $\frac{\pi}{2}$ pulses.

6.4.3 Qubit Excitation in the Dephasing Scenario

After investigating the interferometric scenario in the previous section, we now turn our attention to the dephasing scenario. To ensure that the dephasing mechanism does not alter the photon statistics of our light field, we restrict our analysis to pure dephasing. In this case, the driving light field is in contact with a bath of incoherent photons such that both parties can exchange photons, without changing the photon statistics [79, p. 171]. The exchange process is characterized by the exchange rate $\gamma = \omega_c^2\gamma'$, which becomes constant in the case of single-mode excitation. The time evolution of the density matrix elements $\rho_{m,n}(t)$ under pure dephasing is then given by

$$\rho_{m,n}(t) = \exp\left(-i\omega_c\left[m-n\right]\right)\cdot\exp\left(-\gamma\left[m-n\right]^2 t\right)\rho_{m,n}(0) \tag{6.12}$$

The first exponential term describes ultrafast oscillations of the off-diagonal terms that, however, do not alter the coherence properties of the state. The second term, in contrast, induces an exponential decay of the off-diagonal elements. As the associated decay rate increases quadratically with the order of the off-diagonal elements $|m - n|$, elements on higher-order off-diagonals decay faster compared to the elements on the first off-diagonal. As in the interferometric scenario, we excite a single qubit from its ground state into the superposition state using a $\frac{\pi}{2}$ pulse. We then analyze the purity of the prepared superposition state $\mathcal{P}_{\frac{\pi}{2}}$ and relate it to the coherence properties of the driving light field. To investigate the impact of pure dephasing under realistic conditions, each simulation begins with a displaced thermal state of ratio $R = 100$, which is then exposed to different amounts of pure dephasing and, afterward, coupled to the qubit system. As in the interferometric scenario, all simulations are performed for photon numbers of 3, 5, 10, 15, and 20. We begin the analysis with the relation between $\mathcal{P}_{\frac{\pi}{2}}$ and the dephasing parameter

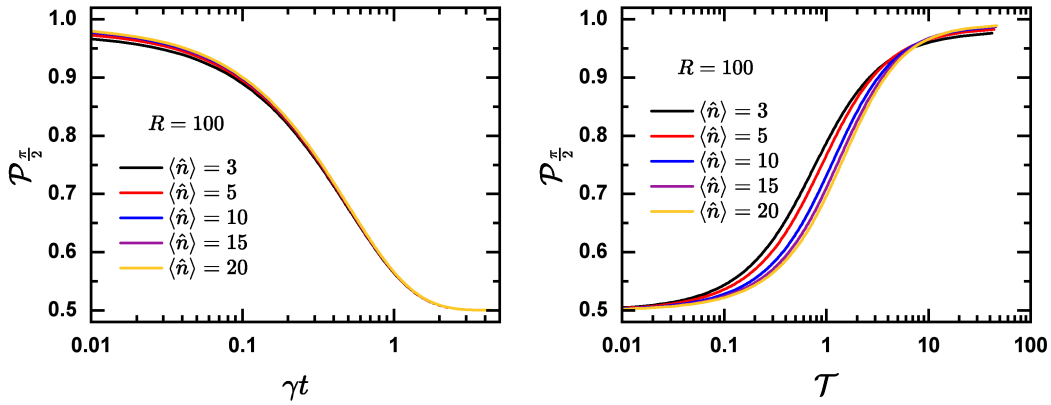

Figure 6.8: Purity of the excited qubit superposition state $\mathcal{P}_{\frac{\pi}{2}}$ in the dephasing scenario, either in dependence of the dephasing constant γt (a) or the tightness $\mathcal{T}$ of the driving light field (b). All dephasing operations are applied on a displaced thermal state of ratio $R = 100$. The simulations are performed for mean photon numbers of $3, 5, 10, 15$ and 20. Adapted from [78].

γt, depicted in figure 6.8 (a). In the weak dephasing regime, the curves exhibit a characteristic splitting behavior as $P_{\frac{\pi}{2}}$ is upper bounded by the residual $\mathcal{P}_{\text{Inc}}$ of the excitation light field. As the degree of dephasing increases, the obtainable qubit purities decrease non-linearly and gradually converge to a single curve. At $\gamma t = 1$, the curves have effectively merged, and the purity has dropped to approximately 0.55. Finally, we obtain a nearly maximally mixed state at around $\gamma t = 3$. In addition to examining the dependence of $\mathcal{P}_{\frac{\pi}{2}}$ on γt, we also study its relation to $\mathcal{T}$, when the dephasing is included directly into $\mathcal{T}$. The corresponding graph is displayed in figure 6.8 (b). The tightness reaches its maximum in the absence of

dephasing, which consequently also yields the highest $\mathcal{P}_{\frac{\pi}{2}}$. In the intermediate regime, we not only note a splitting of the curves - unlike to the interferometric scenario - but also a reversed curve order. This behavior follows from the definition of the tightness, as a less intense light field requires a higher degree of quantum coherence to achieve the same tightness. The fact that quantum coherence and mixedness are furthermore correlated with $\mathcal{P}_{\mathrm{Inc}}$, however, complicates the relations, so one clearly sees that the tightness is a quantifier for the maximal obtainable purity, but not for directly including dephasing. This is expected as the obtainable qubit purity depends only on the entries in the first off-diagonals of the density matrix, while dephasing affects the different off-diagonals in a dissimilar manner. We conclude our study of the dephasing scenario with the relation between $\mathcal{P}_{\frac{\pi}{2}}$ and $\mathcal{C}_1$. The associated graphs are depicted in figure 6.9. As in the interferometric

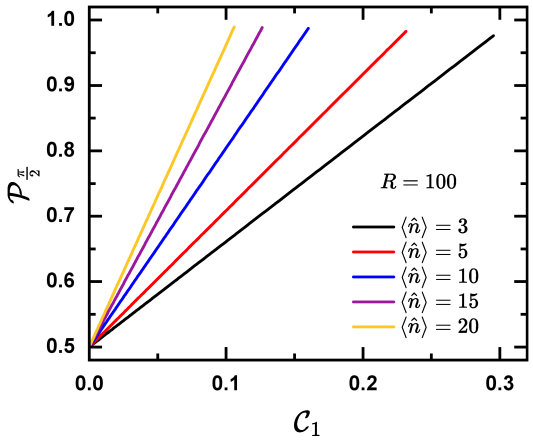

Figure 6.9: Purity of the qubit superposition state $\mathcal{P}_{\frac{\pi}{2}}$ in the dephasing scenario, dependent on the first-order quantum coherence $\mathcal{C}_1$ of the driving light field. All dephasing operations are applied on a displaced thermal state of ratio $R = 100$. The simulations are performed for mean photon numbers of $3, 5, 10, 15$ and 20. Adapted from [78].

scenario, the curves are ordered by increasing photon number, the relation between $\mathcal{C}_1$ and $\mathcal{P}_{\frac{\pi}{2}}$ is, however, linear. Consequently, the dephasing scenario can be traced back on the interferometric scenario.

6.5 Conclusion

In summary, we have developed a simple resource-theoretical model describing the formation of quantum coherence during the onset of the lasing process. We have demonstrated that the attainable quantum coherence of a light field, emitted by a maser or laser, is upper-bounded by the mixedness of the light field, which originates from residual thermal noise, and by the purity of the closest incoherent state. Furthermore, we experimentally validated our theoretical predictions and confirmed the model's central results using quantum state tomography, achieving excellent agreement between the model and the experiment. Moreover, the ability to tune the thermal and coherent contributions of the signal during the experiment underscores the versatility and performance of our in situ quantum state tomography setup. Our simulations of single-qubit excitation driven by a realistic coherent light source revealed that quantum superpositions play a decisive role in the preparation of coherent qubit superposition states. Consequently, quantum coherence emerges as a reasonable quantifier to quantify the usefulness of a partially coherent light field for the preparation of a superposition state in a qubit, where the commonly used second-order correlation function $g^{(2)}$ fails to provide reliable predictions over the purity of the final qubit superposition state. For this purpose, we studied the qubit preparation in three different excitation scenarios. Notably, we find that within the interferometric scenario, quantum coherence can be determined without the need for a fixed phase reference. This simplifies the integration of detectors that measure the quantum coherence into established experimental setups and testing processes.

Although our simulations are restricted to the specific task of preparing a single qubit in order to demonstrate the capabilities of our framework, the underlying principles can be transferred to more complex and experimentally more relevant protocols [84, 85, 86, 87]. Alternatively, earlier studies on coherent qubit control could be revisited from the perspective of quantum coherence and the use of realistic coherent light sources [88, 89]. More broadly, it appears advantageous to incorporate quantum resource theories already at an early stage in the design and development of new coherent light sources. An example would be the construction of miniaturized coherent light sources for integrated quantum computing. This study may also serve as a starting point for investigating the coherence properties of further partially coherent light sources in the broader scope of quantum resource theories. This includes not only maser and laser systems but also encompasses other non-conventional partially coherent light sources such as free-electron lasers [90] and Bose-Einstein condensates, created from photons [91] or polaritons [39]. At last, even spectroscopic applications can benefit from the study of quantum coherence. For example, recent studies have revealed that the Cherenkov radiation, which has so far been described in a classical way, involves underlying quantum-mechanical

processes [92]. For this purpose, the interplay between the quantum coherence of the emitter and the classical phase coherence of the emitted signal was investigated. In this regard, the analysis of the quantum resource of the emitted light field could lead to further insights.

7 Enhancing the Quantum Coherence of a Polariton Condensate

Technological developments over the past decades have led to remarkable advances in quantum computation and quantum information science, providing solutions to emerging challenges in quantum security [93], quantum machine learning [94], and quantum optimization [95]. The range of experimentally accessible qubit platforms has expanded significantly, and nowadays includes systems such as trapped ions [2, 96, 97], superconducting circuits [98, 99], and photonic architectures [100, 101]. At the same time, progress in reducing losses in quantum channels enabled quantum communication over increasingly large distances [102, 103, 104, 105]. Nevertheless, no single qubit platform is ideal for all types of quantum operations. In this regard, matter-based platforms usually outperform photonic systems in quantum computation, whereas photonic platforms are indispensable for transmitting quantum information between different locations. For this reason, hybrid quantum devices capable of transferring quantum information between matter-based and photonic systems are required [106]. Exciton-polaritons represent promising candidates for such hybrid quantum devices due to their hybrid light-matter character. On the one hand, resonant excitation enables the optical imprinting of quantum information on the polariton population. On the other hand, polaritons transfer their quantum information to emitted photons upon decay. Furthermore, polaritons can, due to their bosonic character, exhibit a variety of nontrivial collective phenomena, such as polariton lasing [107], superfluidity [108], and the phase transition into a Bose-Einstein condensate-like state [39]. The latter is accompanied by the buildup of coherent superpositions in the polariton system. This feature renders polariton condensates, as we had discussed in the previous chapter, interesting for a wide range of quantum informational applications in quantum thermodynamics, quantum algorithms, and quantum metrology [109]. In this context, understanding and optimizing the condensation process and the associated buildup of quantum superpositions is crucial for hybrid quantum technologies [110, 111, 112, 113, 114, 115]. The objective of this chapter is to characterize and optimize the condensation process of a non-resonantly excited polariton condensate. To this end, we combine a semiconductor microcavity, which provides long-lived polaritons, with an annular-shaped excitation beam, thereby separating the condensate area from the excitation area and minimizing interactions between both. In this context, previous

studies have already demonstrated that the spatial separation of excitation area and condensate improves the spatial [45] and temporal [46, 47] first-order coherence $g^{(1)}$. To examine the condensation process and the buildup of coherence, we employ classical spectroscopy and homodyne detection. Detailed information about the experimental setup and the used sample is provided in chapter 5.

The remainder of this chapter is structured in four sections, whereby the contents of the first three sections formed the base of the published paper 'Quantum coherence of a long-lifetime exciton-polariton condensate' [63]. We start the studies by validating the condensation process in section 7.1. Subsequently, in section 7.2, we examine the temporal stability of the condensate state through the time-resolved analysis of $\langle \hat{n} \rangle$ and $g^{(2)}(0)$. In section 7.3, we extend the investigation to the phase-averaged Husimi-Q distribution. The application of the displaced thermal state model then provides access to the quantum coherence of the condensate state in terms of the interferometric scenario that we introduced in the previous chapter. Finally, in section 7.4, we relax the restriction of a stationary condensate state and investigate the influence of intensity noise on the coherence properties of the intensity-averaged state. We conclude the chapter by introducing a time-resolved version of the Husimi-Q analysis, which enables us to inspect the temporal evolution of quantum coherence in the presence of external perturbations.

7.1 Spectroscopic Characterization of the Polariton-Condensation Process

Before analyzing the coherence properties of the light field emitted by the sample, two conditions must be verified. First, we have to validate that the polariton population within the sample forms a polariton condensate, and second, we have to ensure that the condensate is spatially separated from the excitation area. To examine these criteria, we excite the sample with an excitation beam of annular shape, drive the system across the condensation threshold, and investigate the resulting changes in the radiated emission using spectroscopic methods. The corresponding results at three representative excitation powers (I) below threshold, (II) at threshold, and (III) above threshold are shown in figure 7.1. The left column displays the two-dimensional real-space emission, while the right column shows the one-dimensional dispersion along k_y for fixed $k_x = 0\,\mu\text{m}^{-1}$.

Below the condensation threshold, the real-space image of the polaritons resembles the annular profile of the excitation beam, as polariton scattering toward the ring center plays only a minor role. Nevertheless, polariton-phonon scattering already broadens the thickness of the ring compared to the excitation profile. In momentum

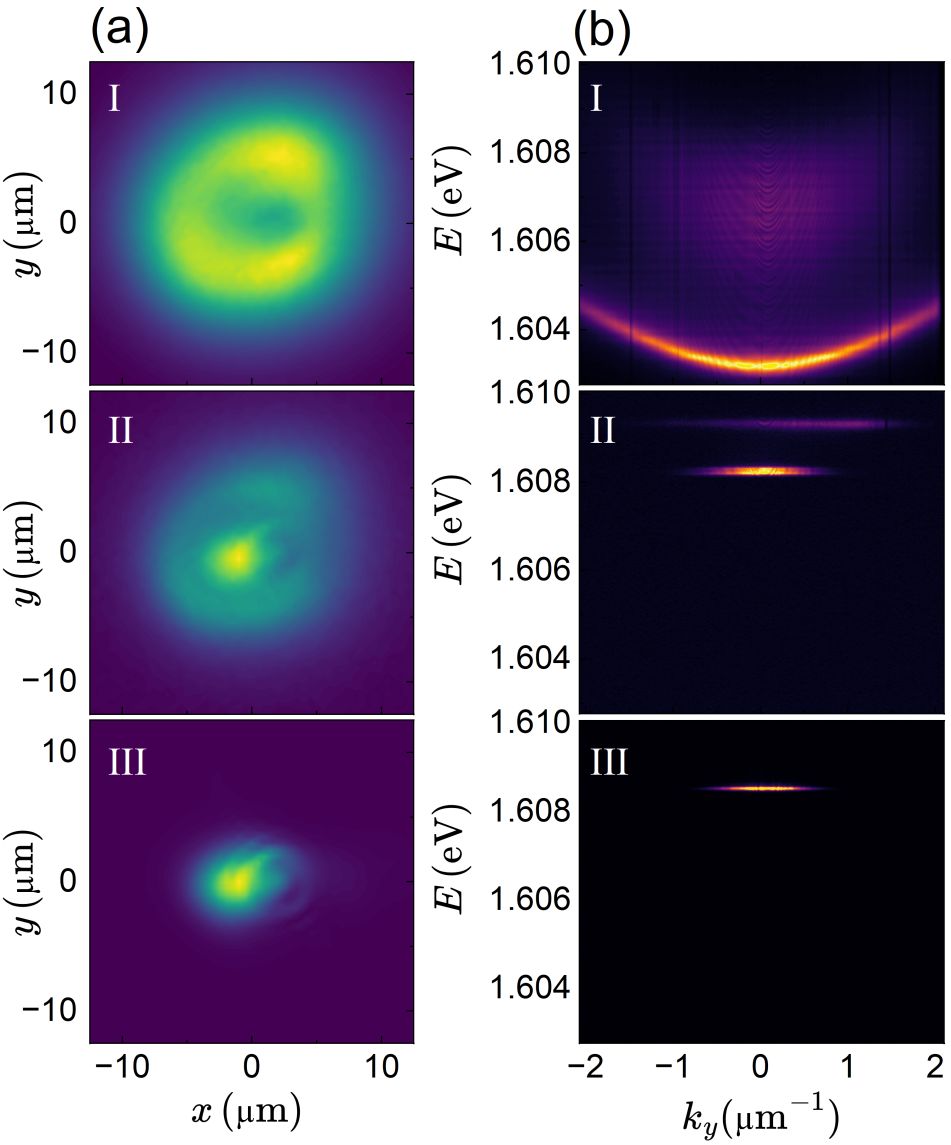

Figure 7.1: Polariton emission in (a) real- and (b) momentum-space for different excitation intensities of (I) $0.57\,P_{\mathrm{th}}$, (II) $1.00\,P_{\mathrm{th}}$ and $1.35\,P_{\mathrm{th}}$. The heatmaps of case (II) are averaged over several iterations as the system shows instabilities around the threshold. Adapted from [63].

space, the dispersion of the lower polariton branch (LPB) exhibits the characteristic parabolic shape associated with uncondensed polaritons below the condensation threshold, while the ground state energy amounts to 1.603 eV. At the threshold, the polariton system destabilizes, such that minimal fluctuations in the excitation geometry can induce a phase transition from an incoherent polariton population to a coherent condensate state and vice versa. To accommodate this instability, the heatmaps shown in regime (II) represent averages over multiple successive measurements recorded under nominally identical experimental conditions. The real-space image clearly reflects the state's instability, as contributions not only arise from the ring but also from its center, indicating a successful separation between the excitation area and the condensate. Simultaneously, the dispersion narrows to a region around $k_y = 0\,\mu\text{m}^{-1}$, while its energy decreases in linewidth and blueshifts by around 5 meV. As for the real-space image, the dispersion heatmap is averaged over several iterations. The dispersion of the lower polariton branch is, however, not visible, as its intensity is too low compared to that of the condensate state. Since the first signs of condensation appear at this excitation power, we define it as the threshold power P_{th}. Above threshold, the condensed state stabilizes, and the emission originates predominantly from the ring center. The momentum-space dispersion supports this interpretation as the emission line further localizes around $k_y = 0\,\mu\text{m}^{-1}$, accompanied by an additional blueshift and a further reduction in linewidth.

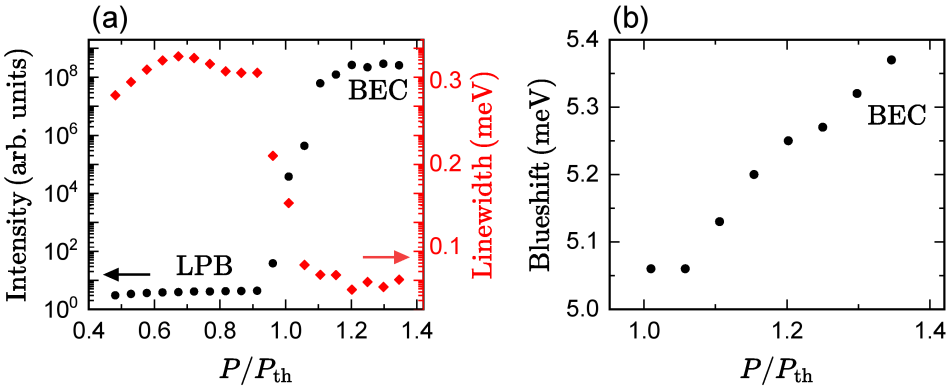

Figure 7.2: (a) Polariton state intensity and spectral linewidth dependent on the excitation power. (b) Polariton blueshift relative to the ground state level of the lower polariton branch. The excitation power is given in units of the threshold power. Further details on the analysis are given in the text. Adapted from [63].

To quantitatively support these preliminary results, we plot the evolution of the intensity, the linewidth, and the blueshift of the condensate mode as functions of the excitation power, presented in units of the threshold power P_{th}. For this purpose,

we analyze the recorded dispersions and respectively, extract an energy-dependent intensity profile from a narrow region around $k_y = 0\,\mu m^{-1}$ with a width of $1\,\mu m^{-1}$. The graphs depicted in figure 7.2(a) display the evolution of the emission intensity (black) and linewidth (red). Below the condensation threshold, the uncondensed lower polariton branch is taken into account; above the threshold, focus is set on the condensate mode. The graph in figure 7.2(b) shows the blueshift of the condensate mode above P_{th}. We observe that the emission intensity increases by approximately eight orders of magnitude when the power is driven across the condensation threshold. Meanwhile, the linewidth drops by a factor of around six. Together, these effects constitute clear signatures of condensation. In addition, the blueshift exhibits a step-like increase of about 5 meV as the population transits from the lower polariton branch into the condensate mode. Above the condensation threshold, the blueshift scales linearly with excitation power. At first glance, the comparably large blueshift, stronger than observed in other $GaAs$-based microcavities [116, 117, 118], appears surprising, especially as the spatial separation between condensate and excitation area should lead to a reduced blueshift. However, other experiments in comparable microcavities have demonstrated that dark excitons with large in-plane momentum, located beyond the light cone, can propagate distances exceeding 30 µm before decaying [119]. Given that our annular trap has a diameter of only 9.6 µm, it is reasonable to assume that the condensed polaritons still interact with dark-excitons [120]. In this context, it is important to emphasize that the long lifetime of these dark-exciton states facilitates their efficient thermalization. As a result, we expect that the interactions with dark excitons, in contrast to the interactions with strongly fluctuating particles, lead to a constant and homogeneous modification of the potential landscape. This observation may indicate that the condensate's coherence is not primarily limited by the mere presence of a reservoir, but rather by fluctuations within it. The objective of the subsequent homodyne analysis is therefore to elucidate the role of fluctuations on the coherence properties of the generated condensate [121, 122].

7.2 Time-Resolved Analysis of $\langle \hat{n} \rangle$ and $g^{(2)}(0)$

After validating both the condensation process and the spatial separation between the condensate and the excitation area in the previous section, we now focus on the coherence properties of the emitted light field. To this end, we direct the emission of the sample to a four-port detector, as introduced in section 4.2.1, and examine the time evolution of the mean photon number $\langle \hat{n} \rangle(t)$, and the second-order correlation function $g^{(2)}(t, 0)$, according to section 4.3.3. As we are interested in the condensate mode, the local oscillator is spectrally aligned with it while avoiding overlap with

the ground state of the uncondensed polaritons. To evaluate the ensemble averages in the computation of $\langle\hat{n}\rangle(t)$ and $g^{(2)}(t,0)$, we employ a rolling window calculation using a window size of 30000 quadratures and a step size of 10000 quadratures. The time traces of $\langle\hat{n}\rangle(t)$ and $g^2(t,0)$ for excitation powers of $1.05\,P_{\mathrm{th}}$, $1.10\,P_{\mathrm{th}}$ and $1.35\,P_{\mathrm{th}}$ over a representative time interval are presented in panels (a) and (b) of figure 7.3. When the system is close to the threshold power, it has usually not yet stabilized but exhibits fluctuations between different modes. These fluctuations can induce the system to go in and out of the condensed phase [118]. Since the emission intensity of the uncondensed phase is too low to record it with the employed homodyne setup, we focus in this study purely on the condensed phase. To this end, we apply a simple intensity filter with a threshold photon number of 0.6 to differentiate between time intervals of the uncondensed and condensed phase. This is possible since phase transitions occur on timescales that are fast compared to the time resolution of the analysis. For clarity, the time intervals during which the system remained in the uncondensed phase are shaded gray in the photon number graph and omitted from the $g^{(2)}$ graph.

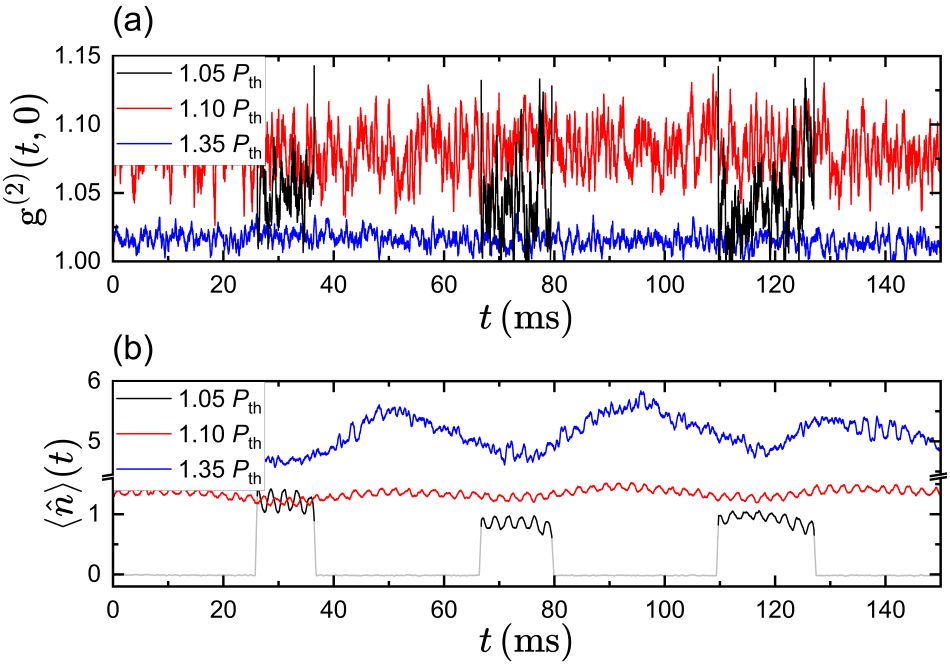

Figure 7.3: Time traces of the time-resolved equal-time second order correlation function $g^{(2)}(t,0)$ (a) and the mean photon number $\langle\hat{n}\rangle(t)$ (b) for different excitation powers of $1.05\,P_{\mathrm{th}}$, $1.10\,P_{\mathrm{th}}$ and $1.35\,P_{\mathrm{th}}$. For clarity, time intervals corresponding to the uncondensed state are grayed out in the $\langle\hat{n}\rangle(t)$ traces and omitted in the $g^{(2)}(t,0)$ traces. Adapted from [63].

At $P = 1.05\,P_{\mathrm{th}}$, close to the condensation threshold, the polariton system is found - consistent with the spectroscopic analysis - in a highly unstable regime, switching on the millisecond scale between the uncondensed and condensed phases. In the latter the photon number rises to around $\langle \hat{n} \rangle \approx 1$, while $g^{(2)}(t, 0)$ drops to around 1.04, indicating the buildup of coherence. However, the system remains unstable, as evidenced by the temporal fluctuations inside $g^{(2)}(t, 0)$. Increasing the excitation power slightly to $P = 1.10\,P_{\mathrm{th}}$ stabilizes the system against external perturbations, such that the polariton system remains consistently in the condensed state. The average photon number, however, does not increase significantly at this stage, while $g^{(2)}(t, 0)$ even rises slightly to 1.08. We attribute this effect to residual uncondensed polaritons. At the highest recorded excitation power of $P = 1.35\,P_{\mathrm{th}}$, the system has fully stabilized as the condensate mode has become the dominating mode. The average photon number increases to around 5, while $g^{(2)}(t, 0)$ decreases to approximately 1.02, indicating that the majority of the excited polariton population is in the condensed state. Further, the fluctuations in $g^{(2)}$ observed at lower powers are substantially reduced. A final aspect deserving attention concerns the nearly harmonic oscillations visible in the photon-number time traces, which persist over all examined excitation powers. A Fourier analysis reveals two dominant frequency components at approximately 24 Hz and 418 Hz hinting a mechanical origin. We therefore attribute these oscillations to external mechanical vibrations that modulate the relative distance between the microscope objective and the sample. This variation leads to a modulation of the effective trap size and, consequently, of the condensation efficiency. In contrast, the second-order correlation function remains unaffected as the oscillation periods are long compared to the temporal resolution of the $g^{(2)}(t, 0)$ calculation [61].

7.3 Time-Averaged Coherence Analysis Based on the Husimi-Q Distribution

In the previous section, we obtained initial insights into the coherence of the condensed polariton system from the time traces of $g^{(2)}(t, 0)$. In this section, we extend our analysis beyond $g^{(2)}$ by determining the amount of quantum coherence of the emission. As discussed in the preceding chapter, quantum superpositions are always defined with respect to a meaningful reference frame and degrade under the influence of external phase noise. In the interferometric scenario, which can be seen as the ideal case, however, the quantum coherence of a displaced thermal state depends solely on the coherent and thermal photon numbers. Since both photon numbers are encoded in the photon statistics, the maximal attainable quantum coherence can be inferred from phase-averaged measurements. Such an approach is

essential, as the short coherence time of the polariton condensate - ranging from several picoseconds to a few nanoseconds [47, 123] - precludes a long-term stable phase relationship to a local oscillator and, consequently, the use of conventional quantum state tomography. Although single-photon detectors could be employed to measure the photon statistics of the emission, and even the quantities $\langle \hat{n} \rangle$ and $g^{(2)}(0)$ would suffice to estimate the coherent and thermal contributions of the field, we instead extract both photon numbers from the phase-averaged Husimi-Q distribution. This method offers several advantages over the aforementioned alternatives. First, the mode sensitivity of homodyne detection allows us to examine multimode signals mode-selectively without applying additional spectral filters. Second, the positivity and smoothness of the Husimi-Q distribution enable reliable parameter extraction even for weak light fields with photon numbers close to zero. The latter poses a particular challenge for the approach based on $g^{(2)}(0)$, which destabilizes numerically for light fields in the vicinity of the vacuum state. A necessary condition for applying the displaced thermal state model to the constructed Husimi-Q distribution is that the polariton system remains in a stationary state throughout the recording time. As noted in the previous section, this condition is not fulfilled for excitation powers near the condensation threshold. We therefore filter the quadratures based on their associated photon numbers, again using a threshold intensity of 0.6 photons per pulse. A transfer of the Husimi-Q distribution into the phase-space spanned by α, followed by a coordinate transformation into polar coordinates, allows us to perform a fit to the radial profile of the phase-averaged distribution using the Husimi-Q distribution for a phase-averaged displaced thermal state [77]

$$Q_{\mathrm{DT,Inc}}(\alpha) = \frac{\exp\left[-\left(|\alpha|^2 + |\alpha_0|^2\right) / \left(n_{\mathrm{th}} + 1\right)\right]}{\pi(n_{\mathrm{th}} + 1)} I_0\left(\frac{2|\alpha||\alpha_0|}{n_{\mathrm{th}} + 1}\right) . \tag{7.1}$$

In this fitting procedure, the parameters $|\alpha_0|^2$ and n_{th} correspond to the coherent and thermal photon numbers of the light field, while I_0 denotes the zeroth-order modified Bessel function of the first kind. Due to the rotational symmetry of the distribution, the function depends solely on the radial coordinate. This allows us to utilize the entire constructed phase-space distribution, thereby enabling meaningful parameter estimation even from a limited number of quadratures. We will make use of this advantage in the final section.

The results of the Husimi-Q construction and the subsequent analysis are presented in figure 7.4. The heatmaps in the panels (a-d) of the top row illustrate the evolution of the Husimi-Q distribution as the system is driven across the condensation threshold. The panels in the bottom row show the excitation-power dependency of the coherent and thermal photon numbers (e), as well as the corresponding dependencies of $g^{(2)}(0)$ (f) and $\mathcal{C}$ (g). For the latter, we employed the equations (2.46) and (6.4). The Husimi-Q distributions illustrate how the polariton system evolves from an incoherent

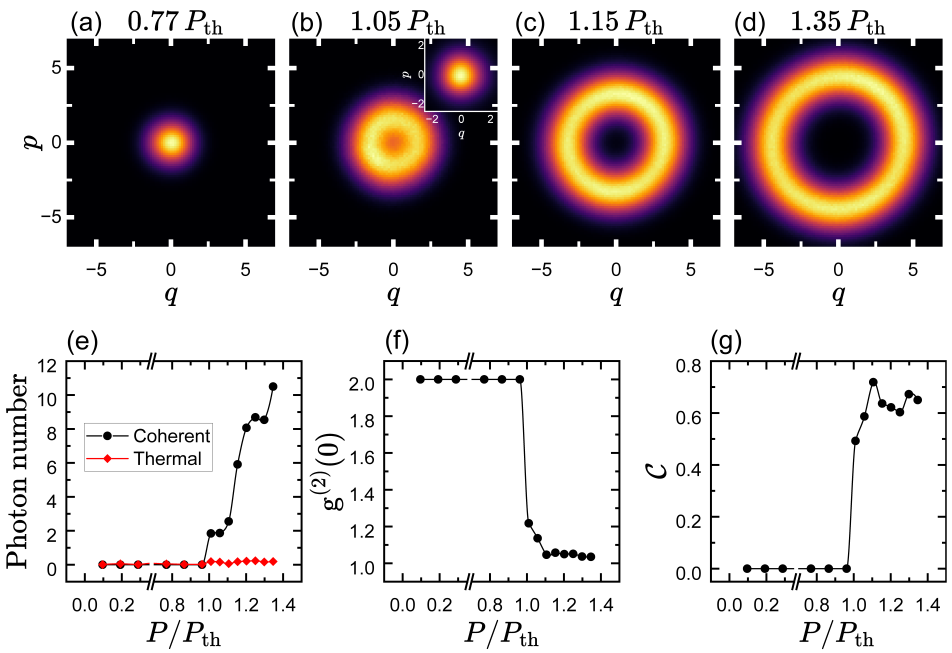

Figure 7.4: Compilation of the principal results obtained from the reconstruction of the phase-averaged Husimi-Q distributions of the polariton condensate. The upper panels (a)-(d) display the phase-averaged Husimi-Q distributions for representative excitation powers of $0.77\,P_{\mathrm{th}}$, $1.05\,P_{\mathrm{th}}$, $1.15\,P_{\mathrm{th}}$, and $1.35\,P_{\mathrm{th}}$. The distribution in panel (a) corresponds to the vacuum state, since the local oscillator does not overlap with the uncondensed polaritons. Meanwhile, the main image in panel (b) displays the condensate state reconstructed exclusively from time intervals in which condensation occurred, whereas the inset shows the average distribution obtained from the complete recorded dataset. In panels (c) and (d), the system remains continuously in the condensed state. The bottom row represents the results derived from these distributions within the displaced thermal state model. Panel (e) shows the excitation power dependence of the coherent and thermal photon numbers extracted from the fit. The corresponding dependencies of $g^{(2)}(0)$ and $\mathcal{C}$, calculated from these parameters, are displayed in the panels (f) and (g), respectively. Adapted from [63].

mixed state without quantum superpositions to a state of higher purity that exhibits pronounced coherence as the system is driven over the condensation threshold. Below threshold, depicted in panel (a), the system consists of an incoherent polariton population, represented in the reconstruction by a vacuum state as the local oscillator does not overlap spectrally with the ground state mode. This situation changes once the system is driven above the threshold, as shown in panel (b). As soon as a condensate forms, coherent contributions become visible as the phase averaged

phase-space distribution reshapes from a Gaussian distribution to a ring of finite ring radius. The inset in panel (b) shows the distribution reconstructed from the complete dataset, including time intervals without condensation. As expected, the dominant vacuum component nearly completely obscures the coherent contribution in this case. At higher excitation powers, displayed in panels (c) and (d), the system stabilizes, and the coherent photon number increases, indicated by the growing ring diameter of the phase-space distribution. In contrast, the width of the ring remains comparable to the width of the vacuum state, implying that the thermal photon number remains close to zero.

Building on the preceding qualitative discussion of the Husimi-Q distributions, we quantify our observations using the displaced thermal state model. We find that the coherent photon number increases from zero once the excitation power exceeds the threshold power. In contrast, the thermal photon number rises only slightly and remains at a level of around 0.2 photons even for higher excitation powers. This behavior also translates to $g^{(2)}(0)$. In accordance with previous studies [124, 125, 126], we assign the uncondensed polaritons below threshold a thermal distribution with $g^{(2)}(0) = 2$. As the excitation power surpasses the threshold, $g^{(2)}(0)$ decreases immediately to 1.4 and subsequently converges towards unity with increasing pump power. At last, we examine the evolution of the quantum coherence $\mathcal{C}$. As expected, no quantum coherence is observed below the threshold, which is consistent with the expectations for both a vacuum and a thermal state. Once the system is driven over the threshold, quantum coherence increases rapidly to approximately 0.5, indicating the fast formation of quantum superpositions. For higher excitation powers, $\mathcal{C}$ increases further, attaining a maximal value of 0.7 before exhibiting fluctuations at around 0.65. We attribute these fluctuations to minor variations in the fitting procedure, as the quantum coherence becomes increasingly sensitive to small changes in the thermal photon number at high coherence values.

Finally, we compare our results on the quantum coherence with previous measurements reported by Lüders et al. [77]. In their study, the same coherence quantifier was employed; however, the authors investigated a microcavity with a lower quality factor and excited the sample with a Gaussian beam of 70 µm diameter. It is important to note that a direct comparison of the estimated absolute quantum coherences is not meaningful. This follows as our quantifier depends on the absolute coherent and thermal photon numbers, such that a difference in emission intensity lead to a different quantum coherence. This effect becomes understandable when considering that a change in intensity can be modeled by a beam splitter operation, which is a non-free operation in the context of quantum coherence and therefore may change the quantum coherence [127, 128]. Nonetheless, we can still meaningfully compare the qualitative evolution of quantum coherence as the system is driven across the condensation threshold. In the measurements by Lüders et al., several multiples

of the threshold power were required to reach maximal quantum coherence. In contrast, our results demonstrate the emergence of substantial quantum coherence immediately above the condensation threshold. This observation is particularly notable given that the blueshift observed in our study exceeds the one reported previously, affirming our claim that not the mere presence of a reservoir suppresses quantum coherence. Rather, fluctuations within the reservoir appear to be the dominant source of thermally induced decoherence. Consequently, it may be sufficient to spatially separate the condensate from fluctuating reservoir particles, such as free electrons and holes, while interactions with comparatively static particles - such as dark excitons - play only a secondary role.

7.4 Husimi-Q Analysis of Fluctuating Light Fields

In the previous section, we observed how the condensation process of the polariton population leads to the formation of coherent quantum superpositions, as reflected in the buildup of quantum coherence in the emitted light field. A necessary condition for this analysis, however, was that the condensate remained in a stationary state throughout the recording time. In this final section, we relax this restriction and examine the average quantum coherence measured when the light field varies over the acquisition time. Furthermore, we compare the coherence value measurable with quantum state tomography with that estimated from phase-averaged detection and the displaced thermal state model. This comparison allows us to determine under which conditions - and for which quantifier - the model provides a valid approximation, and where its limitations become significant. Finally, we complement the simulations by introducing a time-resolved version of the Husimi-Q analysis. This approach enables us to probe the instantaneous coherence properties of the light field, eliminating the influence of external intensity noise.

7.4.1 Application of the Displaced Thermal State Model to Fluctuating Light Fields

We begin our analysis by examining how intensity noise affects the coherence properties of the time-averaged state. In this regard, the experimental results obtained in the previous two sections motivate us to several assumptions streamlining the simulations. First, we observe that the coherence properties of the state become more sensitive to thermal noise when the unperturbed state is highly coherent. For this reason, we limit our analyses to coherent states as they promise the most significant changes in the coherence properties. Second, the time traces of $\langle \hat{n} \rangle(t)$, displayed in figure 7.3, indicate that the photon fluctuations created by external

noise are often nearly harmonic. This motivates us to model the time dependent photon number $\langle\hat{n}\rangle(t)$ via

$$\langle\hat{n}\rangle(t) = n_0 + \delta n \sin(\omega t)\,, \tag{7.2}$$

where n_0 denotes the time-averaged photon number, δn is the modulation amplitude, and ω is the modulation frequency. To obtain average values one would expect for a long measurement over many oscillation cycles, we average the quantum state over one cycle period. Finally, the time traces of $\langle\hat{n}\rangle(t)$ in figure 7.3 further indicate that the fluctuation amplitude usually increases with increasing average photon number. To consider this effect during the analysis, we investigate the coherence properties as functions of the relative amplitude $\frac{\delta n}{n_0}$, normalized to the respective average photon number.

The simulations then follow the following pattern: First, we construct the instantaneous density matrices corresponding to the sinusoidally modulated photon number. To this end, we discretize the modulation in 200 steps. The density matrix of the averaged state corresponds then to the average over all instantaneous density matrices. Finally, we use the intensity-averaged density matrix to calculate the reference value of the quantum coherence. Afterward, we construct the phase-averaged Husimi-Q distribution phase-averaged intensity-averaged density matrix, which lack all off-diagonal matrix elements. By fitting the radial profile of this distribution within the displaced thermal state model, we extract the effective coherent and thermal photon numbers of the intensity-averaged state. Meanwhile, fit quality indicates whether the model provides a valid description.

We begin our studies by analyzing the effect of intensity modulation on the density matrix and the phase-averaged Husimi-Q distribution. For this purpose, figure 7.5 illustrates both quantities for a coherent state with $n_0 = 10$ and δn of 0, 0.5, 3, and 7 photons. The top row shows the corresponding intensity-averaged density matrices. The bottom row presents the profiles of the phase-averaged Husimi-Q distributions evaluated at $\mathrm{Im}(\alpha = 0)$ (black lines), together with fits based on the displaced thermal state model (dashed red lines). Examining the evolution of the density matrices first, we observe that the distribution elongates along the main diagonal as the modulation amplitude increases. Meanwhile, its shape transforms from a rounded triangle at $\delta n = 0$ to a conical structure at $\delta n = 7$. The conical profile arises since the distribution of the coherent state broadens with increasing photon number along the anti-diagonal axis. This behavior highlights a fundamental difference between the effects of intensity noise and thermal noise. Thermal noise reshapes the distribution of density matrix elements into an elliptical form, whereas intensity modulation leads to a markedly different structural change. Meanwhile, the profiles of the phase-averaged Husimi-Q distributions in the bottom row of figure 7.5

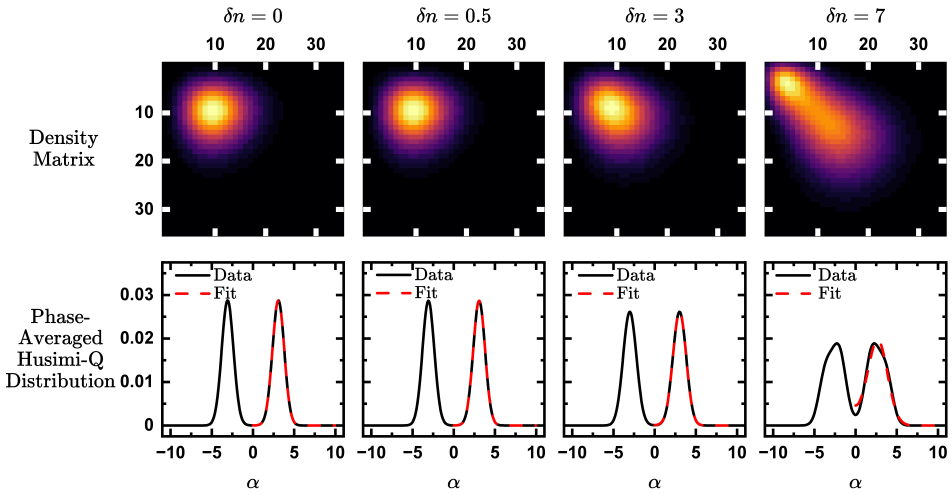

Figure 7.5: Simulated results of a time-averaged coherent state with modulated photon number. The mean photon number over one time period is fixed at $n_0 = 10$, while the instantaneous photon number undergoes sinusoidal modulation. Simulations are carried out for different modulation amplitudes δn of 0, 0.5, 3, and 7. The top row shows the corresponding density matrices of the averaged states, while the bottom row presents profiles at $\mathrm{Im}(\alpha) = 0$ of the experimentally obtainable phase-averaged Husimi-Q distributions (black lines), together with corresponding fits based on the displaced thermal state model (red dashed lines).

only reflect changes in the photon-number statistics. As the modulation amplitude increases from $\delta n = 0$ to $\delta n = 3$, we observe a broadening of the distribution accompanied by a reduction in peak height. These changes are, however, less pronounced compared to the structural changes observed in the corresponding density matrices. The difference between both representations becomes apparent when comparing the density matrix and the Husimi-Q distribution for $\delta n = 3$. Although the model still provides an adequate fit to the Husimi-Q distribution, the density matrix already differs significantly from that of a displaced thermal state. In contrast, the fit model only breaks for very large modulation amplitudes, such as $\delta n = 7$. This observation leads to our first key finding: intensity modulation alters the off-diagonal elements of the density matrix more strongly than the photon statistics encoded in the main diagonal. Consequently, it becomes essential to quantify how coherence predicted by the displaced thermal state model deviates from the correct values and under which conditions the model may still yield reliable approximations.

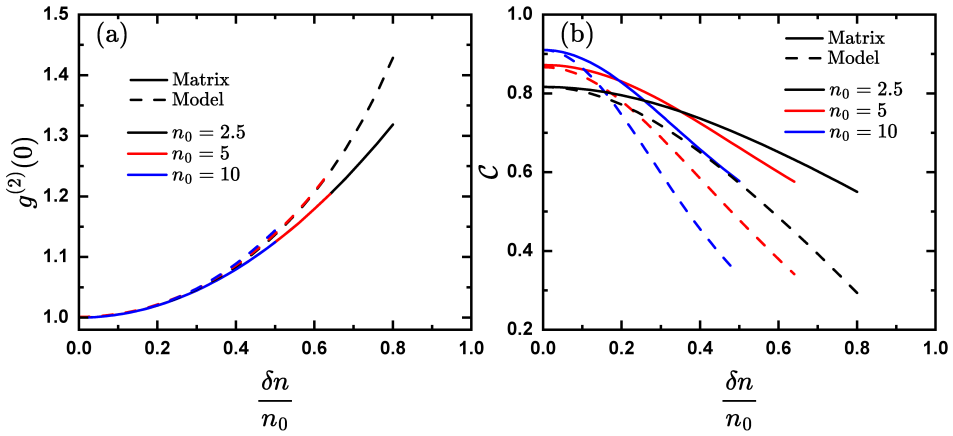

Figure 7.6: Second order correlation function $g^{(2)}(0)$ (a) and quantum coherence $\mathcal{C}$ (b) of an averaged coherent state of sinusoidally modulated photon number, dependent on the relative modulation amplitude $\frac{\delta n}{n_0}$. The simulations are performed for different average photon numbers n_0 of 2, 5, and 10. The full line plots display the results obtained from the averaged density matrices, while the dashed lines show the evolution predicted by the displaced thermal state model applied to the phase averaged Husimi Q distribution. We consider a fit successful if the sum of least squares is below 10^{-5}.

To investigate this question further, we examine the second-order correlation function $g^{(2)}(0)$ and the quantum coherence $\mathcal{C}$ as functions of the relative modulation amplitude $\frac{\delta n}{n_0}$. The associated curves are displayed in the panels (a) and (b) of figure 7.6 for n_0 of 2.5, 5, and 10. To restrict the analysis to states whose photon statistics follow the displaced thermal state model, we include only those states for which the sum of least squares of the fitting procedure remains below 10^{-5}. For $g^{(2)}(0)$, we observe generally good agreement between the reference curves and the model predictions. In the small perturbation regime below $\frac{\delta n}{n_0} = 0.2$ - as typically encountered in stabilized systems - deviations are negligible. Significant discrepancies arise only for large modulations. Notably, the observed relationships are independent of the absolute average photon number, indicating that $g^{(2)}(0)$ is a normalized quantity. In contrast, quantum coherence depends on both the absolute photon number and the absolute modulation amplitude, leading to a clear splitting of the curves. Consistent with the observations made for the density matrices, the quantum coherence predicted by the model deviates even for minor modulation amplitudes noticeably from the reference curve, whereby the deviations become more pronounced with increasing n_0. Conversely, the range of modulation amplitudes with acceptable deviations further narrows with increasing n_0. Consequently, caution is required when applying the displaced thermal state model to Husimi-Q distributions

constructed from experimental signals with fluctuating intensity. While the associated error may remain acceptable for $g^{(2)}(0)$, it becomes crucial when evaluating $\mathcal{C}$. Nevertheless, in such situations, the value obtained from the model may still provide a conservative lower-bound estimate for the true quantum coherence.

7.4.2 Time-Resolved Husimi-Q Analysis

After examining the influence of intensity noise on the quantum coherence obtained from time-averaged measurements, we now introduce a time-resolved version of the Husimi-Q analysis that enables the reconstruction of the instantaneous quantum coherence. The underlying principle is analogous to that of the time-resolved evaluation of $\langle\hat{n}\rangle$ and $g^{(2)}(0)$, described in section 4.3.3. Using a rolling window, the set of orthogonal quadrature pairs is distributed into subsets, each corresponding to a certain time interval. From each subset, we construct the Husimi-Q distribution and subsequently fit it according to the displaced thermal state model. This gives us access to the time traces of the coherent and the thermal photon number of the examined light field. To benchmark the method, we apply it to a temporally unstable signal recorded from a polariton condensate near the condensation threshold that was subject to external mechanical perturbations. The window size is set to 10000 quadrature pairs per point and the step size of the rolling window is set to 1000 quadratures. Further, the (q, p)-phase space has a binning resolution of 0.2.

The corresponding results are presented in figure 7.7. The time evolutions of the coherent and thermal photon numbers $|\alpha|^2(t)$ and $n_{\mathrm{th}}(t)$, the second-order correlation function $g^{(2)}(t, 0)$, and the quantum coherence $\mathcal{C}(t)$ are displayed in panels (a-c). In addition, the top row illustrates the temporal evolution of the phase-averaged Husimi-Q distribution over half an oscillation cycle. When examining the time evolutions of $|\alpha|^2(t)$ and $n_{\mathrm{th}}(t)$, we observe that only $|\alpha|^2(t)$ exhibits temporal oscillations, whereas $n_{\mathrm{th}}(t)$ remains at a value of approximately 1. The Husimi-Q distribution in the top row reflects these dynamics, as the observed ring-like distribution expands and contracts with increasing and decreasing coherent photon number. We note that both curves are well-resolved and exhibit only minor fluctuations, despite the limited number of used quadratures. In the next step, we consider the time evolution of $g^{(2)}(t, 0)$. We observe a local maximum whenever the instantaneous coherent photon number reaches a minimum and vice versa. This occurs because the modulation of $|\alpha|^2(t)$ translates into a modulation of the coherent-to-thermal ratio R, which in turn modulates $g^{(2)}(t, 0)$. As for $|\alpha|^2(t)$ and $n_{\mathrm{th}}(t)$, the curve is sufficiently smooth to recognize the modulation. In the last step, we consider the quantum coherence $\mathcal{C}(t)$, which exhibits oscillations in a range between 0.23 and 0.3. This is explained by two reasons. First, the nearly constant thermal

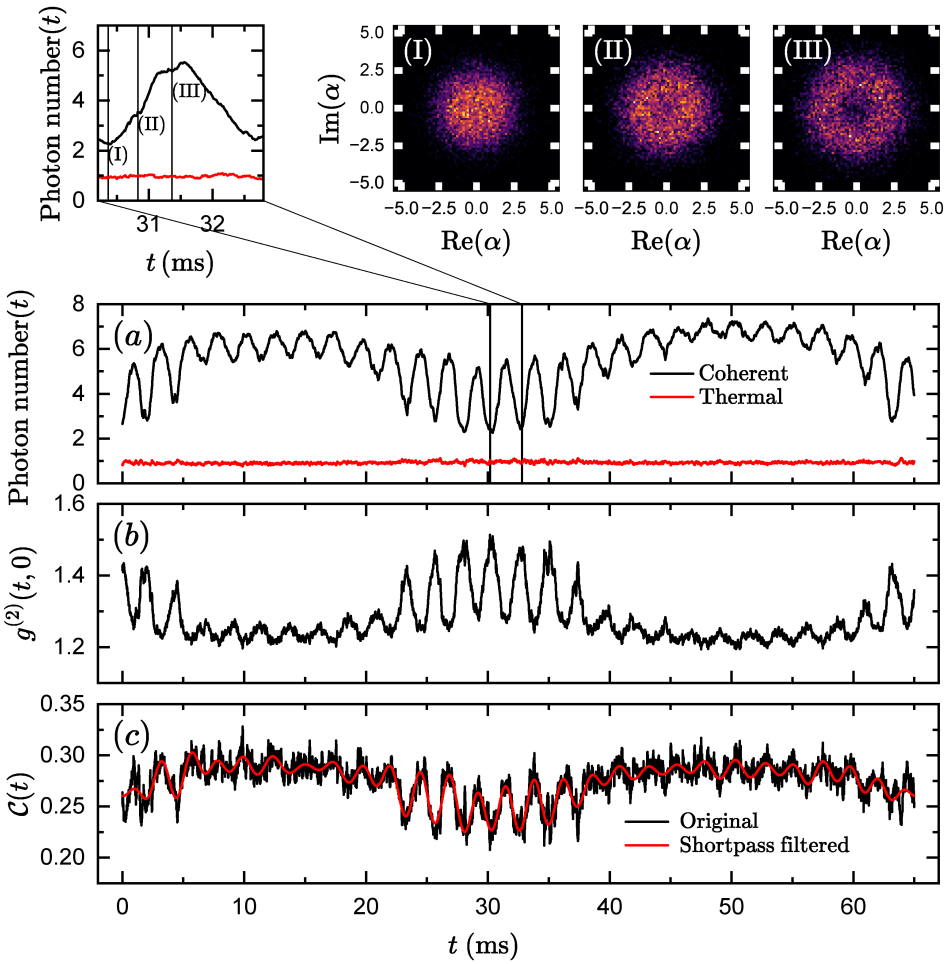

Figure 7.7: Time evolution of the principal properties of a temporally unstable polariton condensate near the condensation threshold that is subject to external noise. Panel (a) shows the coherent and thermal photon numbers $|\alpha|^2(t)$ and $n_{\mathrm{th}}(t)$, while the inset in the top row focuses on the changes of the Husimi-Q distribution over a half-period cycle. Panel (b) displays the attributed $g^{(2)}(t,0)$ and panel (c) presents the quantum coherence $\mathcal{C}(t)$. For clarity, the latter also includes a low-pass filtered version obtained using a cutoff frequency of 500 Hz.

contribution upper limit the achievable quantum coherence to around 0.35. Second the modulation of $|\alpha|^2(t)$ leads to contrary oscillations in $\mathcal{C}$ and $\mathcal{P}_{\mathrm{Inc}}$. For this reason, $\mathcal{C}(t)$ exhibits the same temporal modulation as $|\alpha|^2(t)$ and $g^{(2)}(t,0)$. Since $\mathcal{C}(t)$ is far more sensitive to minimal variations in $n_{\mathrm{th}}(t)$ than $g^{(2)}(t,0)$ the curve is, however, noisy. As a result, only oscillations of large amplitude remain visible, while oscillations of lesser amplitude vanish within the noise. This obstacle, however, can

be partially compensated for by applying a low-pass filter to the calculated time trace.

7.5 Conclusion

In conclusion, our experiments reveal a smoother condensation process and a more rapid buildup of quantum superpositions compared to previous studies. Time-resolved analysis demonstrates that, although the system is sensitive to external perturbations just above the condensation threshold, it stabilizes quickly with increasing excitation power. In particular, stabilization is achieved already at an excitation power of $1.35P_{\mathrm{th}}$, where $g^{(2)}(t,0)$ approaches unity. We attribute the rapid formation of quantum superpositions to two primary factors. First, the extended polariton lifetime allows the polaritons to propagate over macroscopic distances while thermalizing without significant loss of coherence. Second, the spatial separation of the condensate from the reservoir minimizes interactions with strongly fluctuating reservoir particles. In this context, the use of traps with larger diameters may further improve coherence. Notably, our analysis indicates that the mere overlap with the reservoir does not necessarily degrade coherence; rather, the interactions with fluctuating particles limit the attainable quantum coherence. The extension from stationary states to intensity-modulated states, however, demonstrates that one has to be careful when applying the displaced thermal state model. Although the model appears to remain valid even for moderately large modulation amplitudes, the off-diagonal density matrix elements deviate rapidly from the model. As a result, discrepancies between model predictions and the true value emerge even for relatively small modulations. In such cases, however, the model-based estimate may still provide an experimentally accessible lower bound. Finally, we have shown that time-resolved Husimi-Q distribution analysis can bridge this gap, offering deeper insights into the temporal evolution of the coherence properties of a light field that is influenced by external mechanical noise. These findings may facilitate the integration of polariton condensates as low-threshold sources of resourceful quantum states in future hybrid quantum devices.

8 Conditional Spectroscopy Through Non-Stationary Optical Tomography on a Sixteen-Port Homodyne Detector

Over the past decades, continuous variable quantum state tomography based on homodyne detection has evolved into a powerful technique for extracting comprehensive information about a given light field. A major limitation of conventional optical tomography employing a four-port homodyne detector, however, is the requirement for a fixed phase relationship between the signal and the local oscillator. While this condition can often be satisfied in controlled environments, as usually found in quantum-optical experiments such as the experimental validation of the displaced thermal state model discussed in chapter 6, it restricts the applicability in other areas, such as semiconductor spectroscopy. In this context, the primary objective is typically not the characterization of the emission state itself, but of the underlying semiconductor dynamics, which can be investigated through the emission. These dynamics typically take place on picosecond timescales or below, while the optical phase may fluctuate on comparable timescales. As a result, conventional stationary optical tomography can only reconstruct the phase-averaged time-averaged quantum state, even though the intrinsic temporal resolution of homodyne detection would, in principle, be sufficient to resolve the dynamics. One strategy to overcome this limitation is to use an extended homodyne detection scheme with 12 ports [129]. In this approach, the signal of interest is split at a beam splitter into two detection channels, hereafter referred to as the postselection (ps) and target (t) channels. The light field in the postselection channel is measured using an eight-port detector that samples the Husimi-Q distribution. Simultaneously, a four-port detector in the target channel samples the Wigner distribution. Because the fields in both channels share a fixed relative phase, the phase information recorded in the postselection channel can serve as a phase reference for the target channel. This enables reconstruction of the phase information - and consequently paves the way to compute the density matrix - in the target channel, even in the absence of a fixed phase relationship with the local oscillator. This ability, however, comes at the cost of additional noise, as additional vacuum enters through the initial beam splitter into the two channels. The system can be extended to non-stationary optical homodyne tomography with sub-picosecond time resolution by introducing a controlled time delay τ between the

two channels. The twelve-port detection scheme resembles, in this regard, previous non-stationary techniques, but is not limited to the detection of the time-resolved $g^{(2)}$ or the time-resolved photon statistics [130, 59]. A second application, especially interesting for semiconductor spectroscopy, is conditional analysis. In this scenario, one is not interested in the complete signal per se but in specific events that occur according to stochastic dynamics. Accordingly, one does not assume, in contrast to quantum optics, that the system is in a pure state, but rather that averaging over the underlying dynamics leads to a mixed state. This includes phenomena such as the spontaneous condensation of a polariton population [131] or the blinking of quantum dots [132]. In such cases, ensemble averaging over identically prepared systems is insufficient and one needs to employ triggered or conditional techniques to reveal the dynamics.

A typical twelve-port measurement proceeds as follows: The eight-port detector in the postselection channel samples a pair of orthogonal quadratures from the Husimi-Q distribution of a given light field at an arbitrary time t_0, thereby returning some information about the system. Simultaneously, the four-port detector in the target channel samples a quadrature of the light field at time $t_0 + \tau$. Since the light fields in the two channels are typically correlated, the measured quadratures in the two channels are correlated likewise. Based on this connection, conditional analysis enables the investigation of the conditional state in the target channel that is present when the light field in the postselection channel satisfies a specified condition, for example, a particular amplitude and phase. The key advantage of this approach compared to other techniques is that the condition can be defined after the measurement, enabling different analyses based on the same data set. In practice, the conditional analysis is performed by applying the chosen condition to the indexed set of recorded orthogonal quadrature pairs and identifying the subset of indices that satisfy the condition. In the next step, the subset of data recorded in the target channel corresponding to these same indices is selected. Finally, this second subset is used to perform all subsequent calculations, such as a density-matrix reconstruction. The ability to track ultrafast dynamics on the sub-picosecond timescale, combined with the option to perform conditional analyses under flexible a posteriori-applied postselection criteria, enhances the capabilities of conditional non-stationary optical tomography compared to other techniques. The capabilities of twelve-port homodyne detection for conditional analysis have already been demonstrated in previous studies. For example, Thewes et al. [129] experimentally showed how a thermal light field may arise from an incoherent mixture of coherent states. Similarly, Lüders et al. used conditional analysis to investigate the decoherence dynamics of a polariton condensate [123].

The objective of this chapter is to extend the twelve-port detection scheme to a sixteen-port detection scheme by replacing the four-port detector in the target channel with a second eight-port detector. Although the application domains of a sixteen-port detector are largely analogous to those of a twelve-port detector, the additional eight-port detector significantly simplifies the data analysis. In particular, the phase information in the target channel no longer needs to be estimated via phase reconstruction but is directly experimentally accessible. Moreover, both unconditional and conditional states in the target channel can be analysed directly in terms of their Husimi-Q distributions, eliminating the need for density-matrix reconstruction or more elaborated tailored phase-space distributions [129, 123]. A further application that particularly benefits from a sixteen-port configuration is the simultaneous measurement of two modes. By applying appropriate filters to each channel, one can configure the sixteen-port detector to simultaneously measure the Husimi-Q distributions of the individual modes. This approach can then be combined with conditional or non-stationary optical tomography to investigate the correlation dynamics between the two modes.

The remainder of this chapter is organized into four sections. In section 8.1, we introduce the experimental configuration of the sixteen-port detector, describe the alignment scheme, and consider further extensions of the setup to perform experiments on two-mode light fields. The subsequent three sections then focus on benchmarking the sixteen-port detector using a thermal light field. We begin in section 8.2 by first deriving theoretical reference values for a couple of properties of the conditional state in the target channel for a fixed amplitude and phase in the postselection channel. Afterward, we use these reference values to benchmark the experimental setup at zero time delay. In section 8.3, we extend the analysis to non-stationary optical tomography and examine the decoherence dynamics of the conditional state based on several observables. Finally, in section 8.4, we conclude the chapter by analyzing how the amplitude and phase information between both channels degrade with increasing time delay. To this end, we investigate the distributions of amplitude and phase differences between the two channels.

8.1 Construction and Alignment of a Sixteen-Port Detector

Throughout the previous section, we have implicitly defined a number of requirements for the design of a sixteen-port detector. An experimental setup that fulfills these requirements is schematically illustrated in figure 8.1. A non-polarizing beam splitter distributes the signal light field (blue) equally between the postselection and the target channel. Each channel is equipped with an eight-port detector, as introduced in section 4.2.2, which samples pairs of mutually orthogonal quadratures from the

corresponding Husimi-Q distributions. The local oscillator (red) is distributed analogously, whereby additional delay lines in the local oscillator beam paths enable precise control of the temporal delay between the two channels. To fine-tune the spatial overlap between the local oscillator and the signal in each channel, a small fraction of the local oscillator is split off and used as a test-signal. This concept is analog to the experiments in the previous chapters, however, we employ free-space beam propagation instead of optical fibers to minimize optical losses. The subsequent preprocessing and digitalization of the recorded electric signals is analogous to that of a four-port detector, with the only difference that we employ two synchronized ADC cards to maintain a sampling rate of 2.5 GHz per balance detector. The main disadvantage of beams propagating in free space is that the beam paths and beam diameters of the signal and the test-signal must be matched manually. For this purpose, additional telescopes with embedded pinholes are inserted into the beam paths of each channel. The focal distances of the telescope's lenses and the diameters of the pinholes are chosen with respect to the signal beam's diameter, ensuring that the signal just passes through the pinhole. The test-signal, in contrast, is adjusted to have a slightly smaller diameter before entering the telescope. As a result, it becomes slightly larger than the pinhole diameter, allowing the pinhole to reshape the test-signal to the diameter of the signal. Optimal coupling of the test-signal through the pinhole is achieved by adjusting the beam path with the two steering mirrors in the test-signal path. Following this procedure, the signal and the test-signal should have the same diameter and propagate along the same optical path. The remaining alignment steps are identical to those for an individual eight-port detector, as described in section 4.2.2.

The described setup design can be extended to various types of two-mode configurations without requiring substantial modifications. In particular, it enables the simultaneous measurement of two modes that show different polarization, energy, or spatial modes. To measure two modes of different polarization, additional polarization filters can be introduced into the signal beam paths. In the case of two spectrally separated modes that are still sufficiently close to overlap with the local oscillator, additional spectral filters may be implemented in both signal beam paths to enable selective detection of the respective modes. Finally, one can employ the telescopes to filter for spatially separated modes. In this case, the size of the test-signal must be chosen such that it overlaps with both signal modes at the pinhole.

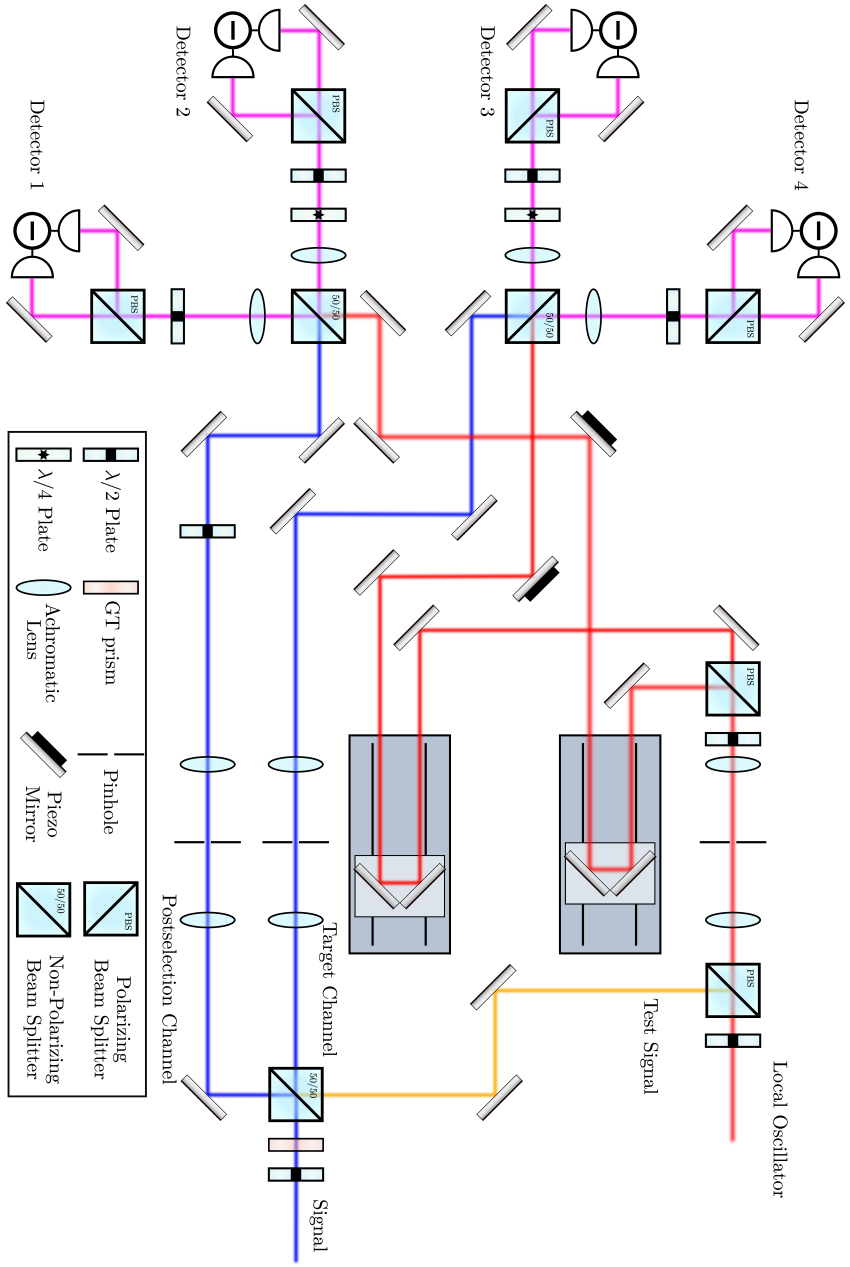

Figure 8.1: Schematic illustration of the sixteen-port homodyne detection setup. Sources of the local oscillator and the signal, as well as the electronics used for recording, are omitted for clarity. A description of the setup, a brief alignment scheme, and a brief summary of the necessary modifications to turn the setup into a two-mode detector are given in the text.

8.2 Benchmark of the Sixteen-Port Detector with a Thermal State

After outlining the fundamental layout of a sixteen-port detector and presenting a straightforward alignment procedure, we proceed to benchmark the detector performance. Thermal light fields are ideal candidates for this purpose, as they can be generated in a stable, reproducible manner on the one hand, but require high temporal resolution and conditional analysis to examine the ultrafast stochastic processes that govern the emission process on the other hand. Moreover, their comparatively simple theoretical description in phase space enables us to calculate theoretical reference values for a series of relevant physical quantities. To benchmark the sixteen-port detector, we consider the simplest postselection condition and investigate the conditional state in the target channel for a fixed γ_{ps} in the postselection channel corresponding to a fixed amplitude and a fixed phase. The benchmark consists of two steps: First, we derive the theoretically expected conditional Husimi-Q distribution in the target channel $Q_{\mathrm{c}}(\delta)$ and compute the conditional expectation values $\langle \hat{O} \rangle_{\mathrm{c}}(\gamma_{\mathrm{ps}})$ for several observables. Afterward, we examine the experimentally found conditional Husimi-Q distribution at zero time delay and compare the results. This benchmarking procedure follows the procedure introduced by Thewes et al. [129] to benchmark the twelve-port detector.

8.2.1 The Conditional Husimi-Q Distribution of a Thermal State

We begin the theoretical analysis by deriving an analytical expression for the conditional Husimi-Q distribution in the target channel $Q_{\mathrm{c}}(\delta)$. To clearly distinguish between the different Husimi-Q distributions, we denote the unconditional distributions in the postselection and the target channels by $Q_{\mathrm{ps}}(\gamma)$ and $Q_{\mathrm{t}}(\delta)$. We begin with the joint P distribution of the thermal and the vacuum state that enter the initial beam splitter, which splits the signal into the postselection and the target channel. The states at the beam splitter's inputs and outputs are named according to section 4.1.1. Since the two states are uncorrelated, the joint input P distribution is given by the product of the P distributions of the individual states $P_{\mathrm{j}}(\alpha, \beta) = P_{\mathrm{vac}}(\beta) P_{\mathrm{th}}(\alpha)$. In practice, however, we are not measuring the P distribution but the Q distribution. For this reason, we calculate the associated

joint Husimi-Q distribution $P_\mathrm{j}(\alpha,\beta)$, which is, according to (2.30), given by

$$\begin{aligned} Q_\mathrm{j}(\alpha,\beta) &= \frac{1}{\pi^2}\int_{-\infty}^{\infty}\mathrm{d}^2\alpha'\int_{-\infty}^{\infty}\mathrm{d}^2\beta'\,P_\mathrm{th}(\alpha')P_\mathrm{vac}(\beta')\mathrm{e}^{-|\alpha-\alpha'|^2}\mathrm{e}^{-|\beta-\beta'|^2} \\ &= \left[\frac{1}{\pi}\int_{-\infty}^{\infty}\mathrm{d}^2\alpha'\,P_\mathrm{th}(\alpha')\mathrm{e}^{-|\alpha-\alpha'|^2}\right]\left[\frac{1}{\pi}\int_{-\infty}^{\infty}\mathrm{d}^2\beta' P_\mathrm{vac}(\beta')\mathrm{e}^{-|\beta-\beta'|^2}\right] \\ &= Q_\mathrm{th}(\alpha)Q_\mathrm{vac}(\beta) \end{aligned} \tag{8.1}$$

Because P_th and P_vac are uncorrelated, the double integral factorizes into a product of single-mode integrals over the respective phase spaces. As these integrals correspond to the relation between the P and Q distributions of a single-mode light field, the equation simplifies to $Q_\mathrm{j}(\alpha,\beta) = Q_\mathrm{th}(\alpha)Q_\mathrm{vac}(\beta)$. Consequently, by inserting the known Husimi-Q distributions of the vacuum and thermal state [11, p. 326, p. 328], we obtain

$$Q(\alpha,\beta) = \frac{\exp(-|\beta|^2)}{\pi^2(1+n_\mathrm{th})}\exp\left(-\frac{|\alpha|^2}{1+n_\mathrm{th}}\right), \tag{8.2}$$

where n_th denotes the average photon number of the thermal light field. In the next step, we use the beam splitter transformation introduced in equation 4.5 to acquire the Husimi-Q distribution of the joined output state behind the beam splitter. To keep the computation simple, we assume a lossless beam splitter and real reflection and transmission coefficients, leading to $t_1 = t_2 = t$ and $r = r_1 = -r_2$. With these assumptions, we receive

$$Q(\gamma,\delta) = \frac{\exp(-|t\gamma + r\delta|^2)}{\pi^2(1+n_\mathrm{th})}\exp\left(-\frac{|t\delta - r\gamma|^2}{1+n_\mathrm{th}}\right). \tag{8.3}$$

Finally, we transition from the unconditional Husimi-Q distribution of the joined output state to the conditional Husimi-Q distribution in the target channel by replacing the phase space variable γ by the postselected constant γ_ps. After a final renormalization, performed with Wolfram Mathematica, we obtain

$$Q_\mathrm{c}(\delta) = \frac{\exp\left(\frac{|\gamma_\mathrm{ps}|^2}{1+n_\mathrm{ps}}\right)}{2\pi(1+n_\mathrm{th})}\cdot\exp(-|t\gamma_\mathrm{ps} + r\delta|)\cdot\exp\left(\frac{|t\delta - r\gamma_\mathrm{ps}|^2}{1+n_\mathrm{th}}\right), \tag{8.4}$$

where $n_\mathrm{ps} = r^2 n_\mathrm{th}$ and $n_\mathrm{t} = t^2 n_\mathrm{th}$ denote the average photon numbers measured in the postselection and the target channel.

After acquiring $Q_\mathrm{c}(\delta)$, we apply the optical equivalence theorem, introduced in section 2.1.9, to calculate the expectation values of the operators $\hat{q}$, $\hat{p}$, $\hat{q}^2$, $\hat{p}^2$, and $\hat{n}$ for the conditional state. The corresponding antinormally ordered functions $O^{(a)}(\delta)$, together with the resulting analytical expressions for $\langle O\rangle_\mathrm{c}(\gamma_\mathrm{ps})$, are summarized in

$\hat{O}$	$O^{(a)}(\delta)$	$\langle\hat{O}\rangle_{\mathrm{c}}(\gamma_{\mathrm{ps}})$
$\hat{q}$	$\sqrt{2}\mathrm{Re}(\delta)$	$-\mathrm{Re}(\gamma_{\mathrm{ps}})\frac{\sqrt{2n_{\mathrm{ps}}n_{\mathrm{t}}}}{1+n_{\mathrm{ps}}}$
$\hat{p}$	$\sqrt{2}\mathrm{Im}(\delta)$	$-\mathrm{Im}(\gamma_{\mathrm{ps}})\frac{\sqrt{2n_{\mathrm{ps}}n_{\mathrm{t}}}}{1+n_{\mathrm{ps}}}$
$\hat{q}^2$	$2\left(\mathrm{Re}(\delta)\right)^2-\frac{1}{2}$	$\frac{1+\langle n\rangle(2+n_{\mathrm{ps}})+n_{\mathrm{ps}}n_{\mathrm{t}}(1+4(\mathrm{Re}(\gamma_{\mathrm{ps}}))^2)}{2(1+n_{\mathrm{ps}})^2}$
$\hat{p}^2$	$2\left(\mathrm{Im}(\delta)\right)^2-\frac{1}{2}$	$\frac{1+\langle n\rangle(2+n_{\mathrm{ps}})+n_{\mathrm{ps}}n_{\mathrm{t}}(1+4(\mathrm{Im}(\gamma_{\mathrm{ps}}))^2)}{2(1+n_{\mathrm{ps}})^2}$
$\hat{n}$	$\lvert\delta\rvert^2-1$	$\frac{n_{\mathrm{t}}+n_{\mathrm{t}}n_{\mathrm{ps}}(1+\lvert\gamma_{\mathrm{ps}}\rvert^2)}{(1+n_{\mathrm{ps}})^2}$

Table 8.1: Antinormally ordered functions $O^{(a)}(\delta)$ and expectation values of the conditional state $\langle\hat{O}\rangle_{\mathrm{c}}(\gamma_{\mathrm{ps}})$ for a range of observables. The negative sign in the expressions of $\langle\hat{q}\rangle_{\mathrm{c}}$ and $\langle\hat{p}\rangle_{\mathrm{c}}$ arises from the chosen convention for the beam-splitter reflectivities $r_2=-r_1=-r$.

table 8.1. Based upon these results, we further compute the conditional amplitude of the target state

$$A_{\mathrm{c}}=\sqrt{\frac{\langle\hat{q}\rangle_{\mathrm{c}}^2+\langle\hat{p}\rangle_{\mathrm{c}}^2}{2}}=\frac{\sqrt{n_{\mathrm{ps}}n_{\mathrm{t}}}}{1+n_{\mathrm{ps}}}|\gamma_{\mathrm{ps}}| \tag{8.5}$$

as well as the variances along $\hat{q}$ and $\hat{p}$

$$\mathrm{Var}_{\mathrm{c}}(\hat{q})=\mathrm{Var}_{\mathrm{c}}(\hat{p})=\frac{1+n_{\mathrm{th}}+n_{\mathrm{t}}}{2(1+n_{\mathrm{ps}})}\,. \tag{8.6}$$

We highlight that the variances of $\hat{q}$ and $\hat{p}$ are independent of γ_{ps}, indicating that the conditional state resembles a coherent state. The state is, however, broadened due to the additional vacuum introduced by the additional beam splitter, while the amount of broadening depends on the splitting ratio of the beam splitter. Finally, we find from the functions $O^{(a)}(\delta)$ in table 8.1 that all expectation values are connected to each other via

$$\langle\hat{n}\rangle_{\mathrm{c}}=\frac{\langle\hat{q}^2\rangle_{\mathrm{c}}+\langle\hat{p}^2\rangle_{\mathrm{c}}}{2}-\frac{1}{2}=\mathrm{Var}_{\mathrm{c}}(\hat{q})+A_{\mathrm{c}}^2-\frac{1}{2} \tag{8.7}$$

It is important to emphasize that the calculated expectation values refer explicitly to the operators $\hat{q}$ and $\hat{p}$ and do not necessarily describe intrinsic properties of the phase-space distribution of the state. Furthermore, all derived expressions are only valid for fixed values of γ_{ps}. This requirement also applies to observables such as A_{c} or $\mathrm{Var}_{\mathrm{c}}(\hat{q})$, even though their theoretical expectation values are only partially or completely independent of γ_{ps}.

8.2.2 Detector Benchmark using Conditional Optical Tomography

After deriving theoretical expectation values for a range of observables, we use them to benchmark the experimental sixteen-port detector. For this purpose, we employ the thermal emission from a superluminescent diode (SLD) with a central wavelength of 835 nm as the signal source and distribute it equally between the postselection and target channel. A spectral filter placed upstream narrows the signal's power spectrum to a rectangular profile with a spectral width of 1 nm. This spectral filtering increases the temporal phase coherence of the signal field, thereby allowing us to resolve its decoherence dynamics. The local oscillator is provided by a Mira 900-D laser system, which emits Gaussian pulses with a spectral full-width at half-maximum (FWHM) of 10 nm, corresponding to a temporal pulse duration of approximately 100 fs. For the beginning, we set the temporal delay between the two channels to zero. Before proceeding with the conditional analysis, we first examine

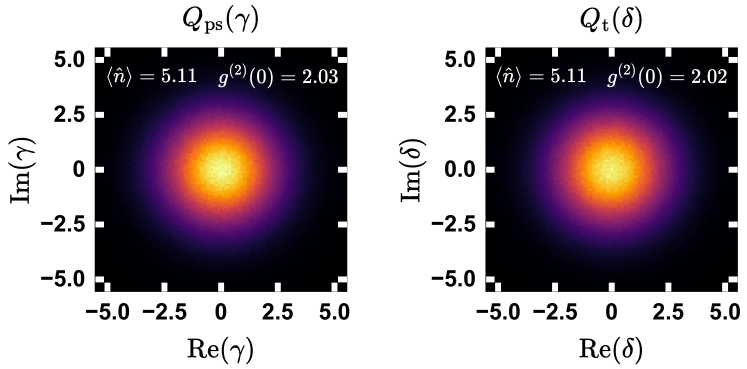

Figure 8.2: Unconditional Husimi-Q distributions Q_{ps} and Q_{t} recorded in the postselection and the target channel at zero time delay.

the unconditional states recorded in both channels. To this end, figure 8.2 shows the corresponding Husimi-Q distributions $Q_{\mathrm{ps}}(\gamma)$ and $Q_{\mathrm{t}}(\delta)$. The mean photon numbers in each channel amount to $\langle\hat{n}\rangle = 5.11$ respectively, while the measured value of $g^{(2)}(0) \approx 2$ confirms the thermal character of the light field. Following this preliminary results, we begin the conditional analysis by examining $Q_{\mathrm{c}}(\delta)$ for three different postselection conditions, whereby the corresponding distributions are illustrated in figure 8.3. The main panels display $Q_{\mathrm{c}}(\delta)$, while the insets show $Q_{\mathrm{ps}}(\gamma)$, with the postselected regions highlighted in green. In panel (a), we postselect an annular region defined by a fixed amplitude $|\gamma_{\mathrm{ps}}| = 2.5 \pm 0.125$. The resulting conditional distribution $Q_{\mathrm{c}}(\delta)$ also exhibits an annular shape. The ring diameter is, however, reduced compared to the postselected region, while the ring width is increased. In panel (b), we impose no constraint on the amplitude but restrict the phase φ_{ps}, calculated by $\varphi_{\mathrm{ps}} = \arctan\left(\mathrm{Re}(\gamma_{\mathrm{ps}}), \mathrm{Im}(\gamma_{\mathrm{ps}})\right)$ using the four-quadrant

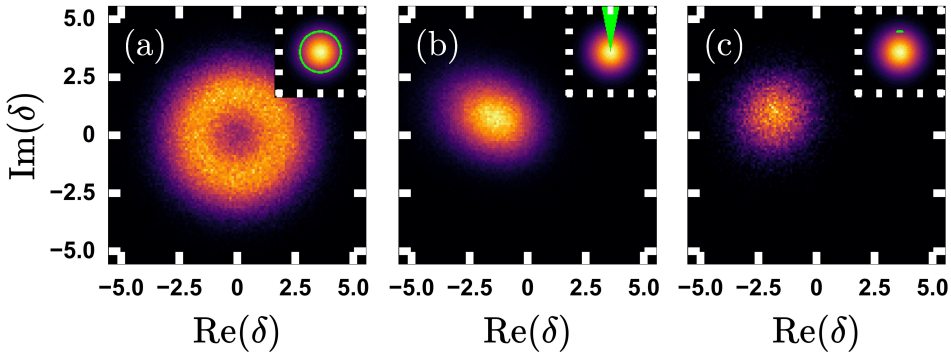

Figure 8.3: Husimi-Q distributions in the target channel for postselection areas defined by a fixed (*a*) amplitude, (*b*) a fixed phase, and (*c*) both at $\tau = 0\,\mathrm{ps}$. The Husimi-Q distributions of the postselection channel with the selected areas marked in green are shown in the insets.

inverse-tangent function, to the interval $\varphi_{\mathrm{ps}} = \frac{\pi}{2} \pm \frac{\pi}{16}$ corresponding to an area around the positive y-axis. In this case, Q_{c} acquires an elliptical Gaussian shape, elongated in the amplitude direction. Further, we note a phase shift between the postselected area in the postselection channel and the central phase of the constructed Q_{c}. This follows, as the average relative phase between both channels is random, since the spatial precision of the used delay lines of around 1 µm exceeds the wavelength of the light field. In panel (c), we combine both postselection conditions, resulting in $\gamma_{\mathrm{ps}} \approx 2.5i$. In this case, the shape of $Q_{\mathrm{c}}(\delta)$ resembles, as expected by theory, the shape of a coherent state, broadened by the additional vacuum. Experimentally, we obtain a conditional amplitude $A_{\mathrm{c}} = 2.02$, which is slightly smaller than the theoretically expected value of 2.09. The deviation can be attributed to additional phase noise between both channels, which reduces the measurable expectation values of $\langle\hat{q}\rangle_{\mathrm{c}}$ and $\langle\hat{p}\rangle_{\mathrm{c}}$. For the variances, we determine $\mathrm{Var}_{\mathrm{c}}(\hat{q}) = 1.57$ and $\mathrm{Var}_{\mathrm{c}}(\hat{p}) = 1.61$, both exceeding the theoretical value of 1.34 and additionally differing slightly from each other. The comparably large discrepancy between theory and experiment arises because $\langle\hat{q}\rangle_{\mathrm{c}}$ and $\langle\hat{p}\rangle_{\mathrm{c}}$ enter quadratically into the variance. The difference between $\mathrm{Var}_{\mathrm{c}}(\hat{q})$ and $\mathrm{Var}_{\mathrm{c}}(\hat{p})$ follows as the phase noise affects both variances differently, dependent on the distribution's position of maximal probability in phase space. In this context, $\mathrm{Var}_{\mathrm{c}}(\hat{q})$ maximizes when the position of maximal probability is located around the y-axis and minimizes when it is located around the x-axis. For $\mathrm{Var}_{\mathrm{c}}(\hat{p})$, the relation is reversed. To simplify the subsequent analyses and to reduce the variance's sensitivity to the position of maximal probability in phase space, we use from now on the averaged variance $\overline{\mathrm{Var}}_{\mathrm{c}}(\hat{q},\hat{p}) = \frac{1}{2}\left(\mathrm{Var}_{\mathrm{c}}(\hat{q}) + \mathrm{Var}_{\mathrm{c}}(\hat{p})\right)$ instead. The agreement between theory and experiment improves when considering phase-independent quantities such as $\langle\hat{n}\rangle_{\mathrm{c}}$ or

$g_c^{(2)}(0)$. For $\langle \hat{n} \rangle_c$ we obtain an experimental value of 5.19 that is in good agreement with the theoretical prediction of 5.21. The experimental value of $g_c^{(2)}(0) = 1.34$ does not reach unity, which is expected as the additional vacuum introduces additional noise into the system.

8.3 Decoherence Analysis using Non-Stationary Conditional Optical Tomography

After benchmarking the sixteen-port detector with conditional tomography at zero time delay, we extend the analysis to non-stationary conditional tomography and investigate the decoherence mechanisms of phase and amplitude in the thermal state. To this end, we vary the temporal delay τ between the postselection and the target channel over an interval from -4 to 4 ps with a temporal resolution of 60 fs. For the conditional analysis, we select regions of fixed phase $\varphi_{ps} = \frac{\pi}{2} \pm \frac{\pi}{16}$ and varying amplitudes $|\gamma_{ps}|$ of 0.5 ± 0.125, 1.5 ± 0.125, 2.5 ± 0.125, 3.5 ± 0.125, and 4.5 ± 0.125. For each configuration, we construct the corresponding conditional Husimi-Q distributions $Q_c(\delta)$ and use them to compute the time traces of the amplitude A_c, the average variance $\overline{\mathrm{Var}}_c(\hat{q}, \hat{p})$, the mean photon number $\langle \hat{n} \rangle_c$ and the second-order correlation function $g_c^{(2)}(0)$. The results of this analysis are presented in figure 8.4. The top row illustrates the conditional Husimi-Q distribution $Q_c(\delta)$ for $\gamma_{ps} = 2.5i$ at representative time delays of 0 ps, 1 ps, and 2 ps. The four panels (a-d) below display the time traces of A_c, $\overline{\mathrm{Var}}_c(\hat{q}, \hat{p})$, $\langle \hat{n} \rangle_c$ and $g_c^{(2)}(0)$.

We begin the discussion by examining the temporal evolution of $Q_c(\delta)$. The distribution starts at $\tau = 0$ as a coherent state broadened by the additional vacuum. As the time delay increases, the distribution broadens equally along $\mathrm{Re}(\delta)$ and $\mathrm{Im}(\delta)$, while its displacement from the origin progressively diminishes. After a time delay of around $\tau = 2$ ps, nearly all amplitude and phase correlations between postselection and target channel are lost, and $Q_c(\delta)$ has converged to the unconditional distribution $Q_t(\delta)$. Next, we examine the temporal evolution of A_c, shown in panel (a). The amplitude reaches its maximum at $\tau = 0$, with the peak value increasing with increasing $|\gamma_{ps}|$. As the time delay increases, the curves decay equally until they approach a minimal value close to zero at approximately $|\tau| = 2.3$ ps. For larger time delays, A_c exhibits a revival in time, whereby the amplitudes of these created sidebands increase with $|\gamma_{ps}|$. The observed decoherence behavior of A_c, including the formation of sidebands, can be traced back to the signal's power spectrum. Precisely, one finds from the Wiener-Khinchin theorem [10, p. 56-59] that the temporal evolution of a light field's phase uncertainty follows the Fourier transform of the signal's power spectrum. Accordingly, the rectangular power spectrum leads to the

formation of sidebands at which the phase information is revived. As A_c depends on the phase-dependent $\langle\hat{q}\rangle_\mathrm{c}$ and $\langle\hat{p}\rangle_\mathrm{c}$, A_c exhibits qualitatively the same decay and revival features as the phase uncertainty of the light field. In addition to the general decoherence process, we further note irregular dips in the time traces, whose depths increase with $|\gamma_\mathrm{ps}|$, but whose positions remain constant. We attribute these dips to additional external phase noise, whose magnitude may fluctuate between consecutive measurements. A more detailed analysis of the phase noise is given in the next section. Panel (b) shows the temporal evolution of the averaged variance $\overline{\mathrm{Var}}_\mathrm{c}(\hat{q},\hat{p})$. In agreement with theory, the general behavior is independent of the selected value of $|\gamma_\mathrm{ps}|$. The variance exhibits a local minimum at $|\tau| = 0$ and increases with increasing time delay, eventually converging to the variance of the unconditional state. As observed for A_c, local maxima appear whenever the system is affected by additional phase noise. The variance, however, responds more sensitively to such perturbations, since the expectation values $\langle\hat{q}\rangle_\mathrm{c}$ and $\langle\hat{p}\rangle_\mathrm{c}$ enter quadratically in the expression. Panel (c) depicts the temporal evolution of $\langle\hat{n}\rangle_\mathrm{c}$. Similar to the previously discussed observables, $\langle\hat{n}\rangle_\mathrm{c}$ is extremal at $|\tau| = 0$, where the absolute value, dependent on $|\gamma_\mathrm{ps}|$, either exceeds or falls below $\langle\hat{n}\rangle_\mathrm{t}$. For time delays long compared to the amplitude coherence time, all curves converge towards $\langle\hat{n}\rangle_\mathrm{t}$. We have to highlight that the time traces exhibit no additional irregular fluctuations, indicating that the setup does not suffer significantly from additional irregular amplitude noise. Finally, panel (d) presents the temporal evolution of $g_\mathrm{c}^{(2)}(0)$. The correlation function attains its minimum at $|\tau| = 0$, with the minimal value decreasing as $|\gamma_\mathrm{ps}|$ increases. The decrease of $g_\mathrm{c}^{(2)}(0)$ occurs, as A_c increases with $|\gamma_\mathrm{ps}|$ while the distribution's variance remains constant. In reverse, this prevents the conditional state of reaching $g^{(2)}(0)_\mathrm{c} = 1$ as the distribution's additional broadening can be associated with a non-vanishing thermal photon number component. Finally, we note that the decay times of $\langle\hat{n}\rangle_\mathrm{c}$ are $g_\mathrm{c}^{(2)}(0)$ are comparable. This again indicates that both quantities depend solely on amplitude noise and are independent of phase noise.

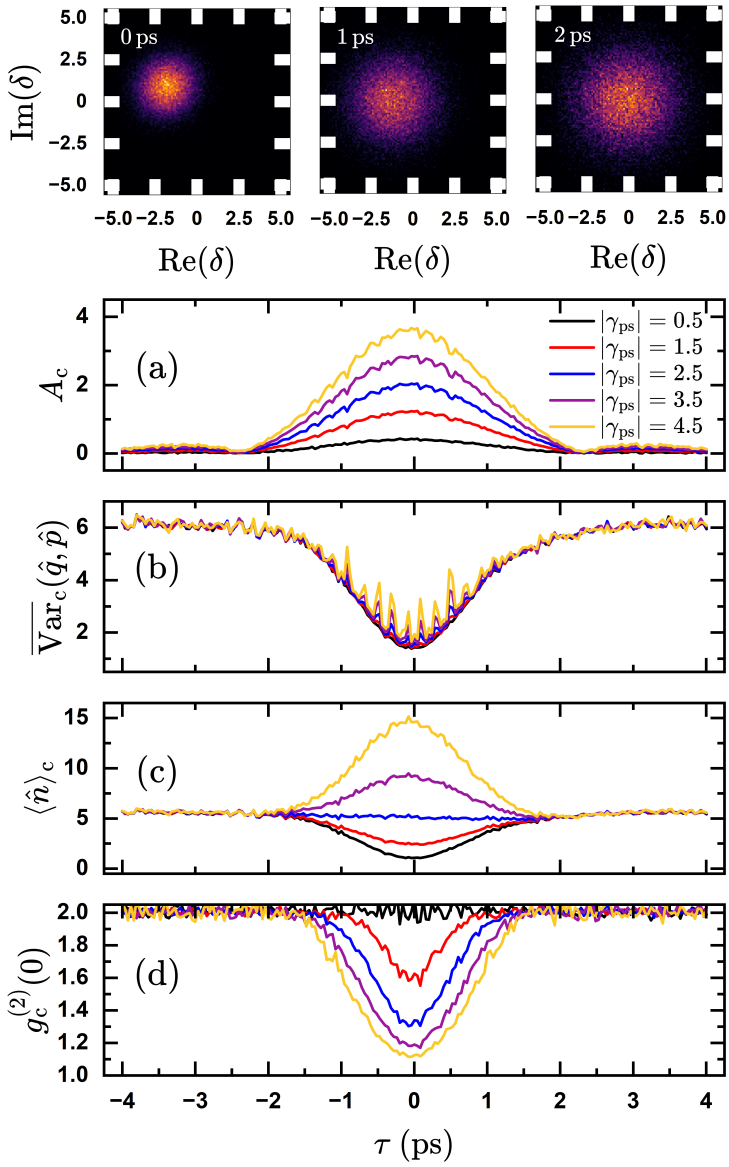

Figure 8.4: Illustration of the main results using conditional non-stationary optical tomography. The top row displays the conditional Husimi-Q distribution in the target channel for representative time delays of 0 ps, 1 ps, and 2 ps. The panels (a-d) below display the time traces of the amplitude A_c, the average variance $\overline{\mathrm{Var}_c}(\hat{q},\hat{p})$, the average photon number $\langle\hat{n}\rangle_c$ and the second-order correlation function $g_c^{(2)}(0)$. The postselected amplitudes intervals have a common width of ± 0.125, while the phase was postselected to $\frac{\pi}{2} \pm \frac{\pi}{16}$ corresponding to values around the positive y-axis.

8.4 Decoherence Analysis Based on the Distributions of Relative Amplitude and Phase

We conclude the chapter by examining the temporal evolution of amplitude and phase noise directly. For this purpose, we first express the quadrature pairs recorded in both channels in the form of amplitudes A_{ps}, A_{t} and phases φ_{ps}, φ_{t} and use them to compute sets of the amplitude difference $\Delta A = A_{\mathrm{t}} - A_{\mathrm{ps}}$ and the relative phase $\Delta\varphi = \varphi_{\mathrm{t}} - \varphi_{\mathrm{ps}}$. Finally, we construct the frequency distributions of ΔA and $\Delta\varphi$ and consider them as functions of the time delay τ. The principal results are presented as two-dimensional heatmaps that display the distributions dependent on the time delay. In addition, we further plot the time evolutions of the heatmap profiles at $\Delta A = 0$ and $\Delta\varphi = 0$ as well as the distributions' variances.

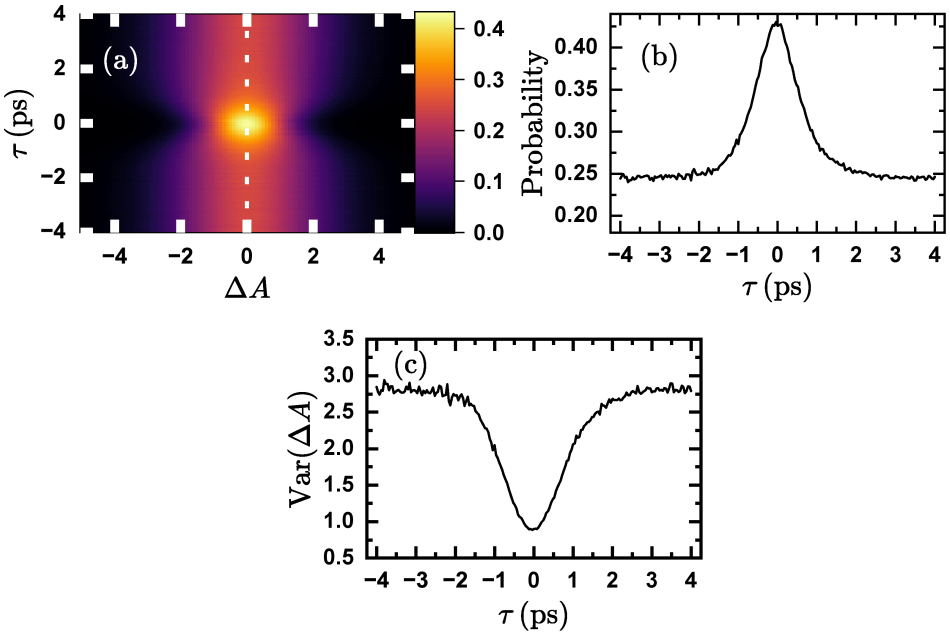

Figure 8.5: Time evolution of the amplitude differences ΔA, dependent on the time delay τ. Panel (a) displays the time evolution of the associated frequency histograms in the form of a heatmap. In addition, panels (b) and (c) show the temporal evolutions of the heatmap's profile at $\Delta A = 0$ and of the variance $\mathrm{Var}(\Delta A)$.

We begin with the analysis of the amplitude differences, whose principal results are illustrated in figure 8.5. The two-dimensional heatmap is displayed in panel (a), the time evolutions of the heatmap's profile at $\Delta A = 0$ and of the variance $\mathrm{Var}(\Delta A)$

are shown in panels (b) and (c). Consistent with the results of the conditional non-stationary analysis in the previous section, the distribution of ΔA exhibits a minimal variance of approximately 0.88 at $\tau = 0$ and broadens with increasing time delay. For $|\tau| \geq 1.7\,\mathrm{ps}$, the amplitude correlations between the two channels are lost, and the distribution reaches its maximal width. As expected from the time traces of $\langle \hat{n} \rangle_\mathrm{c}$ and $g_\mathrm{c}^{(2)}(0)$, the time evolution of the relative amplitude exhibits no irregular fluctuations.

After analyzing the decoherence dynamics of the relative amplitude, we turn to the decoherence dynamics of the relative phase. Two complications arise when examining the distribution of the relative phase. First, the phase is periodic, so that $\varphi = -\pi$ and $\varphi = \pi$ must be considered equal. Second, the native distribution is not centered around zero but exhibits an offset that depends on the time delay. To address these issues, we recenter the distributions after construction so that every distribution is centered around $\Delta\varphi = 0$. To quantify the width of the distribution, we replace the conventional variance $\mathrm{Var}(\Delta\varphi)$ with the circular variance $\mathrm{Var}_\varphi(\Delta\varphi)$ [133, p. 32]. This modification is required because the phase renormalization can be applied to the frequency distribution, but not directly to the raw set of relative phases. The circular variance is defined by

$$\mathrm{Var}_\varphi\left(\{\varphi_\mathrm{i}\}\right) = 1 - \frac{1}{n}\left|\sum_{\mathrm{i}=1}^{n} \exp(i\varphi_\mathrm{i})\right|, \tag{8.8}$$

and bypasses the limitation of the circular distribution by mapping the individual phase values onto points on the unit circle in the complex plane. This representation naturally accounts for the periodicity of the phase and ensures the equivalence of $-\pi$ and π. In contrast to the conventional variance, the circular variance is limited to the value range between zero and one, where a value of zero denotes a singular distribution and a value of one a maximally mixed distribution. The results of the analysis of the phase distribution are illustrated in figure 8.6. The two-dimensional heatmap of the relative phase distribution dependent on τ is shown in panel (a). The time evolutions of the heatmap's profile at $\Delta\varphi = 0$ and the circular variance are plotted in the panels (c) and (d) in the form of black lines, respectively. In analogy to the distribution of ΔA, the phase distribution of $\Delta\varphi$ exhibits a local minimum at $\tau = 0$, corresponding to a circular variance of 0.28. With increasing time delay, the phase distribution progressively broadens and approaches an approximately uniform distribution after around 2.3 ps. For larger delays, we observe a slight phase revival, due to the signal's rectangular power spectrum, as discussed for the time trace of A_c in the previous section. Apart from the general dephasing dynamics, we also note time delays at which the phase distribution suddenly and irregularly broadens. The positions of these outliers coincide with the positions of the outliers

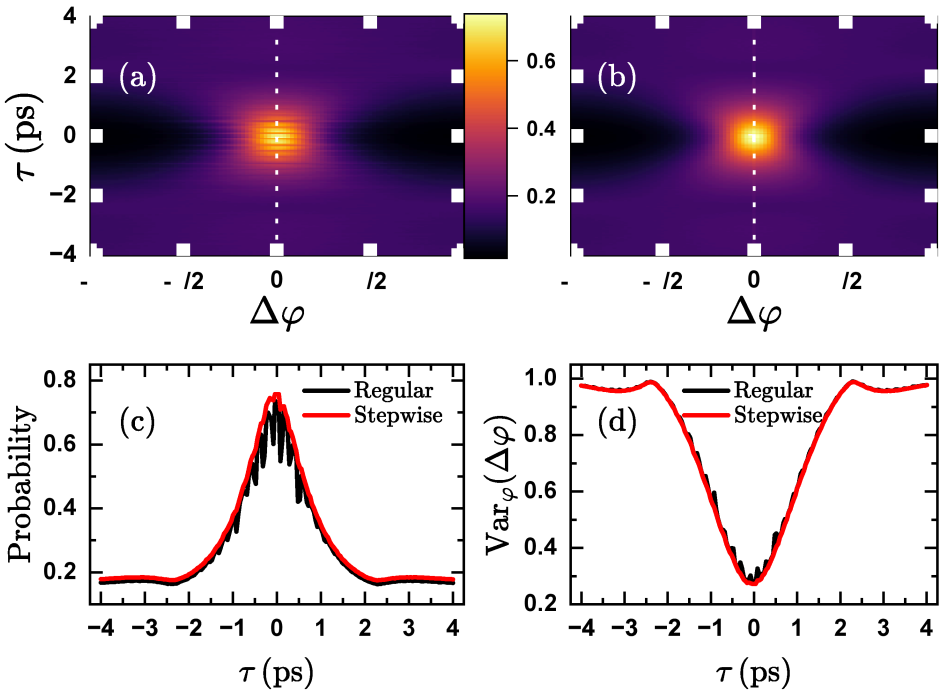

Figure 8.6: Time evolution of the distribution of the relative phase between the two channels $\Delta\varphi$, dependent on the time delay between the two channels τ. Panel (a) displays the evolution, where the histograms are calculated from the complete dataset. Panel (b) displays the same relation, but the histograms are constructed gradually from smaller subsets corresponding to a recording time of 1 ms and then averaged. Panels (c) and (d) display the time evolution of the heatmap at $\Delta\varphi = 0$ and of the distribution's circular variance Var_φ. The curves associated with the naive computation approach are shown as black lines and the curves associated with the gradual calculation approach are displayed as red lines.

found in the time traces of A_c and $\overline{\mathrm{Var}}_\mathrm{c}(\hat{q},\hat{p})$. This confirms that the additional fluctuations in the time traces of A_c and $\overline{\mathrm{Var}}_\mathrm{c}(\hat{q},\hat{p})$ are indeed caused by additional phase noise. To investigate the origin of this phase noise, we perform a Fourier analysis of the calculated relative phases. The dominant frequency components lie below 1 kHz, indicating that the external phase noise is most likely of mechanical origin, for example, due to vibrating components or the exposure of the light field to air perturbations.

We conclude the section by removing the low-frequency phase noise from the phase distribution. To this end, we divide the set of phases into smaller subsets with a size of 75400 values, corresponding to a recording time of around 1 ms, shorter than the oscillation periods of the found mechanical oscillations. For each subset, we

construct the corresponding frequency distribution individually. Finally, we obtain the cleaned distribution of the whole data set by averaging over the constructed histograms. The circular variance is cleaned similarly: First, we calculate the circular variance on the individual subsets, and afterward we average the found values. The corrected two-dimensional heatmap is shown in figure 8.6, panel (b). The corresponding corrected time evolutions of the heatmap's profile at $\Delta\varphi = 0$ and of the circular variance are presented in the panels (c) and (d) as red lines. While the overall shapes of the heatmap and the associated profiles remain unchanged, the artifacts induced by spontaneously occurring additional external phase noise are no longer present. This confirms the effectiveness of this approach.

8.5 Conclusion

In conclusion, we have introduced a sixteen-port homodyne detection scheme and benchmarked its capabilities by investigating the ultrafast dynamics of a thermal light field. Our conditional analysis at zero time delay has experimentally shown that a thermal light field reduces to a coherent state at an instant time, in agreement with theory. Especially for phase-independent observables such as the average photon number, we observe good agreement between theory and experiment. For phase-dependent quantities as A_c, however, we do not reach the same level of agreement as demonstrated for the twelve-port detector [129]. We attribute this to the fact that the previous study used phase reconstruction to estimate the phase information in the target channel, thereby excluding additional phase fluctuations between the two channels that occur on timescales short compared to the applied sinusoidal phase modulation. In our case, however, the phase information is directly measured and consequently includes the additional external phase noise. Nonetheless, our non-stationary analysis has demonstrated that we are still able to observe the ultrafast decoherence dynamics of the thermal light field on the sub-picosecond timescale. Finally, our analysis of the relative amplitude and phase difference between the two channels confirmed that the phase noise indeed has a mainly mechanical origin. Meanwhile, no significant external amplitude noise could be observed. The finally introduced procedure to clean the phase distribution from external noise showed that the distribution can indeed be corrected. While this correction approach is most certainly not applicable to regular conditional analysis, because the number of remaining quadratures would become too low, it may be applied to unconditional analyses that focus on the phase relation between the two channels. Probably the biggest advantage of a sixteen-port detection scheme over a twelve-port detection scheme lies not in the conditional analysis of a single-mode signal but in the analysis of a two-mode signal. In this case, the precise phase relation between the two channels is not necessarily known a priori but is governed by the dynamic correlations between the two modes. Consequently, it becomes crucial to measure the phase information of both channels individually, as phase reconstruction could distort the results. To minimize the influence of external noise on these kinds of measurements, future experiments should minimize external perturbations, for example, by sealing the beam paths from turbulent air.

9 Conclusion and Outlook

The investigations conducted throughout this thesis have yielded several key results that are summarized in the following. We started the studies in chapter 6 by addressing the discrepancy between established quantum resource theories that primarily focus on non-classical light fields and experimental practice, where one seeks to replace expensive non-classical light sources with cheaper, more reliable classical ones. To bridge part of this gap, we introduced a simple quantum resource-theoretical model that describes the emission of a realistic laser as a displaced thermal state and quantifies its resourcefulness via quantum coherence. Subsequent experimental analyses via optical homodyne tomography then demonstrated good agreement between the coherence properties extracted from the states' density matrices and the model's predictions. In addition, we examined the role of quantum coherence in a concrete application: the preparation of qubit superposition states via Rabi driving with a short laser pulse. Our simulations revealed that quantum coherence arises in this case as a fundamental requirement for the preparation of high-quality qubit superposition states. This finding highlights the limitations of the commonly employed second-order correlation function $g^{(2)}$, which fails to predict the outcome. Most importantly, we found that quantum coherence in the absence of dephasing only depends on the coherent and thermal photon numbers. This enables a simpler estimation of the quantum coherence, for example, from the phase-averaged Husimi-Q distribution without the requirement of a stable external phase reference. In the subsequent chapter 7, we applied this scheme to investigate the buildup of quantum coherence in a non-resonantly optically excited polariton condensate spectroscopically. To enhance the condensation process, we combined long-lifetime polaritons, expected to facilitate better thermalization, with a spatial separation of the condensate and the excitation region, thereby potentially minimizing interactions between the condensate and the reservoir. In contrast to previous studies employing shorter-living polaritons and Gaussian excitation profiles [77], we observed a rapid emergence of quantum coherence immediately above the condensation threshold. Furthermore, we detected a pronounced blueshift of the condensate mode relative to the ground state of the uncondensed polaritons, which we attribute to interactions with dark excitons possessing large in-plane momentum. These findings suggest that the mere presence of a reservoir is not necessarily limiting the coherence. Rather, it may be interactions with strongly fluctuating particles, such as free electrons and holes, that degrade the coherence of

the condensate. Complementary to these experimental results, we also performed numerical simulations to determine the limitations of the displaced thermal state model. To this end, we subjected a coherent state to sinusoidal photon-number fluctuations and calculated the coherence properties of the resulting averaged state. For the second-order correlation function $g^{(2)}(0)$, we observed good agreement between model predictions and the true values for small and moderate perturbations. In contrast, when considering quantum coherence, the model fails rapidly, and the predicted values deviate significantly from the true coherence. Only in the regime of weak perturbations may the model provide a conservative lower-bound estimate. Finally, we introduced a time-resolved extension of the displaced thermal state analysis, which enables the investigation of the temporal evolution of the light field both in terms of its Husimi-Q distribution and its coherence properties on the millisecond timescale. In the final result chapter 8, we shifted the focus toward the specific requirements of semiconductor spectroscopy. To this end, we developed a sixteen-port homodyne detection scheme that splits the signal into postselection and target channels, each sampling the corresponding Husimi-Q distribution. This configuration enables us, at the cost of additional noise, to perform non-stationary and conditional analyses with a temporal resolution down to 100 fs and a wide range of a posteriori applicable postselection conditions without the need for a stable phase reference to an external local oscillator. The setup performance was then benchmarked on a thermal light field. Comparison between experimental results and theoretical predictions demonstrated good agreement for phase-independent observables, while the phase-dependent observables revealed the influence of external phase noise. A subsequent analysis of the relative amplitudes and phases between the two channels confirmed this interpretation. Despite these limitations, the setup proved capable of resolving the decoherence dynamics of the thermal light field. Finally, we also introduced a versatile recording suite that enables not only automated data acquisition, but also in situ characterization of the current light field during the experiments. This approach minimizes the conventional separation between measurement and subsequent analysis, allowing for the identification of potentially interesting phenomena already at the stage of recording. As a result, the overall experimental optimization process may be significantly accelerated.

While our investigations have revealed a variety of interesting effects, this work does not represent an endpoint but rather opens the path to a broad range of future experiments in quantum optics and semiconductor spectroscopy. First, our analysis of the resourcefulness of realistic laser fields for quantum applications is limited to a single specific task. Future studies could extend these considerations to more sophisticated and technologically more relevant protocols [84, 85, 86, 87]. Alternatively, previous investigations on coherent qubit control could be revisited while explicitly accounting for the properties of realistic lasers [88, 89]. Further, the

concept of quantum coherence could be used to investigate the emission of other non-conventional partially coherent light sources, such as free-electron lasers [90] or Bose-Einstein condensates from photons [91]. Finally, spectroscopic scenarios may also benefit from analyses grounded in quantum coherence. For instance, recent studies employing quantum coherence have revealed quantum features in Cherenkov radiation, which previously had been considered purely classical [92]. Second, our optimization of the coherence properties of a polariton condensate can be regarded as a proof of concept. Future investigations in this direction could systematically investigate how the properties of the polaritons or the cross-section profile of the annular trap affect the condensation threshold and the coherence properties of the condensate state. Such studies may pave the way for the use of polariton condensates as a low-threshold source of resourceful coherent light fields. Third, the introduced sixteen-port detection scheme may serve as a powerful and versatile tool for semiconductor spectroscopy. While the benchmark on a single thermal light field already yielded favourable results, the most promising capabilities of the sixteen-port detector lie in the analysis of the correlation dynamics between two modes. In such scenarios, the relative phase between the two channels is not known a priori but represents a quantity of central interest for understanding the dynamics between the two modes, thereby preventing the employment of a twelve-port detection scheme. This capability may facilitate the investigation of coupled systems, such as polariton condensates in coupled micropillar microcavities [134], or competing modes of different polarization or energy in unstable systems. Last but not least, the capabilities of the implemented monitoring software can also be further extended. While the current implementation can be considered a proof of concept, it prioritizes expandability over computation speed. Consequently, more specialized analysis tools tailored to specific evaluation methods could significantly improve processing performance. For example Trifonov et al. [135] demonstrated rapid $g^{(2)}(0)$ evaluation with an acumulation and calculation cycle frequency exceeding 1 kHz using a comparable detection setup. Such developments may enable the integration of quantum-optical analysis techniques into industrial applications.

Bibliography

[1] E. Chitambar and G. Gour, "Quantum resource theories," Rev. Mod. Phys. **91**, 025001 (2019).

[2] J. I. Cirac and P. Zoller, "Quantum Computations with Cold Trapped Ions," Phys. Rev. Lett. **74**, 4091 (1995).

[3] Q. A. Turchette, C. S. Wood, B. E. King, C. J. Myatt, D. Leibfried, W. M. Itano, C. Monroe, and D. J. Wineland, "Deterministic Entanglement of Two Trapped Ions," Phys. Rev. Lett. **81**, 3631 (1998).

[4] S. Ahn, A. S. Moskalenko, V. Y. Chernyak, and S. Mukamel, "Qubit entanglement generated by classical light driving an optical cavity," Phys. Rev. Res. **5**, 043195 (2023).

[5] B. Qi, "True randomness from an incoherent source," Rev. Sci. Instrum. **88**, 113101 (2017).

[6] J. Thewes, C. Lüders, and M. Aßmann, "Eavesdropping attack on a trusted continuous-variable quantum random-number generator," Phys. Rev. A **100**, 052318 (2019).

[7] H. Deng, H. Haug, and Y. Yamamoto, "Exciton-polariton Bose-Einstein condensation," Rev. Mod. Phys. **82**, 1489 (2010).

[8] P. J. Mohr, D. B. Newell, B. N. Taylor, and E. Tiesinga, "CODATA recommended values of the fundamental physical constants: 2022," Rev. Mod. Phys. **97**, 025002 (2025).

[9] M. M. Wilde, *Quantum Information Theory*, 2nd ed. (Cambridge University Press, 2017).

[10] L. Mandel and E. Wolf, *Optical Coherence and Quantum Optics* (Cambridge University Press, 1995).

[11] W. P. Schleich, *Quantum Optics in Phase Space* (Wiley, 2001).

[12] J. Thewes, "Non-Stationary Optical Homodyne Tomography," PhD thesis (Technische Universität Dortmund, 2018).

[13] R. J. Glauber, "Photon Correlations," Phys. Rev. Lett. **10**, 84 (1963).

[14] E. C. G. Sudarshan, "Equivalence of Semiclassical and Quantum Mechanical Descriptions of Statistical Light Beams," Phys. Rev. Lett. **10**, 277 (1963).

[15] K. Husimi, "Some Formal Properties of the Density Matrix," Proceedings of the Physico-Mathematical Society of Japan. 3rd Series **22**, 264 (1940).

[16] Y. Kano, "A New Phase-Space Distribution Function in the Statistical Theory of the Electromagnetic Field," J. Math. Phys. **6**, 1913 (1965).

[17] E. Wigner, "On the Quantum Correction For Thermodynamic Equilibrium," Phys. Rev. **40**, 749 (1932).

[18] D. F. Walls and G. J. Milburn, *Quantum Optics*, 3rd ed. (Springer Nature Switzerland, 2025).

[19] W. Vogel and D.-G. Welsch, *Quantum Optics* (Wiley, 2006).

[20] G. Lachs, "Theoretical Aspects of Mixtures of Thermal and Coherent Radiation," Phys. Rev. **138**, B1012 (1965).

[21] K. E. Cahill and R. J. Glauber, "Ordered Expansions in Boson Amplitude Operators," Phys. Rev. **177**, 1857 (1969).

[22] G. S. Agarwal and E. Wolf, "Calculus for Functions of Noncommuting Operators and General Phase-Space Methods in Quantum Mechanics. I. Mapping Theorems and Ordering of Functions of Noncommuting Operators," Phys. Rev. D **2**, 2161 (1970).

[23] G. S. Agarwal and E. Wolf, "Calculus for Functions of Noncommuting Operators and General Phase-Space Methods in Quantum Mechanics. II. Quantum Mechanics in Phase Space," Phys. Rev. D **2**, 2187 (1970).

[24] M. Fox, *Quantum Optics* (Oxford University Press, 2006).

[25] R. H. Brown and R. Twiss, "LXXIV. A new type of interferometer for use in radio astronomy," The London, Edinburgh, and Dublin Philosophical Magazine and Journal of Science **45**, 663 (1954).

[26] T. Baumgratz, M. Cramer, and M. B. Plenio, "Quantifying Coherence," Phys. Rev. Lett. **113**, 140401 (2014).

[27] S. Rana, P. Parashar, and M. Lewenstein, "Trace-distance measure of coherence," Phys. Rev. A **93**, 012110 (2016).

[28] M. Fox, *Optische Eigenschaften von Festkörpern* (De Gruyter Oldenbourg, 2020).

[29] A. V. Kavokin, J. J. Baumberg, G. Malpuech, and F. P. Laussy, *Microcavities* (Oxford University Press, 2017).

[30] A. Rahimi-Iman, *Polariton Physics* (Springer International Publishing, 2020).

[31] M. Grundmann, *The Physics of Semiconductors*, 4th ed. (Springer International Publishing, 2021).

[32] J. J. Hopfield, "Theory of the Contribution of Excitons to the Complex Dielectric Constant of Crystals," Phys. Rev. **112**, 1555 (1958).

[33] A. Rahimi-Iman, "Nichtlineare Effekte in III/V Quantenfilm-Mikroresonatoren: Von dynamischer Bose-Einstein-Kondensation hin zum elektrisch betriebenen Polariton-Laser," PhD thesis (Julius-Maximilians-Universität Würzburg, 2013).

[34] F. Dalfovo, S. Giorgini, L. P. Pitaevskii, and S. Stringari, "Theory of Bose-Einstein condensation in trapped gases," Rev. Mod. Phys. **71**, 463 (1999).

[35] R. Onofrio, C. Raman, J. M. Vogels, J. R. Abo-Shaeer, A. P. Chikkatur, and W. Ketterle, "Observation of Superfluid Flow in a Bose-Einstein Condensed Gas," Phys. Rev. Lett. **85**, 2228 (2000).

[36] O. Penrose and L. Onsager, "Bose-Einstein Condensation and Liquid Helium," Phys. Rev. **104**, 576 (1956).

[37] T. Fließbach, *Statistische Physik*, 6th ed. (Springer, 2018).

[38] M. H. Anderson, J. R. Ensher, M. R. Matthews, C. E. Wieman, and E. A. Cornell, "Observation of Bose-Einstein Condensation in a Dilute Atomic Vapor," Science **269**, 198 (1995).

[39] J. Kasprzak, M. Richard, S. Kundermann, A. Baas, P. Jeambrun, J. M. J. Keeling, F. M. Marchetti, M. H. Szymańska, R. André, J. L. Staehli, V. Savona, P. B. Littlewood, B. Deveaud, and L. S. Dang, "Bose-Einstein condensation of exciton polaritons," Nature **443**, 409 (2006).

[40] T. Guillet and C. Brimont, "Polariton condensates at room temperature," C. R. Phys. **17**, 946 (2016).

[41] A. Kavokin, G. Malpuech, and F. P. Laussy, "Polariton laser and polariton superfluidity in microcavities," Phys. Lett. A **306**, 187 (2003).

[42] J. Schmutzler, P. Lewandowski, M. Aßmann, D. Niemietz, S. Schumacher, M. Kamp, C. Schneider, S. Höfling, and M. Bayer, "All-optical flow control of a polariton condensate using nonresonant excitation," Phys. Rev. B **91**, 195308 (2015).

[43] S. Alyatkin, H. Sigurdsson, A. Askitopoulos, J. D. Töpfer, and P. G. Lagoudakis, "Quantum fluids of light in all-optical scatterer lattices," Nat. Commun. **12**, 5571 (2021).

[44] S. Alyatkin, K. Sitnik, V. K. Daníelsson, Y. V. Kartashov, J. D. Töpfer, H. Sigurðsson, and P. G. Lagoudakis, "Quantum fluids of light in 2D artificial reconfigurable aperiodic crystals with tailored coupling," Sci. Adv. **11**, eadz2484 (2025).

[45] J. Schmutzler, T. Kazimierczuk, Ö. Bayraktar, M. Aßmann, M. Bayer, S. Brodbeck, M. Kamp, C. Schneider, and S. Höfling, "Influence of interactions with noncondensed particles on the coherence of a one-dimensional polariton condensate," Phys. Rev. B **89**, 115119 (2014).

[46] A. Askitopoulos, H. Ohadi, A. V. Kavokin, Z. Hatzopoulos, P. G. Savvidis, and P. G. Lagoudakis, "Polariton condensation in an optically induced two-dimensional potential," Phys. Rev. B **88**, 041308 (2013).

[47] K. Orfanakis, A. F. Tzortzakakis, D. Petrosyan, P. G. Savvidis, and H. Ohadi, "Ultralong temporal coherence in optically trapped exciton-polariton condensates," Phys. Rev. B **103**, 235313 (2021).

[48] H. P. Yuen and V. W. S. Chan, "Noise in homodyne and heterodyne detection," Opt. Lett. **8**, 177 (1983).

[49] G. L. Abbas, V. W. S. Chan, and T. K. Yee, "Local-oscillator excess-noise suppression for homodyne and heterodyne detection," Opt. Lett. **8**, 419 (1983).

[50] C. Lüders, F. Barkhausen, M. Pukrop, E. Rozas, J. Sperling, J. Sperling, S. Schumacher, S. Schumacher, S. Schumacher, and M. Aßmann, "Continuous-variable quantum optics and resource theory for ultrafast semiconductor spectroscopy [Invited]," Opt. Mater. Express **13**, 2997 (2023).

[51] Z. Y. Ou and L. Mandel, "Derivation of reciprocity relations for a beam splitter from energy balance," Am. J. Phys. **57**, 66 (1989).

[52] N. Walker and J. Carroll, "Simultaneous phase and amplitude measurements on optical signals using a multiport junction," Electronics Letters **20**, 981 (1984).

[53] N. G. Walker and J. E. Carroll, "Multiport homodyne detection near the quantum noise limit," Opt. Quantum Electron. **18**, 355 (1986).

[54] C. Lüders, "Measuring coherence properties of exciton-polaritons with homodyne detection," PhD thesis (Technische Universität Dortmund, 2022).

[55] R. Kumar, E. Barrios, A. MacRae, E. Cairns, E. H. Huntington, and A. I. Lvovsky, "Versatile wideband balanced detector for quantum optical homodyne tomography," Opt. Commun. **285**, 5259 (2012).

[56] A. I. Lvovsky, "Iterative maximum-likelihood reconstruction in quantum homodyne tomography," J. Opt. B: Quantum Semiclassical Opt. **6**, S556 (2004).

[57] Y. Vardi and D. Lee, "From Image Deblurring to Optimal Investments: Maximum Likelihood Solutions for Positive Linear Inverse Problems," Royal Statistical Society. Journal. Series B: Methodological. **55**, 569 (1993).

[58] J. M. Pérez-Jordá, "On the recursive solution of the quantum harmonic oscillator," European Journal of Physics **39**, 015402 (2017).

[59] G. Roumpos and S. T. Cundiff, "Multichannel homodyne detection for quantum optical tomography," J. Opt. Soc. Am. B **30**, 1303 (2013).

[60] C. Lüders, J. Thewes, and M. Aßmann, "Real time $g^{(2)}$ monitoring with 100 kHz sampling rate," Opt. Express **26**, 24854 (2018).

[61] C. Lüders and M. Aßmann, "Distinguishing intrinsic photon correlations from external noise with frequency-resolved homodyne detection," Sci. Rep. **10**, 22411 (2020).

[62] M. Steger, C. Gautham, D. W. Snoke, L. Pfeiffer, and K. West, "Slow reflection and two-photon generation of microcavity exciton-polaritons," Optica **2**, 1 (2015).

[63] Y. Brune, E. Rozas, K. West, K. Baldwin, L. N. Pfeiffer, J. Beaumariage, H. Alnatah, D. W. Snoke, and M. Aßmann, "Quantum coherence of a long-lifetime exciton-polariton condensate," Commun. Mater. **6**, 123 (2025).

[64] M. B. Plenio and S. Virmani, "An introduction to entanglement measures," Quantum Inf. Comput. **7**, 1 (2007).

[65] M. Avesani, D. G. Marangon, G. Vallone, and P. Villoresi, "Source-device-independent heterodyne-based quantum random number generator at 17 Gbps," Nat. Commun. **9**, 5365 (2018).

[66] C. Bruynsteen, T. Gehring, C. Lupo, J. Bauwelinck, and X. Yin, "100-Gbit/s Integrated Quantum Random Number Generator Based on Vacuum Fluctuations," PRX Quantum **4**, 010330 (2023).

[67] F. Grosshans, G. Van Assche, J. Wenger, R. Brouri, N. J. Cerf, and P. Grangier, "Quantum key distribution using gaussian-modulated coherent states," Nature **421**, 238 (2003).

[68] E. Agudelo, J. Sperling, and W. Vogel, "Quasiprobabilities for multipartite quantum correlations of light," Phys. Rev. A **87**, 033811 (2013).

[69] F. Shahandeh, A. P. Lund, and T. C. Ralph, "Quantum Correlations in Nonlocal Boson Sampling," Phys. Rev. Lett. **119**, 120502 (2017).

[70] A. Streltsov, H. Kampermann, S. Wölk, M. Gessner, and D. Bruß, "Maximal coherence and the resource theory of purity," New J. Phys. **20**, 053058 (2018).

[71] J. Ma, B. Yadin, D. Girolami, V. Vedral, and M. Gu, "Converting Coherence to Quantum Correlations," Phys. Rev. Lett. **116**, 160407 (2016).

[72] H. Zhu, Z. Ma, Z. Cao, S.-M. Fei, and V. Vedral, "Operational one-to-one mapping between coherence and entanglement measures," Phys. Rev. A **96**, 032316 (2017).

[73] T. H. Maiman, "Stimulated Optical Radiation in Ruby," Nature **187**, 493 (1960).

[74] C. T. Santis, S. T. Steger, Y. Vilenchik, A. Vasilyev, and A. Yariv, "High-coherence semiconductor lasers based on integral high-Q resonators in hybrid Si/III-V platforms," Proc. Natl. Acad. Sci. U.S.A. **111**, 2879 (2014).

[75] S. Kim, B. Zhang, Z. Wang, J. Fischer, S. Brodbeck, M. Kamp, C. Schneider, S. Höfling, and H. Deng, "Coherent Polariton Laser," Phys. Rev. X **6**, 011026 (2016).

[76] J. I. de Vicente and A. Streltsov, "Genuine quantum coherence," J. Phys. A: Math. Theor. **50**, 045301 (2016).

[77] C. Lüders, M. Pukrop, E. Rozas, C. Schneider, S. Höfling, J. Sperling, S. Schumacher, and M. Aßmann, "Quantifying Quantum Coherence in Polariton Condensates," PRX Quantum **2**, 030320 (2021).

[78] Y. Brune, M. Cizauskas, and M. Aßmann, "Quantum resource theory of lasers," Phys. Rev. Res. **8**, 013170 (2026).

[79] C. Gardiner and P. Zoller, *A Handbook of Markovian and non-Markovian Quantum Stochastic Methods with Applications to Quantum Optics*, 3rd ed. (Springer Berlin/Heidelberg, 2004).

[80] N. Lambert, E. Giguère, P. Menczel, B. Li, P. Hopf, G. Suárez, M. Gali, J. Lishman, R. Gadhvi, R. Agarwal, A. Galicia, N. Shammah, P. Nation, J. R. Johansson, S. Ahmed, S. Cross, A. Pitchford, and F. Nori, "QuTiP 5: The Quantum Toolbox in Python," Physics Reports **1153**, 1 (2026).

[81] J. H. Eberly, N. B. Narozhny, and J. J. Sanchez-Mondragon, "Periodic Spontaneous Collapse and Revival in a Simple Quantum Model," Phys. Rev. Lett. **44**, 1323 (1980).

[82] J. Gea-Banacloche, "Collapse and revival of the state vector in the Jaynes-Cummings model: An example of state preparation by a quantum apparatus," Phys. Rev. Lett. **65**, 3385 (1990).

[83] S. J. D. Phoenix and P. L. Knight, "Establishment of an entangled atom-field state in the Jaynes-Cummings model," Phys. Rev. A **44**, 6023 (1991).

[84] N. V. Vitanov, A. A. Rangelov, B. W. Shore, and K. Bergmann, "Stimulated Raman adiabatic passage in physics, chemistry, and beyond," Rev. Mod. Phys. **89**, 015006 (2017).

[85] D. Jaksch, J. I. Cirac, P. Zoller, S. L. Rolston, R. Côté, and M. D. Lukin, "Fast Quantum Gates for Neutral Atoms," Phys. Rev. Lett. **85**, 2208 (2000).

[86] I. Schwartz, D. Cogan, E. R. Schmidgall, Y. Don, L. Gantz, O. Kenneth, N. H. Lindner, and D. Gershoni, "Deterministic generation of a cluster state of entangled photons," Science **354**, 434 (2016).

[87] T. K. Bracht, M. Cosacchi, T. Seidelmann, M. Cygorek, A. Vagov, V. M. Axt, T. Heindel, and D. E. Reiter, "Swing-Up of Quantum Emitter Population Using Detuned Pulses," PRX Quantum **2**, 040354 (2021).

[88] J. Gea-Banacloche, "Some implications of the quantum nature of laser fields for quantum computations," Phys. Rev. A **65**, 022308 (2002).

[89] K. Igeta, N. Imoto, and M. Koashi, "Fundamental limit to qubit control with coherent field," Phys. Rev. A **87**, 022321 (2013).

[90] C. Pellegrini, A. Marinelli, and S. Reiche, "The physics of x-ray free-electron lasers," Rev. Mod. Phys. **88**, 015006 (2016).

[91] J. Klaers, J. Schmitt, F. Vewinger, and M. Weitz, "Bose-Einstein condensation of photons in an optical microcavity," Nature **468**, 545 (2010).

[92] A. Karnieli, N. Rivera, A. Arie, and I. Kaminer, "The coherence of light is fundamentally tied to the quantum coherence of the emitting particle," Sci. Adv. **7**, eabf8096 (2021).

[93] R. Renner, "SECURITY OF QUANTUM KEY DISTRIBUTION," Int. J. Quantum Inform. **06**, 1 (2008).

[94] J. Biamonte, P. Wittek, N. Pancotti, P. Rebentrost, N. Wiebe, and S. Lloyd, "Quantum machine learning," Nature **549**, 195 (2017).

[95] N. Moll, P. Barkoutsos, L. S. Bishop, J. M. Chow, A. Cross, D. J. Egger, S. Filipp, A. Fuhrer, J. M. Gambetta, M. Ganzhorn, A. Kandala, A. Mezzacapo, P. Müller, W. Riess, G. Salis, J. Smolin, I. Tavernelli, and K. Temme, "Quantum optimization using variational algorithms on near-term quantum devices," Quantum Sci. Technol. **3**, 030503 (2018).

[96] M. Ringbauer, M. Meth, L. Postler, R. Stricker, R. Blatt, P. Schindler, and T. Monz, "A universal qudit quantum processor with trapped ions," Nat. Phys. **18**, 1053 (2022).

[97] C. D. Bruzewicz, J. Chiaverini, R. McConnell, and J. M. Sage, "Trapped-ion quantum computing: Progress and challenges," Appl. Phys. Rev. **6**, 021314 (2019).

[98] Y. Nakamura, Y. A. Pashkin, and J. S. Tsai, "Coherent control of macroscopic quantum states in a single-Cooper-pair box," Nature **398**, 786 (1999).

[99] M. Kjaergaard, M. E. Schwartz, J. Braumüller, P. Krantz, J. I.-J. Wang, S. Gustavsson, and W. D. Oliver, "Superconducting Qubits: Current State of Play," Annu. Rev. Condens. Matter Phys., 369 (2020).

[100] E. Knill, R. Laflamme, and G. J. Milburn, "A scheme for efficient quantum computation with linear optics," Nature **409**, 46 (2001).

[101] S. Slussarenko and G. J. Pryde, "Photonic quantum information processing: A concise review," Appl. Phys. Rev. **6**, 041303 (2019).

[102] S. P. Neumann, A. Buchner, L. Bulla, M. Bohmann, and R. Ursin, "Continuous entanglement distribution over a transnational 248 km fiber link," Nat. Commun. **13**, 6134 (2022).

[103] X.-M. Hu, Y. Guo, B.-H. Liu, C.-F. Li, and G.-C. Guo, "Progress in quantum teleportation," Nat. Rev. Phys. **5**, 339 (2023).

[104] Y.-A. Chen, Q. Zhang, T.-Y. Chen, W.-Q. Cai, S.-K. Liao, J. Zhang, K. Chen, J. Yin, J.-G. Ren, Z. Chen, S.-L. Han, Q. Yu, K. Liang, F. Zhou, X. Yuan, M.-S. Zhao, T.-Y. Wang, X. Jiang, L. Zhang, W.-Y. Liu, Y. Li, Q. Shen, Y. Cao, C.-Y. Lu, R. Shu, J.-Y. Wang, L. Li, N.-L. Liu, F. Xu, X.-B. Wang, C.-Z. Peng, and J.-W. Pan, "An integrated space-to-ground quantum communication network over 4,600 kilometres," Nature **589**, 214 (2021).

[105] J. C. López Carreño, E. Zubizarreta Casalengua, B. Silva, E. del Valle, and F. P. Laussy, "Loss of antibunching," Phys. Rev. A **105**, 023724 (2022).

[106] G. Kurizki, P. Bertet, Y. Kubo, K. Mølmer, D. Petrosyan, P. Rabl, and J. Schmiedmayer, "Quantum technologies with hybrid systems," Proc. Natl. Acad. Sci. U.S.A. **112**, 3866 (2015).

[107] F. P. Laussy, G. Malpuech, A. Kavokin, and P. Bigenwald, "Spontaneous Coherence Buildup in a Polariton Laser," Phys. Rev. Lett. **93**, 016402 (2004).

[108] A. Amo, J. Lefrère, S. Pigeon, C. Adrados, C. Ciuti, I. Carusotto, R. Houdré, E. Giacobino, and A. Bramati, "Superfluidity of polaritons in semiconductor microcavities," Nat. Phys. **5**, 805 (2009).

[109] A. Streltsov, G. Adesso, and M. B. Plenio, "Colloquium: Quantum coherence as a resource," Rev. Mod. Phys. **89**, 041003 (2017).

[110] J. M. Matera, D. Egloff, N. Killoran, and M. B. Plenio, "Coherent control of quantum systems as a resource theory," Quantum Sci. Technol. **1**, 01LT01 (2016).

[111] S. Ghosh and T. C. H. Liew, "Quantum computing with exciton-polariton condensates," npj Quantum Inf. **6**, 16 (2020).

[112] D. Ballarini, A. Gianfrate, R. Panico, A. Opala, S. Ghosh, L. Dominici, V. Ardizzone, M. De Giorgi, G. Lerario, G. Gigli, T. C. H. Liew, M. Matuszewski, and D. Sanvitto, "Polaritonic Neuromorphic Computing Outperforms Linear Classifiers," Nano Lett. **20**, 3506 (2020).

[113] T. Boulier, M. J. Jacquet, A. Maître, G. Lerario, F. Claude, S. Pigeon, Q. Glorieux, A. Amo, J. Bloch, A. Bramati, and E. Giacobino, "Microcavity Polaritons for Quantum Simulation," Adv. Quantum Technol. **3**, 2000052 (2020).

[114] A. Kavokin, T. C. H. Liew, C. Schneider, P. G. Lagoudakis, S. Klembt, and S. Höfling, "Polariton condensates for classical and quantum computing," Nat. Rev. Phys. **4**, 435 (2022).

[115] A. Opala and M. Matuszewski, "Harnessing exciton-polaritons for digital computing, neuromorphic computing, and optimization [Invited]," Opt. Mater. Express **13**, 2674 (2023).

[116] B. Nelsen, G. Liu, M. Steger, D. W. Snoke, R. Balili, K. West, and L. Pfeiffer, "Dissipationless Flow and Sharp Threshold of a Polariton Condensate with Long Lifetime," Phys. Rev. X **3**, 041015 (2013).

[117] Y. Sun, Y. Yoon, M. Steger, G. Liu, L. N. Pfeiffer, K. West, D. W. Snoke, and K. A. Nelson, "Direct measurement of polariton-polariton interaction strength," Nat. Phys. **13**, 870 (2017).

[118] H. Alnatah, P. Comaron, S. Mukherjee, J. Beaumariage, L. N. Pfeiffer, K. West, K. Baldwin, M. Szymańska, and D. W. Snoke, "Critical fluctuations in a confined driven-dissipative quantum condensate," Sci. Adv. **10**, eadi6762 (2024).

[119] D. M. Myers, S. Mukherjee, J. Beaumariage, D. W. Snoke, M. Steger, L. N. Pfeiffer, and K. West, "Polariton-enhanced exciton transport," Phys. Rev. B **98**, 235302 (2018).

[120] D. W. Snoke, V. Hartwell, J. Beaumariage, S. Mukherjee, Y. Yoon, D. M. Myers, M. Steger, Z. Sun, K. A. Nelson, and L. N. Pfeiffer, "Reanalysis of experimental determinations of polariton-polariton interactions in microcavities," Phys. Rev. B **107**, 165302 (2023).

[121] D. Schmidt, B. Berger, M. Kahlert, M. Bayer, C. Schneider, S. Höfling, E. S. Sedov, A. V. Kavokin, and M. Aßmann, "Tracking Dark Excitons with Exciton Polaritons in Semiconductor Microcavities," Phys. Rev. Lett. **122**, 047403 (2019).

[122] E. Rozas, E. Sedov, Y. Brune, S. Höfling, A. Kavokin, and M. Aßmann, "Polariton–dark exciton interactions in bistable semiconductor microcavities," Phys. Rev. B **108**, 165411 (2023).

[123] C. Lüders, M. Pukrop, F. Barkhausen, E. Rozas, C. Schneider, S. Höfling, J. Sperling, S. Schumacher, and M. Aßmann, "Tracking Quantum Coherence in Polariton Condensates with Time-Resolved Tomography," Phys. Rev. Lett. **130**, 113601 (2023).

[124] A. F. Adiyatullin, M. D. Anderson, P. V. Busi, H. Abbaspour, R. André, M. T. Portella-Oberli, and B. Deveaud, "Temporally resolved second-order photon correlations of exciton-polariton Bose-Einstein condensate formation," Appl. Phys. Lett. **107**, 221107 (2015).

[125] H. Deng, G. Weihs, C. Santori, J. Bloch, and Y. Yamamoto, "Condensation of Semiconductor Microcavity Exciton Polaritons," Science **298**, 199 (2002).

[126] N. D. Vy, H. T. Cao, D. B. T. Thoai, and H. Haug, "Time dependence of the ground-state population statistics of condensed microcavity polaritons," Phys. Rev. B **80**, 195306 (2009).

[127] L. Ares and A. Luis, "Beam splitter as quantum coherence-maker," Phys. Scr. **98**, 015101 (2023).

[128] G. Díez, L. Ares, and A. Luis, "Coherence via reiterated beam splitting," Phys. Rev. A **109**, 063706 (2024).

[129] J. Thewes, C. Lüders, and M. Aßmann, "Conditional spectroscopy via non-stationary optical homodyne quantum state tomography," Phys. Rev. A **101**, 023824 (2020).

[130] D. F. McAlister and M. G. Raymer, "Ultrafast photon-number correlations from dual-pulse, phase-averaged homodyne detection," Phys. Rev. A **55**, R1609 (1997).

[131] E. Estrecho, T. Gao, N. Bobrovska, M. D. Fraser, M. Steger, L. Pfeiffer, K. West, T. C. H. Liew, M. Matuszewski, D. W. Snoke, A. G. Truscott, and E. A. Ostrovskaya, "Single-shot condensation of exciton polaritons and the hole burning effect," Nat. Commun. **9**, 2944 (2018).

[132] M. Nirmal, B. O. Dabbousi, M. G. Bawendi, J. J. Macklin, J. K. Trautman, T. D. Harris, and L. E. Brus, "Fluorescence intermittency in single cadmium selenide nanocrystals," Nature **383**, 802 (1996).

[133] N. I. Fisher, *Statistical Analysis of Circular Data* (Cambridge University Press, 1993).

[134] A. Amo and J. Bloch, "Exciton-polaritons in lattices: A non-linear photonic simulator," C. R. Phys. **17**, 934 (2016).

[135] A. V. Trifonov, F. Godejohann, O. N. Yakovlev, I. A. Akimov, M. Bayer, and M. Aßmann, "Continuous real-time optical homodyne detection," Opt. Express **33**, 17418 (2025).

List of Publications

[1] E. Rozas, E. Sedov, Y. Brune, S. Höfling, A. Kavokin, and M. Aßmann, "Polariton–dark exciton interactions in bistable semiconductor microcavities," Phys. Rev. B **108**, 165411 (2023).

[2] E. Rozas, Y. Brune, K. West, K. W. Baldwin, L. N. Pfeiffer, J. Beaumariage, H. Alnatah, D. W. Snoke, and M. Aßmann, "Targeted Polariton Flow Through Tailored Photonic Defects," Nanomaterials **14**, 1691 (2024).

[3] Y. Brune, E. Rozas, K. West, K. Baldwin, L. N. Pfeiffer, J. Beaumariage, H. Alnatah, D. W. Snoke, and M. Aßmann, "Quantum coherence of a long-lifetime exciton-polariton condensate," Commun. Mater. **6**, 123 (2025).

[4] Y. Brune, M. Cizauskas, and M. Aßmann, "Quantum resource theory of lasers," Phys. Rev. Res. **8**, 013170 (2026).

[5] E. Rozas, W. Bukalski, Y. Brune, A. Gupta, K. Baldwin, L. N. Pfeiffer, H. Alnatah, J. Beaumariage, D. W. Snoke, P. Comaron, M. H. Szymańska, and M. Aßmann, "Temporal hopping dynamics in exciton-polariton condensation," Optica **13**, 1658 (2026).

Use of Artificial Intelligence

During the preparation of this thesis, artificial intelligence tools were used exclusively to improve sentence syntax and to correct grammar, spelling, and orthography. Specifically, ChatGPT v.5.2-5.3, Grammarly, and DeepL Write were employed for these purposes. At no stage of the writing process was artificial intelligence used to generate original content or to restructure or optimize the logical organization of the text.

Acknowledgments

Now, where everything is done, and everything is said, I want to thank all the people without whose assistance over the last few years I would not be here, and this thesis would not have been written. First of all, I want to thank Prof. Dr. Marc Aßmann, for giving me the opportunity to do my PhD in his group and for introducing me to the interesting and diverse fields of polaritonics and optical homodyne tomography. I also preciously thank my long-standing colleague Dr. Elena Rozas for the countless hours of common and fruitful work in the lab, the uncountable discussions, and her always positive mindset in times of setbacks. Further, I want to thank my former colleagues Dr. Bernd Berger and Dr. Carolin Lüders, who introduced me in the topics of polaritonics and optical homodyne tomography, as well as my successor Juliane Rütter, with whom I know the setup is in good hands. My thanks also go to Lars Wieschollek and Daniel Tüttmann for their technical expertise and for supplying me with helium, as well as to Michaela Wäscher for her organizational support. Finally, I thank all former and current members of E2 for the warm atmosphere over the last few years. Special thanks go to my office colleagues Simon Siegeroth, Gabriel Brune, Nils Denkmann, Steven Nicolai, Lasse Leukefeld, Hakon Etteldorf, Adrian Wittrock, Lars Olschewski, and Mariam Harati, whose conversations and jokes cheered me up when the lab knocked me down. Last but not least, I want to thank my friends, especially Lukas Rolf and Dr. David Rolf, who had to endure my countless talks about malfunctioning lab equipment, and my Family, my parents Anja and Gerald Brune, and my Sisters Clara and Lina, who always supported me.